

JWST PRIMER: A deep JWST study of all ALMA-detected galaxies in PRIMER COSMOS – dust-obscured star-formation history back to $z \simeq 7$

Feng-Yuan Liu¹*, James S. Dunlop¹, Ross J. McLure¹, Derek J. McLeod¹, Laia Barrufet¹,
 Adam C. Carnall¹, Ryan Begley¹, Pablo G. Pérez-González^{2,3}, Callum T. Donnan¹, Richard S. Ellis³,
 Norman A. Grogin⁴, Dan Magee⁴, Garth D. Illingworth⁵, Fergus Cullen¹, Struan D. Stevenson¹,
 Anton M. Koekemoer⁴, Adriano Fontana⁶, Rebecca A. A. Bowler⁷

¹*Institute for Astronomy, University of Edinburgh, Royal Observatory, Edinburgh, EH9 3HJ, UK*

²*Centro de Astrobiología (CAB), CSIC-INTA, Ctra. de Ajalvir km 4, Torrejón de Ardoz, E-28850, Madrid, Spain*

³*Department of Physics & Astronomy, University College London. Gower St., London WC1E 6BT, UK*

⁴*Space Telescope Science Institute, 3700 San Martin Drive, Baltimore, MD 21218, USA*

⁵*Department of Astronomy and Astrophysics, UCO/Lick Observatory, University of California, Santa Cruz, CA 95064, USA*

⁶*INAF - Osservatorio Astronomico di Roma, via di Frascati 33, 00078 Monte Porzio Catone, Italy*

⁷*Jodrell Bank Centre for Astrophysics, Department of Physics & Astronomy, School of Natural Sciences, The University of Manchester, Manchester, M13 9PL, UK*

Accepted XXX. Received YYY; in original form ZZZ

ABSTRACT

We use the deep NIRCam and MIRI imaging from the *JWST* PRIMER survey to study the properties of (sub)mm sources detected by ALMA in the centre of the COSMOS field, with the ultimate aim of defining the cosmic history of dust-enshrouded star formation. The wealth of ALMA data in this field enabled us to isolate a robust sample of 128 (sub)mm sources within the 175 arcmin² PRIMER COSMOS survey footprint, spanning two decades in (sub)mm flux density. The *JWST* imaging is deep and red enough to reveal secure galaxy counterparts for *all* of these sources. This 100% identification completeness is accompanied by an unusually high level of redshift completeness: 52% of the sources have spectroscopic redshifts, and this has enabled us to refine the photometric redshifts for the remaining galaxies. Armed with robust redshift information, we calculate the star-formation rates (SFR) and stellar masses (M_*) of all 128 ALMA-detected galaxies, and place them in the context of other galaxies in the field. We find that the vast majority of star formation is dust-enshrouded in all of the ALMA-detected galaxies, with SFR ranging from $\simeq 1000 M_\odot \text{ yr}^{-1}$ down to $\simeq 20 M_\odot \text{ yr}^{-1}$. We also find that virtually all (126/128) have high stellar masses, $M_* > 10^{10} M_\odot$, independent of redshift. The unusually high quality of our sample enables us to make a robust estimate of the contribution of the ALMA-detected galaxies to cosmic star-formation rate density, ρ_{SFR} . However, despite delivering 128 sources, the *deep* ALMA imaging is highly incomplete, with the individual pointings covering $< 20\%$ of the PRIMER COSMOS area. We therefore use our knowledge of all other massive galaxies in the field to produce a completeness-corrected estimate of dust-enshrouded ρ_{SFR} from $z \simeq 2$ out to $z \simeq 7$. This confirms that UV-visible star formation dominates ρ_{SFR} at $z > 4$, but also indicates that dust-enshrouded star formation likely still made a significant contribution at higher redshifts; extrapolation of our results suggest a $\simeq 20\%$ contribution at $z \simeq 8$, and potentially still $\simeq 5\%$ at $z \simeq 10$.

Key words: galaxies: star formation – galaxies: evolution – galaxies: high-redshift – infrared radiation – submillimeter

1 INTRODUCTION

A complete understanding of the prevalence, history and physical drivers of dust-obscured star-formation activity is of vital importance for advancing our knowledge of galaxy formation and evolution. It is now well established that the majority of the star formation in galaxies during the era of peak activity (‘cosmic noon’, corresponding to $z \simeq 2$) is enshrouded in dust, with most of the rest-frame ultraviolet

(UV) light emitted by newly born massive stars being absorbed and re-emitted by the warmed dust grains in the rest-frame far-infrared (Madau & Dickinson 2014; Dunlop et al. 2017; Bouwens et al. 2020; Zavala et al. 2021).

However, the picture at earlier times is much less clear, in large part due to the limitations of existing ground-based and space-based observing facilities in the near-mid infrared prior to the advent of the *James Webb Space Telescope* (*JWST*). Specifically, the limited wavelength coverage offered by the (relatively warm) *Hubble Space Telescope* (*HST*) ($\lambda < 1.6 \mu\text{m}$) has hampered its ability to uncover

* E-mail: Fengyuan.Liu@ed.ac.uk

dust-reddened galaxies beyond $z \approx 3$ (Barrufet et al. 2023a; Xiao et al. 2023; Pérez-González et al. 2023; Sun et al. 2025), while the poor angular resolution of the *Spitzer* Space Telescope ultimately limited its ability to deliver near/mid-infrared imaging of sufficient depth and resolution to detect all but the most extreme objects at high redshifts. As a result, previous optical-IR follow-up of sources uncovered in (sub)mm surveys has generally been incomplete (e.g., Michałowski et al. 2017; Dudzevičiūtė et al. 2020), leading to considerable uncertainty over the importance/evolution of dust-enshrouded star-formation activity during the first ≈ 2 Gyr of cosmic history (e.g., Rowan-Robinson et al. 2016; Koprowski et al. 2017; Wang et al. 2019; Williams et al. 2019; Loiacono et al. 2021; Gruppioni et al. 2020; Casey et al. 2021).

At very early cosmic times most/all star-formation activity is of course expected to be visible in the rest-frame UV, due to the delayed production of dust from the first generation of stars. At some point star formation in the Universe must therefore transition from mainly unobscured to primarily dust-obscured, and mapping out this transition is a key challenge. Interestingly, recent studies of very early galaxies with *JWST* indicate that most discovered to date at $z > 10$ are largely dust-free (e.g., Cullen et al. 2024, 2025; Ferrara et al. 2025), in stark contrast to the aforementioned later dominance of dust-enshrouded activity by $z \approx 1 - 3$. However, the comparison is complicated by the fact that the dust-obscured star formation activity at cosmic noon is dominated by the contribution of massive galaxies, with stellar masses $M_* > 10^{10} M_\odot$ (McLure et al. 2018), and none of the extreme-redshift galaxies uncovered so far lie above this threshold (Donnan et al. 2024, 2025). Indeed, the cosmic volume covered by the deepest contiguous ALMA survey completed to date – in the Hubble Ultra-Deep Field (HUDF: Dunlop et al. 2017; Bouwens et al. 2020) – proved too small to contain any such massive galaxies at $z > 3$.

Now, however, the situation is being transformed due to the unique power of *JWST* in the near-mid infrared, and by a gradual growth in the availability of deep ALMA (sub)mm imaging over significant areas of sky. Indeed, the data provided by the major *JWST* Cycle-1 Public Release IMAGING for Extragalactic Research (PRIMER, Dunlop et al. 2021) survey has already proved its worth in this arena, with Gillman et al. (2024) using the PRIMER imaging of the COSMOS and UDS survey fields to successfully identify and study the submm-bright galaxies discovered through ALMA follow-up of the 850- μm sources originally uncovered with SCUBA-2 on the James Clerk Maxwell Telescope (JCMT) (Geach et al. 2017; Simpson et al. 2019, 2020; Dudzevičiūtė et al. 2020). However, such extreme (sub)mm galaxies, forming stars at a rate $\approx 500 M_\odot \text{ yr}^{-1}$ are extremely rare at high redshift, and only scratch the surface of the full dust-enshrouded star-forming galaxy population. What is required to complete our inventory is deep *JWST* imaging of a large and representative sample of (sub)mm galaxies, deep enough to reach down to the luminosities of the faintest sources uncovered by ALMA in the HUDF, and large enough to contain significant numbers of very high-redshift dusty galaxies (should they exist).

In this new investigation we attempt to bridge this gap by using the data from the aforementioned *JWST* PRIMER survey to identify and study the properties of all known ALMA sources in the central region of the COSMOS field (corresponding to the PRIMER COSMOS survey footprint, which in turn is based on the *HST* COSMOS footprint in CANDELS; Grogin et al. 2011; Koekemoer et al. 2011). While the ALMA imaging of this $\approx 175 \text{ arcmin}^2$ field is a long way from complete, it transpires that a sufficiently large number of deep ALMA observing programmes have been conducted in this region for us to construct an archival sample of 128 (sub)mm sources (only 17 of which

are bright enough to feature in the AS2COSMOS survey; Simpson et al. 2020). The outcome of our detailed *JWST*+*HST*+UltraVISTA optical-infrared investigation of this newly assembled ALMA sample is the key focus of the work presented here.

The rest of this paper is structured as follows. In Section 2 we present and summarize the key *JWST*, UltraVISTA and ALMA data (along with the important supporting archival *HST*, *Spitzer*, CFHT, and Subaru imaging) used in this new study of the PRIMER COSMOS field, detailing the reduction of the *JWST* PRIMER data, and how the ALMA catalogue in the PRIMER COSMOS survey footprint was assembled from the A³COSMOS database. In Section 3 we then describe how the multi-frequency catalogue was produced for the ALMA sources, discussing first the accurate positional cross-matching of the (sub)mm and optical-infrared catalogues, and then explaining the process by which complete redshift information was assembled for the 128 ALMA-detected galaxies in our final sample. In Section 4 we use this unusually robust redshift information along with the full multi-frequency photometry to derive the basic physical properties of these galaxies, in particular their star-formation rates (SFR) (as estimated through different techniques) and stellar masses (M_*). We conclude this section by making a new estimate of the contribution of dust-enshrouded star formation to the evolution of total cosmic star-formation density (ρ_{SFR}) out to $z \approx 7$, and comparing our findings to other recent results in the literature. Finally, our main conclusions are summarized in Section 5.

Throughout the paper we assume a flat cold dark matter cosmology with $H_0 = 67.4 \text{ km s}^{-1} \text{ Mpc}^{-1}$, $\Omega_m = 0.315$ and $\Omega_\Lambda = 0.685$ (Planck Collaboration et al. 2020). All quoted magnitudes are in the AB system (Oke 1974; Oke & Gunn 1983) and all derived star-formation rates (SFR) and stellar masses (M_*) assume a Chabrier IMF (Chabrier 2003).

2 DATA

In this study, we use the best available space-based and ground-based optical-infrared data to attempt to gain a complete understanding of the (sub)mm-detected galaxies which have been uncovered by a range of studies with ALMA in the centre of the COSMOS survey field over recent years.

Because the primary aim of this work is to explore what new information about the known sub-mm/mm sources in the COSMOS field can be revealed by the new high-quality *JWST* NIRCам and MIRI imaging, we first describe the *JWST* PRIMER data in the COSMOS field, as this defines the chosen survey area (and hence the cosmological volumes probed). We then stay at near-infrared wavelengths, summarizing the ground-based UltraVISTA data that was (by necessity) used in those areas of the COSMOS PRIMER survey footprint which only received coverage with MIRI. Lastly, we summarize the sample of (sub)mm-selected sources within the PRIMER COSMOS footprint which we assembled from the ALMA A³COSMOS database. This sample of 128 sources, detected via their rest-frame far-infrared/sub-mm dust emission, is the primary focus of this study. However, to attempt to correct for the inevitable incompleteness of the ALMA ‘survey’, we also exploit the highly-complete infrared-selected catalogues of massive galaxies produced from the *JWST* PRIMER and UltraVISTA survey data.

2.1 PRIMER COSMOS

The Public Release IMAGING for Extragalactic Research (PRIMER, Dunlop et al. 2021) survey is the largest public GO ‘Galaxies’ pro-

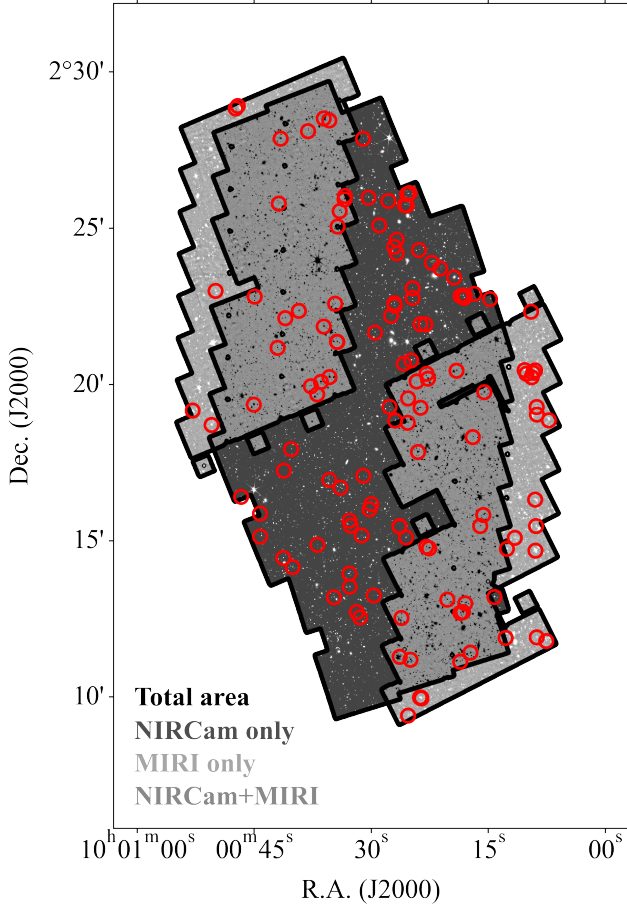


Figure 1. The complete 175.3 arcmin^2 coverage provided by the *JWST* PRIMER imaging within the COSMOS field. The NIRCcam-only coverage (dark grey) is 66.0 arcmin^2 , and the MIRI-only coverage (light grey) is 33.1 arcmin^2 , with 76.2 arcmin^2 of overlapping imaging provided by both instruments (grey). The positions of the 128 ALMA sources in our final sample within this footprint (as specified in Section 3) are indicated by the red circles. The near/mid-infrared counterparts of all of these ALMA sources are securely detected by the NIRCcam and/or MIRI imaging provided by PRIMER, enabling a complete study of their redshift distribution and physical properties.

programme undertaken with *JWST* in Cycle 1. Now complete, PRIMER is a deep extragalactic imaging survey which exploits the broad near-infrared wavelength coverage of NIRCcam and the mid-infrared capabilities of MIRI to provide 10-band imaging across the same central regions of the two equatorial extragalactic survey fields that were previously imaged at UV/optical wavelengths with *HST* as part of the Cosmic Assembly NIR Deep Extragalactic Legacy Survey (CANDELS; Grogin et al. 2011; Koekemoer et al. 2011) Treasury programme. Specifically, the two PRIMER fields each provide $\approx 200 \text{ arcmin}^2$ of high-quality space-based imaging within each of the degree-scale Cosmic Evolution Survey (COSMOS, Scoville et al. 2007) and UKIDSS Ultra-Deep Survey (UDS, Lawrence et al. 2007) imaging programmes.

The PRIMER NIRCcam imaging provides contiguous coverage of the near infrared out to $\lambda \approx 5 \mu\text{m}$ through 8 filters: F090W, F115W, F150W, F200W, F277W, F356W, F410M, and F444W. To the extent allowed by parallel imaging and the layout of the *JWST* focal plane,

Table 1. The median global 5σ limiting magnitudes for each of the photometric filters used in this study. For all *JWST* NIRCcam and *HST* imaging, these are measured in $0.5''$ -diameter apertures and corrected to total assuming a point-source correction. For MIRI F770W, this is measured using $0.7''$ -diameter apertures. For all ground-based imaging, these are measured in $2''$ -diameter apertures and corrected to total assuming a point-source correction. For IRAC imaging, the median global depths are calculated using the uncertainties as output by the deconvolution software TPHOT, including a correction to total.

| Filter | 5σ limit (mag) |
|-------------------------------|-----------------------|
| CFHT u* | 27.2 |
| CFHT g | 27.0 |
| CFHT r | 26.5 |
| CFHT i | 26.2 |
| CFHT z | 25.2 |
| Subaru SSC z' | 26.2 |
| VISTA Y | 25.5 |
| VISTA J | 25.3 |
| VISTA H | 25.1 |
| VISTA K _s | 24.9 |
| Spitzer IRAC $3.6\mu\text{m}$ | 26.0 |
| Spitzer IRAC $4.5\mu\text{m}$ | 26.2 |
| HST ACS F435W | 27.4 |
| HST ACS F606W | 27.5 |
| HST ACS F814W | 27.3 |
| JWST NIRCcam F090W | 27.4 |
| JWST NIRCcam F115W | 27.6 |
| JWST NIRCcam F150W | 27.8 |
| JWST NIRCcam F200W | 27.9 |
| JWST NIRCcam F277W | 28.1 |
| JWST NIRCcam F356W | 28.2 |
| JWST NIRCcam F410M | 27.5 |
| JWST NIRCcam F444W | 27.9 |
| JWST MIRI F770W | 25.8 |

the same field was also imaged in the mid-infrared with MIRI through 2 filters: F770W and F1800W.

As noted above, due to the richness of the ALMA data in the COSMOS field, in this (sub)mm-focused study we confine our attention to the COSMOS component of the (now complete) PRIMER survey, i.e., the PRIMER COSMOS field. Here, PRIMER provides contiguous NIRCcam coverage of 142.2 arcmin^2 and contiguous MIRI coverage of 109.3 arcmin^2 , which overlap by 76.2 arcmin^2 . The combined *JWST* PRIMER imaging of the field provided by NIRCcam and/or MIRI thus provides a total sky coverage of 175.3 arcmin^2 (see Fig. 1), which defines the chosen survey area for this study.

The PRIMER NIRCcam data were reduced using the PRIMER Enhanced NIRCcam Image Processing Library (pencil; Magee et al., in preparation, Dunlop et al. in preparation) software. The astrometry of all the reduced images was aligned to *Gaia* Data Release 3 (Gaia Collaboration et al. 2023) and stacked to the same pixel scale of 0.03 arcsec . The PRIMER MIRI data were reduced with a bespoke version of the official *JWST* pipeline described in Pérez-González et al. (2024) and Östlin et al. (2024) with calibrations based on *JWST* pipeline version 1.13.4, context 1263.pmap. Apart from the regular 3 stages of the pipeline, the calibration of the PRIMER MIRI observations included two additional offline steps. First, a background homogenization step was applied after the flat-fielding, based on the construction of a median super-background frame for each exposure (combining the rest of the data taken in the same filter and after sources are masked). This super-background procedure is able to remove striping (mainly in the vertical direction, but also horizontal) and global gradients which especially affect the lower region of the MIRI detector. For the PRIMER MIRI observations we found the

structure of the background to be time-dependent, and therefore the super-background frame was based only on data taken in the same epoch (i.e., within 2 weeks). The second bespoke procedure was developed because the WCS calibration algorithm, `tweakreg`, in the official pipeline failed to provide a good astrometric calibration for our large $20' \times 12'$ mosaics. Therefore, we used the `tweakreg` package version developed by the CEERS team (Bagley et al. 2023) and switched off the official pipeline version in stage 3, obtaining a significantly better astrometrically calibrated mosaic across the whole area covered by our survey.

The NIRCcam source selection utilised here is based on the F356W imaging. At F356W, the NIRCcam detection has a sensitivity of $\sigma = 0.0039 \mu\text{Jy}$ (point-source total, based on 0.5-arcsec apertures) and an angular resolution of 0.12 arcsec. The MIRI catalogue utilised here is constructed based on the F770W data (Donnan et al., in preparation). This reaches a sensitivity of $\sigma = 0.035 \mu\text{Jy}$ (point-source total, based on 0.7-arcsec apertures) with an angular resolution of 0.27 arcsec.

Crucially, by design, the new *JWST* near/mid-infrared imaging is complemented by pre-existing imaging of comparable angular resolution at shorter (optical) wavelengths, obtained with *HST* through the CANDELS Treasury Program. Specifically, imaging with the Advanced Camera for Surveys/Wide Field Channel (ACS/WFC) is available across the full PRIMER COSMOS survey footprint in the F814W and F606W filters and for most of the area in the F435W filters. The $5\text{-}\sigma$ point-source corrected depths of the *JWST* and *HST* photometry used to create the PRIMER COSMOS source catalogue utilised here are given in Table 1.

The description of the catalogue construction and subsequent photometric redshift determination is described in detail in Begley et al. (2024), to which we refer interested readers. Briefly, following PSF homogenisation to the angular resolution of the F444W imaging, we construct a multi-frequency catalogue by running SOURCE EXTRACTOR in dual-image mode, with F356W as the detection image and aperture photometry measured using 0.5-arcsec diameter apertures.

To account for light outside of the aperture for extended sources, we require a further correction to total beyond point-source corrections. Following McLeod et al. (2024), we therefore scale the fluxes and hence SED-derived properties (e.g., stellar masses, see Section 4.1) to the FLUX_AUTO value (Kron 1980) measured by SOURCE EXTRACTOR, and add a further 10% to account for light outside of the Kron aperture.

The photometry provided by the 8 *JWST* NIRCcam bands and the 3 *HST* ACS bands was then combined to derive photometric redshifts for all of the PRIMER-detected sources. Here, the median redshift of seven different spectral energy distribution (SED) fitting runs was taken as the final photometric redshift for each *JWST* source (although in practice spectroscopic redshifts proved to be available for 52% of the sources - see Section 3.4).

Specifically, we perform two LePHARE (Arnouts & Ilbert 2011) SED-fitting runs, using the BC03 (Bruzual & Charlot 2003) and PEGASE (Fioc & Rocca-Volmerange 1999) template libraries. We also perform five SED-fitting runs using EAZY-PY (Brammer et al. 2008). The first run included the standard template set with additional high equivalent-width emission lines. The second run utilised the PEGASE template library (Fioc & Rocca-Volmerange 1997, 1999, 2019). We also use the *AGN_BLUE_SFHZ_13* template set, and finally, the two SED template sets as described in Larson et al. (2023) and Hainline et al. (2024).

2.2 UltraVISTA

A significant portion (19%) of the PRIMER COSMOS field is only covered by MIRI, which makes it impossible to infer galaxy properties solely on the basis of the new *JWST* data. In order to provide the crucial near-infrared photometry in these regions we used the ground-based imaging data from the UltraVISTA survey (McCracken et al. 2012). This deep, near-infrared survey of the COSMOS field was conducted over the last ~ 14 years using ESO's Visible and Infrared Survey Telescope for Astronomy (VISTA). The survey spans a sky area of 1.9 deg^2 and provides imaging in 4 bands: *Y*, *J*, *H*, and *K_S*.

The ground-based data that we use corresponds to the central ≈ 1 degree overlapping region between UltraVISTA Data Release 4 (DR4) and the optical *u*griz* imaging from the CFHT Legacy Survey D2 T0007 data release (Hudelot et al. 2012). We supplement this optical imaging with deep Subaru Suprime-Cam z'_{new} imaging (Furusawa et al. 2016, see Bowler et al. 2014 for further details).

The UltraVISTA DR4 imaging consists of “deep” and “ultra-deep” stripes, with the area of each depth tier of the survey being about $\sim 50\%$ of the total area. However, the PRIMER footprint lies within one of the ultradeep stripes and, hence, our ground-based photometry is confined to regions of uniform depth in a given photometric band.

A detailed description of the UltraVISTA *K_S*-band catalogue construction is provided in McLeod et al. (2021), to which we refer interested readers. Briefly, source detection was performed on the UltraVISTA *K_S*-band imaging, by running SOURCE EXTRACTOR in dual-image mode and aperture photometry measured in 2-arcsec diameter apertures. To maintain consistency across the multi-frequency dataset, all UV, optical, and NIR images in the UltraVISTA field were PSF homogenized to a Moffat profile with a full width at half maximum (FWHM) of 1.0 arcsec. For the lower resolution *Spitzer* IRAC imaging, photometry was extracted using the deconvolution software TPHOT (Merlin et al. 2015). The $5\text{-}\sigma$ point-source corrected depths of all the VISTA, CFHT, Subaru and *Spitzer* IRAC photometry used to create the UltraVISTA source catalogue utilised here are summarized in Table 1.

Photometric redshifts for the UltraVISTA sources were derived from the combined VISTA, CFHT, Subaru, and *Spitzer* IRAC photometry. The methodology is described in detail in McLeod et al. (2021), and is similar to that adopted for the *JWST+HST* photometric redshifts as outlined above.

As well as providing the crucial near-infrared photometry in those regions of PRIMER COSMOS only covered by MIRI, where NIRCcam imaging *does* exist the inferred galaxy properties from UltraVISTA can still often provide a useful independent check on those derived from the NIRCcam+ACS data. However, where available, we decided to always adopt the final galaxy properties based on the latter, because of the improved depth and extended wavelength coverage provided by NIRCcam in particular.

Finally, we note that, in this study, for a few sources with ambiguous photometric redshifts, the optical-infrared photometric redshifts were further refined for the final catalogue by exploiting the (sub)mm data (see Section 3.3).

2.3 ALMA sources in the PRIMER COSMOS field

The COSMOS field is particularly rich in archival ALMA data. It has been targeted in a systematic way, for example through the AS2COSMOS survey (Simpson et al. 2020) which uncovered 260 ALMA sources via band-7 continuum follow-up observations of a highly-complete flux-limited ($S_{850} > 6.2 \text{ mJy}$) sample of the brightest submillimeter sources detected by the JCMT SCUBA-2

S2COSMOS single-dish survey over the full 1.6 deg^2 of the COSMOS field (Simpson et al. 2019). This survey has also stimulated further ALMA follow-up, such as the band-3 ALMA spectroscopic survey, AS2COSPEC (Chen et al. 2022; Liao et al. 2024). However, the COSMOS field, and in particular the central area of most relevance for the present study, has also been the subject of numerous pointed ALMA follow-up observations of objects selected at other wavelengths, as exemplified by the REBELS survey which undertook targeted ALMA follow-up of the brightest rest-frame-UV selected $z \approx 6 - 7$ galaxies in the field (e.g., Bouwens et al. 2022; Inami et al. 2022; Barrufet et al. 2023a; Bowler et al. 2024).

The most comprehensive source of archival ALMA data in the COSMOS field is provided by the latest version of the A³COSMOS survey (version 20220606, Adscheid et al. 2024). The A³COSMOS database currently contains all publicly available ALMA observations taken before 6 June 2022 in the COSMOS field, calibrated, reduced, and analysed in a consistent manner. To search for ALMA-detected sources in the PRIMER COSMOS footprint, we used the ‘blind’ photometric catalogue provided by Adscheid et al. (2024), in which no prior information at other wavelengths was used to aid source extraction. This catalogue contains all ALMA detections (at any frequency) with a peak flux density signal-to-noise ratio (S/N_{peak}) of 5.40 or higher. Across the full COSMOS field, there are 2,204 entries in total in this latest blind catalogue, which is almost double the number of detections (1,134) reported five years earlier in the version 20180102 of A³COSMOS (Liu et al. 2019). Basic source properties, such as positional coordinates and flux densities are based on multiple-component Gaussian fitting performed by PYBDSF (for details see Liu et al. 2019).

Restricting attention to the relatively small PRIMER COSMOS footprint as defined by our JWST observations still leaves a perhaps surprisingly large number of 347 A³COSMOS detections. However, most of these entries in the database represent repeat observations of the same ALMA sources at different frequencies or resolutions (or both). We therefore visually grouped the sources to avoid duplication, and produced a sample of 129 unique ALMA sources in the PRIMER COSMOS footprint which have a signal-to-noise ratio of the total observed flux density (S/N_{total}) higher than 3.1 (at some frequency). To this sample we were also able to add one extra source from the new large-area ALMA blank-field survey Ex-MORA (Extended Mapping Obscuration to Reionization with ALMA) survey (Long et al. 2024). This is a 2-mm imaging survey of a 577 arcmin^2 area of COSMOS which includes the PRIMER COSMOS field at its centre. However, because it is relatively shallow, almost all of the sources uncovered by Ex-MORA are sources which were already known from pre-existing bright (sub)mm surveys, and have been reported by A³COSMOS, utilising either its progenitor MORA (Casey et al. 2021; Zavala et al. 2021) data or other ALMA archival observations. Nonetheless, to ensure our ALMA source sample is as up-to-date as possible, we added this single new Ex-MORA source (eMORA.29), yielding a final ALMA source list of 130 objects within the PRIMER COSMOS field.

One complication of utilising the A3COSMOS database is that different ALMA detections of a given source, even when observed at similar wavelengths, can sometimes report quite different flux densities (either because the observations are made at different angular resolutions or because of variation in the S/Ns achieved). For clarity and convenience we therefore cleaned the sample by only retaining the highest S/N ALMA detections in every $10 \mu\text{m}$ wavelength bin for each ALMA source. This left 302 potentially useful independent ALMA detections for the 130 ALMA sources at different wavelengths. Because most of these detections are at (or close

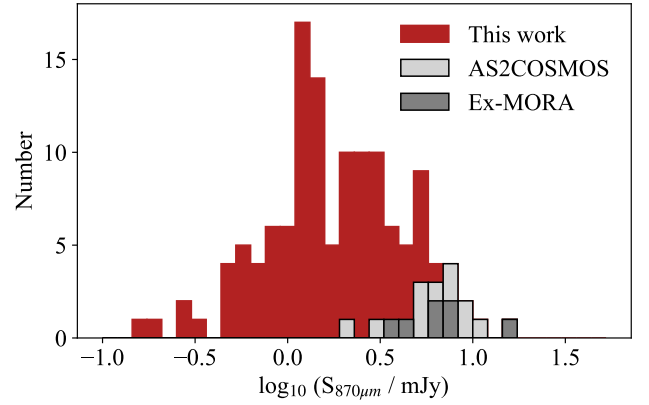


Figure 2. The distribution of $870 \mu\text{m}$ flux density for the 128 ALMA sources in our final sample (red). For sources where the only (or highest S/N) detection in the A³COSMOS catalogue was obtained at a wavelength other than $870 \mu\text{m}$, the flux density was converted to a common observed wavelength of $870 \mu\text{m}$ assuming that the (sub)mm spectral energy distribution has a form $\propto \nu^{-3}$ (see text). The 17 sources detected by AS2COSMOS (light grey) and the 7 sources detected at 2 mm by Ex-MORA (dark grey; 6 in common with AS2COSMOS) included in our sample are over-plotted on the histogram. Not only is our ALMA sample ~ 10 times larger than previous (sub)mm samples studied within the same footprint, but it also bridges the luminosity gap between the brightest sources (e.g., those uncovered with SCUBA-2) and the fainter (sub)mm detections resulting from targeted ALMA follow-up of distant optical/infrared selected galaxies (e.g., as in the REBELS programme; Inami et al. 2022).

to) an observing wavelength of $870 \mu\text{m}$, we decided to construct a pseudo $870 \mu\text{m}$ selected sample, by converting the highest S/N detections of the 130 ALMA sources to $870 \mu\text{m}$ using the relation $f_{870 \mu\text{m}}/f_{\text{obs}} = (\nu_{870 \mu\text{m}}/\nu_{\text{obs}})^3$.

Two sources in this list were later excluded from the final catalogue used in the present study (for reasons explained below in Section 3). Our final sample for the full multi-frequency analysis undertaken here thus consists of 128 unique ALMA sources. The $870 \mu\text{m}$ flux-density distribution of this sample of 128 ALMA sources in the PRIMER COSMOS footprint is shown in Fig. 2. It can be seen that our sample spans two orders-of-magnitude in flux density, extending from the brightest (sub)mm sources uncovered by the wide-area blank-field surveys (our sample contains 17 sources from AS2COSMOS and 7 from Ex-MORA, albeit 6 of the Ex-MORA sources are already included in the 17-source AS2COSMOS list) down to the lowest luminosity sources typically uncovered by deep ALMA pointed follow-up observations (approaching flux densities of $S_{870} \approx 0.1 \text{ mJy}$). We note here that Gillman et al. (2024) used JWST data to study 17 AS2COSMOS sources in COSMOS. Our sample only contains 13 of these because the other 4 lie outside the high-quality PRIMER COSMOS footprint defined here (i.e., they lie in a region only covered by JWST imaging from the COSMOS-Web survey; Casey et al. 2023). However, we recovered another 3 sources (namely AS2COS0017.1, AS2COS0032.1, and AS2COS0035.1) within the MIRI-only footprint that were reported in the original AS2COSMOS catalogue (Simpson et al. 2020). We also include the lensed source (AS2COS0005.1), as its properties have been obtained by detailed modeling (Jin et al. 2024). Therefore, the total number of AS2COSMOS sources in our catalogue is still 17.

3 CONSTRUCTION OF THE FULL MULTI-FREQUENCY ALMA SOURCE CATALOGUE

In this section we describe how we established the full multi-frequency SEDs, and hence ultimately the redshifts and other physical properties of the 128 ALMA-detected galaxies in the PRIMER COSMOS field.

First, we cross-matched the ALMA positions with the positions of the galaxies in the *JWST* and UltraVISTA imaging. As demonstrated and discussed below in Section 3.1, as a result of the high positional accuracy of the ALMA detections and the infrared imaging, this proved to be a relatively straightforward task, with only a few objects requiring additional in-depth analysis to reveal the true infrared-detected galaxy counterpart. Crucially, as a result of the depth of the *JWST* imaging, we have been able to detect the infrared galaxy counterpart of *every* ALMA source in the sample, something rarely before achieved in the optical/infrared follow-up of large (sub)mm-selected samples. This 100% identification completeness, not possible before *JWST*, is obviously of enormous value in subsequent analysis.

With successful and unambiguous identification of the optical/infrared galaxy counterpart comes photometric redshift information from the *JWST* and UltraVISTA photometric catalogues (as described in Sections 2.1 and 2.2). However, for a few objects, especially those where the photometry in the infrared catalogues may have been contaminated by flux from nearby sources, careful manual photometry was required to yield reliable flux densities for the determination of robust photometric redshifts. This process is described in Section 3.2.

Even after assembling the best available optical-infrared photometry, there remain some objects for which the photometric redshift remains unclear or ambiguous, often in the sense that there are two possible alternative solutions at very different redshifts. To improve this situation, we used the multi-frequency ALMA data for each source (where available) to check the plausibility of a given photometric redshift given the expected form of a modified black body for a reasonable assumed dust temperature. This process, which generally helped to exclude some highly uncertain extreme redshift solutions, is summarised in Section 3.3.

Finally, notwithstanding all the above efforts to produce reliable photometric redshifts, we undertook a comprehensive search of the literature and all available spectroscopic databases at optical, infrared and (sub)mm wavelengths to check for the existence of a reliable spectroscopic redshift for each source in our catalogue. Pleasingly, the result of this extensive search is that 66 sources (i.e., 52% of our sample) have reliable spectroscopic redshifts. As described in Section 3.4, this relatively high spectroscopic completeness has enabled us to validate the accuracy of our photometric redshifts, and hence to deliver a robust redshift distribution for our full sample.

3.1 Infrared source identification/cross-matching

To determine the counterparts of the ALMA sources at near-infrared wavelengths, we first cross-matched the ALMA detection coordinates to the coordinates of the sources in the PRIMER COSMOS and UltraVISTA catalogues discussed in Section 2. Fig. 3 shows the distribution of the angular separation between each ALMA detection and the nearest *JWST* or UltraVISTA source. Both distributions peak at very small angles (< 0.15 arcsec), as expected for secure identifications given the high-positional accuracy delivered by ALMA, *JWST* and UltraVISTA (albeit the distribution for UltraVISTA peaks at a slightly larger angle due to the limitations of ground-based seeing). This implies that a relatively small search radius can be used to se-

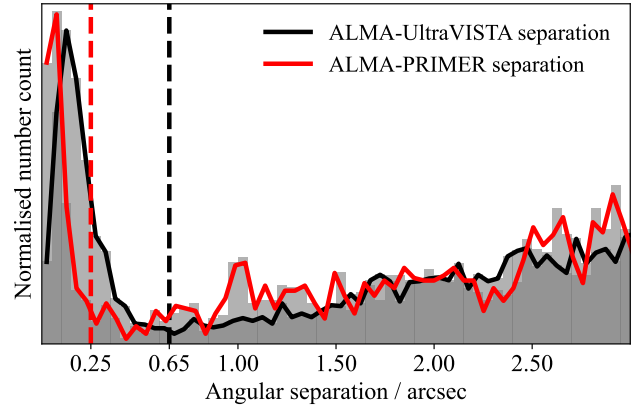


Figure 3. The distribution of the angular separation between the position of each ALMA source in the PRIMER COSMOS footprint and its nearest near-infrared neighbour in the *JWST* (red) or UltraVISTA (black) imaging. Both distributions peak at an angular separation < 0.2 arcsec, reflecting the high positional accuracy of all catalogues. The first local minimum of the ALMA-NIRCam cross-matching distribution occurs at 0.25 arcsec (red vertical dashed line) while that for the ALMA-UltraVISTA cross-matching distribution appears at a somewhat larger radius of 0.65 arcsec (black vertical dashed line), as expected due to the limitations of ground-based seeing. These minima were used to define the search radius for near-infrared counterparts to the ALMA sources in the *JWST* and UltraVISTA catalogues respectively.

cure the near-infrared galaxy counterparts of all ALMA sources, and indeed the distributions both show a clear minimum at reassuringly small angular separation beyond which the number of counterparts starts to rise systematically with increasing angular separation as expected for spurious identifications with galaxies in the field.

We found that an unambiguous NIRCam counterpart for each ALMA source within the NIRCam footprint could be secured using a search radius of only 0.25 arcsec. As can be seen from the vertical red dashed line in Fig. 3 this corresponds to a first minimum in the ALMA-PRIMER source separation distribution, with the use of a larger search radius delivering no additional identifications, but rather just adding a few spurious companion objects. For sources not covered by NIRCam, we searched for UltraVISTA-detected counterparts within a radius of 0.65 arcsec, as indicated by the vertical black dashed line in Fig. 3. This was necessitated by the poorer angular resolution of the data, and resulted in a few multiple possible identifications, but these were able to be refined (and the true galaxy counterpart unambiguously identified) with the use of the MIRI imaging.

The adoption of these relatively small search radii reduces the probability of a spurious identification for each source to $< 1\%$. We note that this situation is very different to the statistically more complex problem of identifying the true galaxy counterparts of (sub)mm sources detected in single dish surveys, where the large (sub)mm beam size (typically FWHM > 10 arcsec) necessitates the use of much larger search radii, vastly increasing the probability of random associations in deep optical/infrared imaging (see, for example, Ivison et al. 2007).

The search of the *JWST* and UltraVISTA catalogues within these adopted search radii yielded a near-infrared counterpart for all but one ALMA source (ALMA R.A. = 150.07486 deg, Dec. = 2.3806 deg). However, this ALMA source is based purely on a highly marginal 3-mm ‘detection’ with $S/N_{\text{total}} = 3.26$ in the A^3 COSMOS catalogue, and is not reported elsewhere in the literature. Increasing the search radius for this object (even by a factor of several) does not reveal

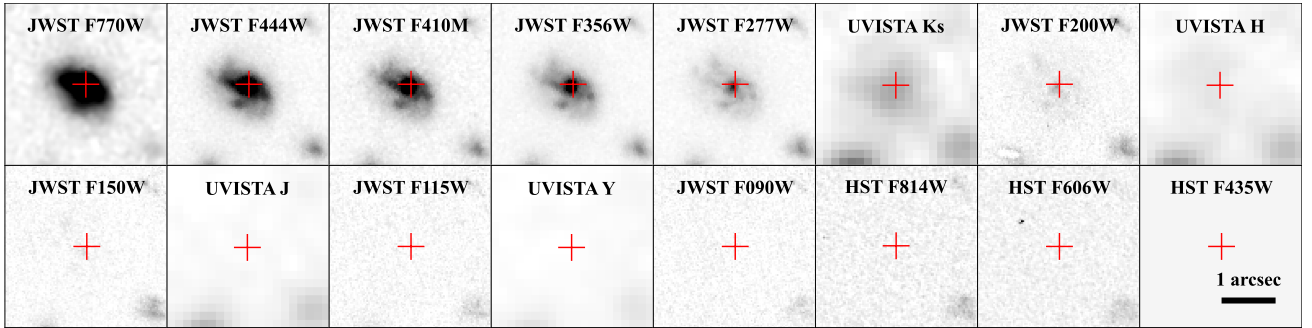
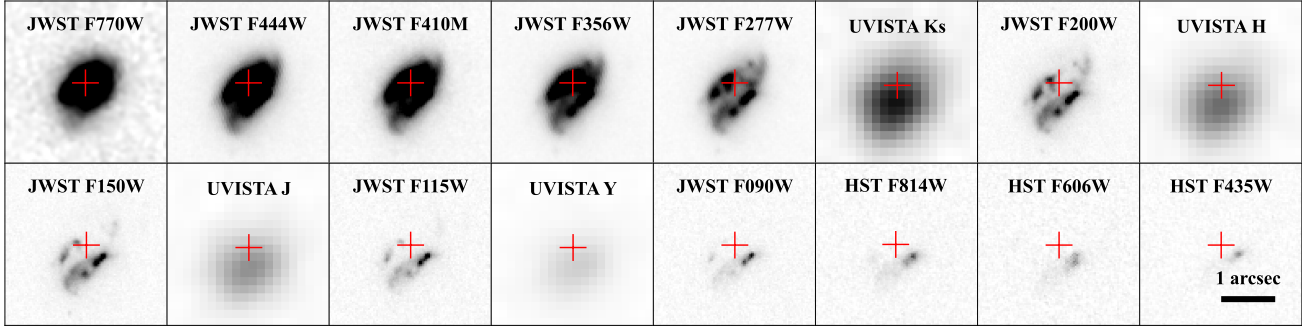
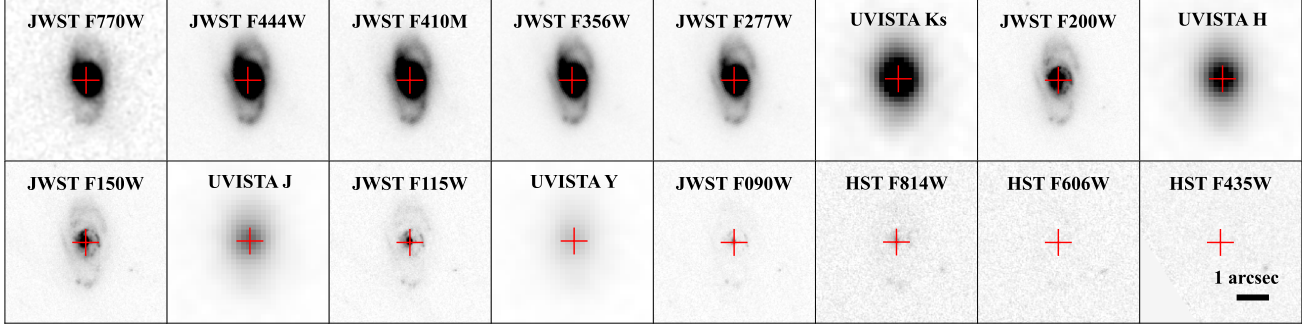
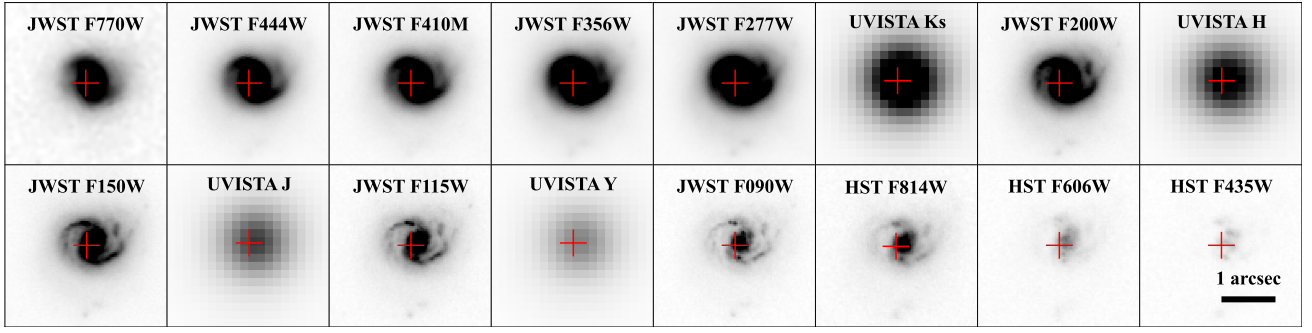


Figure 4. Image stamps in all the available *JWST*, UltraVISTA and *HST* bands for 4 of the sources in our sample (ID 095, ID 053, ID 007, and ID 034). For each of the 4 sources, 16 stamps are shown, ranked in order of decreasing wavelength with filter names marked at the top of each panel, and with the position of the highest-S/N ALMA detection marked by the red cross. These illustrate different but also common features of the typical galaxies in the sample. ID 095, which lies at a redshift of only $z = 0.726$ is detected with *HST* at optical wavelengths (albeit only just at F435W). It is also securely detected in all UltraVISTA near-infrared bands, but the vastly improved angular resolution provided by NIRCcam is key to revealing its spiral disk morphology. ID 053, with $z = 1.552$ is dark on HST F435W to HST 814W images, but has a consistent disk-like morphology across all infrared bands. ID 007, at $z = 2.086$ appears to have an *HST* detection but the longer-wavelength imaging reveals that this does not correspond to the centre of the galaxy; it is either a blue clump or a separate object, and the true mass-dominant galaxy is not revealed until wavelengths longward of $2\ \mu\text{m}$. Finally, ID 034 is a higher-redshift ‘*HST*-dark’ galaxy, with $z_{\text{phot}} \approx 3.55$, and is basically not detected at all until $2\ \mu\text{m}$. Despite these differences caused by a mix of redshift and the degree of dust attenuation, all 4 of the example objects shown here, and in fact all of the galaxies in our sample are detected (and resolved) with relative ease in the longest wavelength NIRCcam and/or MIRI $7.7\ \mu\text{m}$ imaging.

a counterpart in either the *JWST* or UltraVISTA imaging and so we decided to exclude this source as most likely a spurious ALMA detection.

This leaves a sample of 129 ALMA sources with a 100% near/mid-infrared identification rate. All are detected with *JWST*, with the coverage of the PRIMER COSMOS field resulting in 104 being detected with NIRCcam, 112 being detected by MIRI/UltraVISTA, and 87 being detected by both. The reliability of this cross-matching was carefully checked by visually inspecting the near/mid-infrared images at the positions of every ALMA source. Image stamps in all the available *JWST*, UltraVISTA and *HST* bands are shown for four example sources in Fig. 4. These stamps illustrate different aspects of the power of the multi-frequency imaging, including the vastly improved angular resolution provided by NIRCcam over VISTA, and the relative ease with which all of these massive dust-attenuated galaxies are detected at the longest near-mid infrared wavelengths now made possible by *JWST* NIRCcam and MIRI imaging.

It is clear that the depth and extended wavelength coverage provided by the *JWST* PRIMER imaging is vital for uncovering the secure near-infrared counterpart of *every* ALMA source in our sample. While the depth of the K_S imaging provided by UltraVISTA is impressive, without the addition of the *JWST* imaging, 11 of the sources would have remained unidentified given only the previously available ground-based and *HST* imaging. Secondly, in a very small number of cases, the high astrometric accuracy delivered by *JWST* has allowed us to distinguish the true identification from a nearby companion galaxy that lies within the (by necessity) larger UltraVISTA counterpart search radius, as exemplified by our successful identification of the true massive dusty ALMA-detected galaxy Hyde (Schreiber et al. 2018a, ID 064 in our final sample, see Table A1), which lies only 0.43 arcsec away from a brighter quiescent galaxy, ZF-COSMOS-20115.

3.2 Bespoke photometry and the final 128-source catalogue

We produced three-colour (RGB) infrared images of the NIRCcam-detected galaxy counterparts of the ALMA sources using the NIRCcam F444W (red), F277W (green), and F115W (blue) imaging (where available) after convolving the imaging through the latter two filters to the same resolution as the F444W imaging. Where NIRCcam imaging was not available we used the UltraVISTA J -band, the UltraVISTA K_S -band, and MIRI $7.7\ \mu\text{m}$ imaging to produce the RGB images (albeit these inevitably have poorer resolution than the NIRCcam examples). An example (NIRCcam) RGB image is shown in Fig. 5, with the three-colour images for all of the ALMA sources presented in Appendix B.

Fig. 5 illustrates an important point, in particular the dangers of simply assuming that the automated catalogue photometry is correct. In this case, while there is no issue over the correct (red) near-infrared counterpart to the ALMA source, it can be seen that a blue companion object is present (likely in projection) which, while lying well outside the search radius for even an UltraVISTA counterpart, could well contaminate the photometry of this source in ground-based imaging, especially at optical (rest-frame UV) wavelengths. While potential contamination of the NIRCcam photometry due to nearby sources is obviously less likely (due to higher resolution and hence the use of smaller apertures) we nonetheless carefully inspected all of the images of the near-infrared counterparts to search for potential complications due to merging, lensing, or image contamination issues such as diffraction spikes from nearby stars.

Through this process we identified 26 sources for which we judged that the automated catalogue photometry was potentially not to be

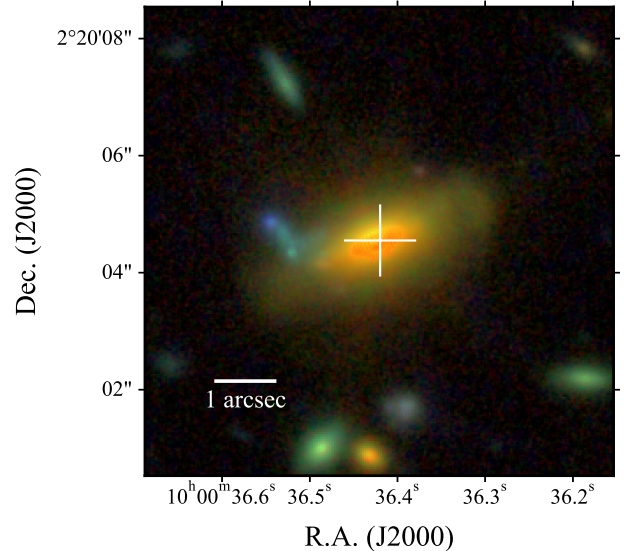


Figure 5. An example RGB image of one of the ALMA-detected galaxies in our sample (ID 100), created from the *JWST* PSF-homogenised NIRCcam imaging: F444W (red), F277W (green), and F115W (blue). The position of the ALMA detection is marked by the white cross. While there is no ambiguity over the correct near-infrared counterpart, a nearby very blue object/component can be seen ≈ 1 arcsec to the east. Such a source is too distant to contaminate the NIRCcam photometry, but could potentially contaminate ground-based photometry, especially at optical (i.e., rest-frame UV) wavelengths. A total of 26 sources were revisited and subjected to manual (rather than automated) photometry to ensure reliable colours and total flux densities. RGB images of all sources in the sample are presented in Appendix B1.

trusted. To be safe, for these objects we manually re-measured the photometry at all bands. This involved careful masking of companions where necessary, but in the main enabled a better representation of the SExtractor isophotal footprint of each object, and hence a better sense of what SExtractor deemed to be the appropriate Kron aperture. This analysis improved the overall centroiding and deblending and delivered a more robust measurement of total flux density which, as well as potentially leading to improved photometric redshifts, ultimately yields more robust physical properties such as stellar mass. This is a painstaking process but one which nonetheless proved invaluable. For example, with the re-measured photometry, the photometric redshift of the (possibly merging) galaxy (ID 075 in the final sample, see Table A2) changes from $z_{\text{photo}} = 1.65$ to $z_{\text{photo}} = 2.82$, which is reassuringly much closer to its spectroscopic redshift $z_{\text{spec}} = 2.989$ (Coulter et al. 2024, from the DAWN *JWST* Archive, see Section 3.4).

The near-infrared counterpart of one source (ALMA RA = 150.10968 deg, Dec = 2.18797 deg) lies on top of a strong diffraction spike from a nearby bright source in the NIRCcam and MIRI images and is blended into that same nearby bright source in the UltraVISTA imaging. Since it is impossible to derive reliable information from the contaminated photometry of this source, we decided to exclude it from the final catalogue. We note that since it is clearly detected in the PRIMER imaging, the removal of this source is unrelated to its actual observed or physical properties, so its rejection on the basis of quality control should not bias our sample.

The final catalogue used for subsequent analysis thus contains a total of 128 ALMA sources, all with robust near-infrared identifications. The coordinates and flux densities of these sources are

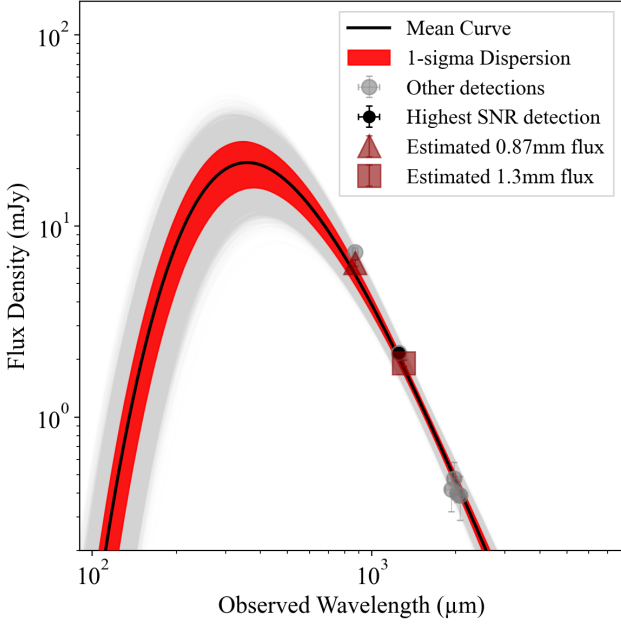


Figure 6. An example of fitting an isothermal modified blackbody to the ALMA photometry for one of our sources, which in this case has a spectroscopic redshift (ID 010, $z_{\text{spec}} = 2.510$). The mean curve is plotted in black with the 1σ dispersion shown in red. The 10,000 MC runs (light grey curves) are plotted in the background. The highest-S/N ALMA detection is marked in black and the rest are shown in grey, with error bars indicating both the flux-density and frequency (i.e., bandwidth) errors. The ALMA detections are consistent with the fitted curve at the adopted redshift of $z = 2.51$.

presented in Table A1, ranked (and labelled) by descending ALMA flux density (converted to $\lambda_{\text{obs}} = 870\ \mu\text{m}$, as discussed in Section 2.3).

3.3 Redshift constraints from ALMA photometry

As mentioned in Section 2.3, 46 (36%) of the ALMA sources in our catalogue have detections in the A³COSMOS database at more than one (sub)mm wavelength. This means that, at least for this subset of sources, it makes sense to perform a sanity check on the optical-infrared photometric redshifts by exploring whether the ALMA photometry (essentially the (sub)mm colour) is consistent with that expected from thermal dust emission of reasonable temperature at the adopted redshift. To do this we fitted a simple isothermal modified blackbody to the available ALMA photometry, as given by the expression:

$$S_\nu = \Omega \frac{2h\nu^3}{c^2} \frac{1}{\exp(h\nu/kT) - 1} \left\{ 1 - \exp\left[-(\nu/\nu_0)^\beta\right] \right\} \quad (1)$$

where ν is the rest frequency (given the adopted redshift z), F_ν is the flux density observed at a frequency equal to $\nu/(1+z)$, Ω is the solid angle subtended by the source, β is the emissivity index of the dust, $\nu_0 = 3.0\ \text{THz}$ is the rest-frame frequency at which the dust emission is assumed to become optically thick (and at all higher frequencies, because the optical depth, τ , at frequency ν is $(\nu/\nu_0)^\beta$), and T is the intrinsic temperature of the dominant dust mass.

During fitting, as well as testing alternative photometric redshifts where appropriate, we allowed the dust emissivity index β to vary in the range $1.5 \leq \beta \leq 2.0$, and adopted a redshift-dependent dust

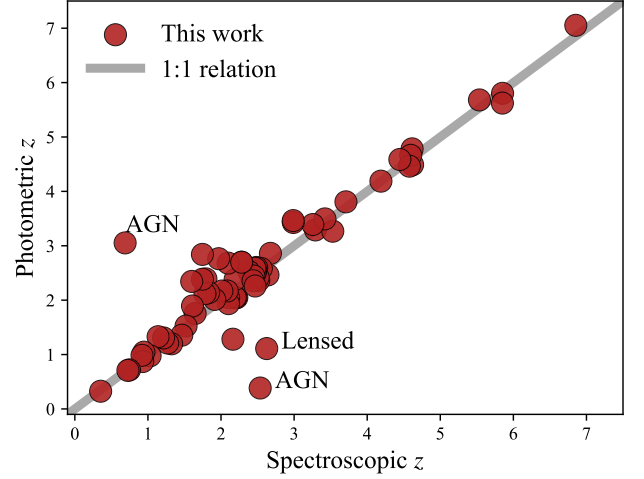


Figure 7. A comparison between the spectroscopic redshifts, z_{spec} , and our final improved photometric redshifts, z_{photo} , for the 66 sources with known z_{spec} in our sample. Apart from the one known lensed galaxy, two bright AGN, and some modest focusing at $2 < z < 3$, z_{photo} and z_{spec} are in excellent agreement, following the 1:1 relation (indicated by the grey line) right out to the highest redshifts.

temperature $T = 32.9 + 4.60 \times (z_{\text{photo}} - 2.0)\ \text{K}$ (Schreiber et al. 2018a) consistent with $T = 35\ \text{K}$ at the median redshift of the final ALMA sample ($z_{\text{med}} \approx 2.5$; see Sec. 3.4). The ALMA fluxes have Gaussian errors and we assumed that the frequency follows a uniform distribution within an ALMA bandwidth of 8 GHz (equivalent to an uncertainty of 4 GHz). We then ran a Monte Carlo (MC) simulation with 10,000 runs for each source to derive means and standard deviations, with each run weighted by the S/N_{total} of the detections. An example of one of the resulting fits, in this case for a source with a robust spectroscopic redshift, is presented in Fig. 6.

For the vast majority of sources, the modified blackbody fits proved to be consistent with the ALMA detections at different frequencies. However, in 5 cases, the fitted curves deviated by more than 5σ from at least one of the ALMA detections (given the assumed optical-infrared photometric redshift). These sources transpired to all have rather high photometric redshifts ($z_{\text{photo}} > 5$) but in fact the optical-infrared photometric redshifts also proved to be highly uncertain, with different code/template combinations delivering very different results and at least some code/template combinations favouring more modest redshifts. In these cases we therefore decided to also allow the redshift to vary while re-performing the modified blackbody fitting, and adopted the optical-infrared photometric solution which lay closest to that implied by the best-fitting (sub)mm photometric redshift. For these 5 sources, this changed the final adopted photometric redshift by $\Delta z \approx 2 - 4$.

3.4 Spectroscopic redshifts

Finally, having established the most probable photometric redshifts for all 128 sources in the sample, we undertook an extensive search of the literature to establish which sources already possessed robust optical/infrared or (sub)mm spectroscopic redshifts.

We found that 53 sources (41% of the entire sample) already have secure optical-infrared spectroscopic redshifts. Unsurprisingly, the vast majority of these come from major spectroscopic survey programmes (with overlaps), such as 3D HST (23 sources, Brammer

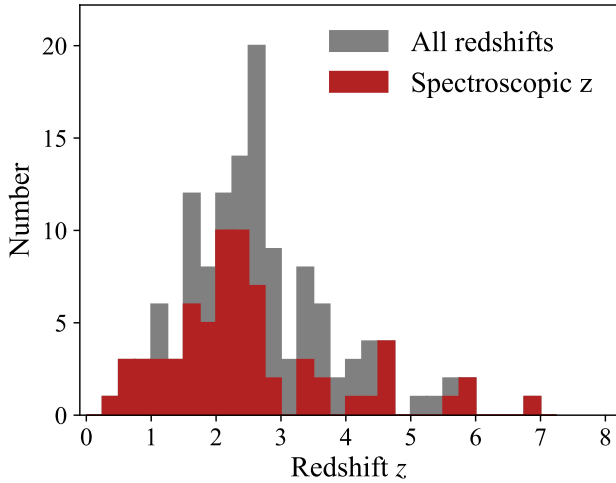


Figure 8. The final redshift distribution of our 128-source sample. The 66 sources for which a spectroscopic redshift has been secured are indicated by the red histogram. It can be seen that the spectroscopic redshift distribution is highly comparable to the overall distribution of the entire sample (grey histogram), with extra coverage in the high-redshift tail.

et al. 2012; Momcheva et al. 2015), DEIMOS (6 sources, Hasinger et al. 2018), zCOSMOS (13 sources, Lilly et al. 2007, 2009), MOSDEF (7 sources, Kriek et al. 2015), LEGA-C (3 sources, van der Wel et al. 2021), and those in the DAWN JWST Archive (DJA, 6 sources, Brammer 2023; Heintz et al. 2024; de Graaff et al. 2024).

To search for reliable (sub)mm spectroscopic redshifts, we matched the ALMA coordinates with ALMA archival targets using ALMiner (Cataldi et al. 2023), an automated ALMA archive mining tool, which enabled us to find published spectroscopic redshifts based on (sub)mm line observations taken up to 2023. We found that 17 sources (13% of the whole sample) had reliable (sub)mm spectroscopic redshifts based on archival ALMA observations. Of these, 11 are new in the sense that these sources do not have secure published optical-infrared spectroscopic redshifts. Among the 6 sources with both optical-infrared and (sub)mm z_{spec} , the results for 4 sources are highly consistent within the (small) measurement uncertainties. However, for the remaining 2 sources, the optical-infrared z_{spec} from 3D HST is somewhat uncertain, and so for these we adopted the more precise (sub)mm z_{spec} resulting from the ALMA line detections. As a final check, we matched our sample with the COSMOS Spectroscopic Redshift Compilation (Khostovan et al. 2025) to verify the quality of the known redshifts and find possible missed spectroscopic information. Three new spectroscopic redshifts with quality flags 4 (‘very reliable redshift’) and 3 (‘reliable redshift’) were obtained, which are originally from surveys C3R2 (Masters et al. 2017, 2019), VUDS (Le Fèvre et al. 2015; Tasca et al. 2017), and zFIRE (Nanayakkara et al. 2016).

In total, therefore, we have established secure spectroscopic redshifts for 66/128 sources, equivalent to 52% of the sample (see Table A2). This is a pleasingly high fraction, especially for a (sub)mm selected sample in which the rest-frame optical-UV is often highly obscured. This, plus the fact that the spectroscopic redshifts span the wide redshift range $0 < z < 7$ allows us to test the validity of our photometric redshifts. The photometric and spectroscopic redshifts for these 66 sources are compared in Fig. 7. It can be seen that, apart from 3 obvious outliers, the photometric and spectroscopic redshifts are in excellent agreement. The only serious outliers are

Table 2. Parameter values adopted as input for BAGPIPES SED fitting. Any parameters not explicitly listed here were set to their default values (Carnall et al. 2018).

| Component | Model parameter | Initial values | |
|-------------------|-------------------|------------------------------|-------------|
| Dust | type | Salim | |
| | eta | 2.0 | |
| | Av | (0.0, 8.0) | |
| | delta | (-0.3, 0.3) | |
| | delta_prior | Gaussian | |
| | delta_prior_mu | 0.0 | |
| | delta_prior_sigma | 0.1 | |
| | B | (0.0, 5.0) | |
| | Nebular | log_U | -3.0 |
| | Stellar (dblplaw) | massformed | (0.0, 13.0) |
| metallicity | | (0.2/z_factor, 3.5/z_factor) | |
| | | z_factor = (0.02/0.014) | |
| metallicity_prior | | "log_10" | |
| alpha | | (0.1, 1000.0) | |
| alpha_prior | | "log_10" | |
| beta | | (0.1, 1000.0) | |
| beta_prior | | "log_10" | |
| tau | | (0.01, 15.0) | |
| tau_prior | | "log_10" | |

two AGN and one lensed galaxy (ID 002, Jin et al. 2024). One of the two outlying AGN, ID 092, exhibits spiral galaxy morphology at shorter wavelengths, but then becomes a saturated point source at wavelengths longer than F200W, resulting in a substantially over-estimated photometric redshift. The other AGN, ID 039, is a saturated point source in all available images and thus unsurprisingly does not have a meaningful constraint on its photometric redshift. Fortunately, these two AGN obviously have secure spectroscopic redshifts, and so their poor photometric redshift estimates are not of importance in this study. No other lensed galaxies are evident in the rest of the sample, and the (very few) AGN are not of serious concern because optical-infrared spectroscopic redshifts are usually readily available for these sources (as in the 2 unusual cases discussed above). In summary, Fig. 7 confirms that the processes we have used to estimate and refine the photometric redshifts of the sources in our ALMA-selected sample have delivered reliable results.

The resulting final, complete redshift distribution of our sample is shown in Fig. 8, with the spectroscopic measurements indicated in red. Here, it can again be seen that the spectroscopic redshifts are representative of the overall redshift distribution, and in particular provide excellent coverage of the key high-redshift tail. The majority (59%) of the final sample lies at so-called cosmic noon, in the redshift range $1.5 < z < 3$. The mean redshift of the sample is $\langle z \rangle = 2.68$ and the median is $z_{\text{med}} = 2.52$.

Compared to previous blind ALMA surveys in the same field, our sample has more sources, both in number and fraction, at higher redshifts. Specifically, almost 30% (37/128) of the ALMA sources in our sample lie at $z > 3$. However, none lie beyond $z = 7$, with the redshift of the most distant source in our sample being spectroscopically confirmed at $z = 6.854$ (Smit et al. 2018). It is worth noting that the spectroscopic redshift coverage at $z > 4$ (10/18, 56%) is even higher than that at lower redshifts (54/110, 49%). This provides additional confidence that our multi-frequency sample can be used to undertake a robust estimate of dust-enshrouded cosmic star-formation activity in the young Universe.

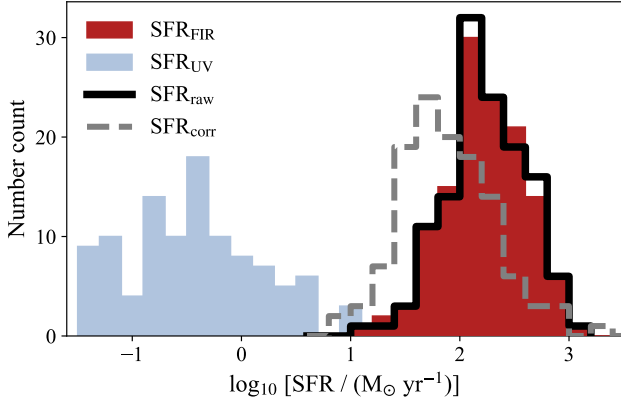


Figure 9. The distribution of different measures of star-formation rate (SFR) for the 128 ALMA-detected galaxies in the PRIMER COSMOS sample. Total ‘raw’ SFR (SFR_{raw} , black solid profile) is the sum of the dust-enshrouded SFR (SFR_{FIR} , red; derived directly from the (sub)mm photometry) and the UV-visible SFR (SFR_{UV} , blue; derived from directly from the optical-infrared photometry *without* correction for dust attenuation). Unsurprisingly, the vast majority of the star-formation activity for all of these ALMA-detected sources is reflected in the (sub)mm emission. The SFR derived from fitting to the optical-infrared SEDs allowing for dust attenuation typically gives a somewhat lower estimate of star-formation rate (SFR_{corr} , dashed grey profile) than the total ‘raw’ SFR, likely due to the failure of this method to account for star formation in the most highly-obscured regions of the galaxies.

4 ANALYSIS & DISCUSSION

Armed with the redshifts and full multi-frequency photometry for all 128 ALMA-detected sources in the PRIMER COSMOS field, we next proceeded to derive best estimates of the basic physical properties of these dusty galaxies. As discussed further in the following subsections, we used the SED-fitting code *BAGPIPES* (Carnall et al. 2018) to determine stellar masses and to provide one estimate of star-formation rate (SFR). We also derived an alternative measure of SFR for each galaxy directly from the raw rest-frame UV and (sub)mm photometry. Below, we present and discuss the resulting derived properties of the galaxies before going on to explore the implications of our results for cosmic star-formation history.

4.1 Star-formation rates

We derived estimates of the SFR for each ALMA-detected galaxy using two different approaches, with the results of both calculations presented in Table A2.

The first calculation of SFR is based on fitting to the observed optical-infrared SEDs of the galaxies (as derived from the *JWST* or *UltraVISTA* photometry, with aperture size effect corrected) using the *BAGPIPES* code. In effect this assumes that the true SFR can be recovered by allowing the attenuation, A_V , to float while seeking the best-fitting stellar population model which can account for the rest-frame UV-optical emission from the galaxy. This estimate of SFR is denoted here as SFR_{corr} (because it involves an obscuration ‘correction’). For most types of galaxy, with moderate dust obscuration, this approach is known to be as reliable as any other (e.g., Dunlop et al. 2017). Where available, we always used the *JWST* photometry for the SED fitting, and only used the *UltraVISTA* data for those objects that lack *NIRCam* imaging. Consistent with the fact that all of these galaxies have been detected in the (sub)mm, we allowed a large range of dust attenuation ($0 < A_V < 8$) during the fitting process. The ini-

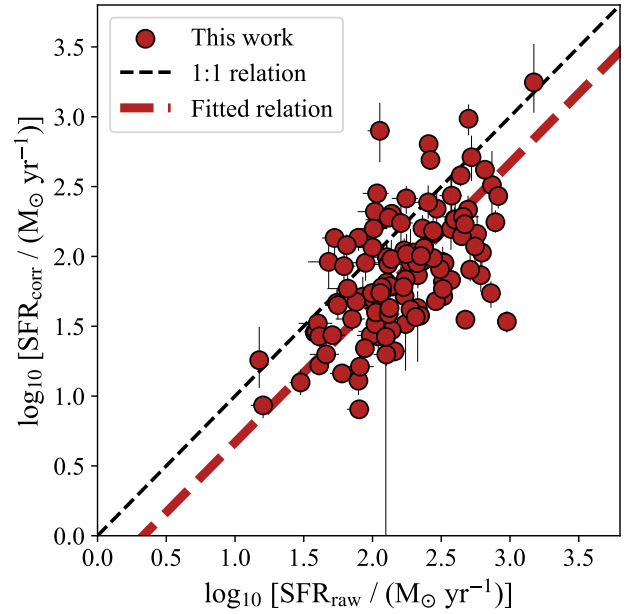


Figure 10. The values of SFR_{corr} (based on SED fitting with *BAGPIPES*) compared with the corresponding values of SFR_{raw} (created by adding the raw sub(mm) and raw UV-derived values of SFR). The fitted dashed red line (with a fixed slope of unity in log space) shows that, on average, SFR_{raw} is 0.33 dex larger than SFR_{corr} . Given this, and the obvious explanation that some of the star formation in these ALMA-detected galaxies is too obscured to be visible at all in optical-infrared regime used for the SED fitting, we adopt SFR_{raw} as the best estimate of SFR in all subsequent analysis.

tial parameter inputs to the *BAGPIPES* code are listed in Table 2. We note that this *BAGPIPES* SED fitting also yielded the stellar masses of the galaxies. These stellar mass estimates are also tabulated in Table A2, and are discussed further in the next subsection.

The second method we used to determine SFR may seem somewhat cruder, but it is less model dependent, and allows for the possibility that at least some of the star-formation activity in these ALMA-detected sources is actually *completely* hidden from view in the rest-frame UV-optical. This involves the calculation of what we term total ‘raw’ star-formation rate, SFR_{raw} by adding the dust-obscured SFR as determined from the (sub)mm photometry (SFR_{FIR}) to the UV-visible SFR (SFR_{UV}) as determined from the rest-frame UV emission *without* any correction for dust attenuation. For the reasons demonstrated and explained below, we ultimately adopted SFR_{raw} as the preferred most robust measure of SFR for the ALMA-detected galaxies under study here.

SFR_{FIR} is estimated from the observed-frame 1.3-mm continuum flux, using the conversion from Dunlop et al. (2017), which was based on the typical mid-far infrared SED displayed by the ALMA-detected galaxies in the Hubble Ultra Deep Field (HUDF), assuming a Chabrier IMF. Specifically we use the simple relation:

$$SFR_{\text{FIR}} (M_{\odot} \text{ yr}^{-1}) = 0.30 \times S_{1.3\text{mm}} (\mu\text{Jy}) \quad (2)$$

where, for each galaxy, the adopted 1.3-mm flux density $S_{1.3\text{mm}}$ and associated uncertainty was converted from the highest-S/N ALMA detection assuming the form of the (sub)mm SED follows $S_{\nu} \propto \nu^3$. We checked that the converted fluxes are all consistent with the greybody fit and other existing ALMA observations around the same frequency (see Fig. 6 for an example). We also verified that a calcu-

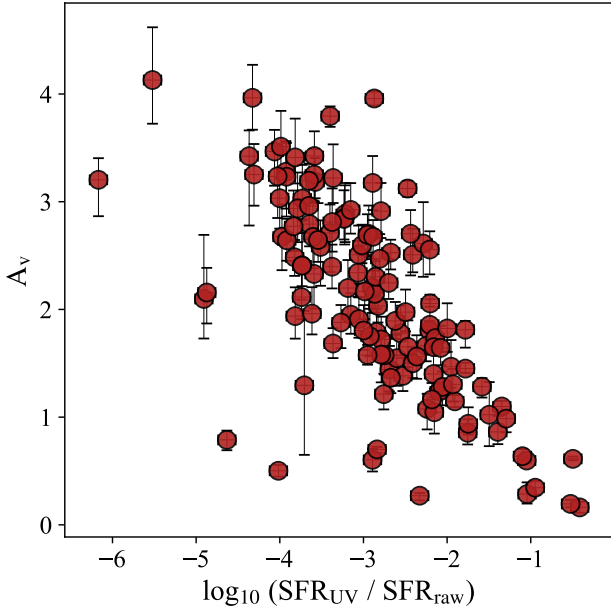


Figure 11. The values of dust attenuation, A_V derived from the optical-infrared SED fitting with BAGPIPES, plotted against the log of the ratio of raw UV and raw total SFR. Given that these are two different and independent measures of inferred obscuration, the strong correlation is reassuring. It can also be seen that the correlation is tighter for more modestly obscured sources where the SED fitting can provide a reasonable estimate of the dust attenuation.

lation of total FIR luminosity, $L_{8-1000\mu\text{m}}$, derived from integration of the fitted greybody curves, when converted to SFR (assuming, again, a Chabrier IMF) using the relation (McLure et al. 2018):

$$\log_{10}(\text{SFR}_{\text{FIR,integ}} / M_{\odot} \text{ yr}^{-1}) = \log_{10}(L_{8-1000\mu\text{m}} / W) - 36.44 \quad (3)$$

yields, on average, identical results to the simple mono-chromatic calculation of SFR_{FIR} described above.

The ‘raw’ SFR_{UV} is derived from the UV luminosity of each source at rest-frame $\lambda = 1500\text{\AA}$ (L_{1500} , as determined from the BAGPIPES SED fitting) using the relation:

$$\text{SFR}_{\text{UV}} (M_{\odot} \text{ yr}^{-1}) = \mathcal{K}_{\text{UV}} \times L_{1500\text{\AA}} (\text{erg s}^{-1} \text{ Hz}^{-1}) \quad (4)$$

where $\mathcal{K}_{\text{UV}} = 0.72 \times 10^{-28}$, corrected from a Salpeter IMF (Kennicutt 1998) to a Chabrier IMF (Madau & Dickinson 2014).

Finally, we note that one of our sources (ID 002, ALMA R.A. = 150.09991 deg, Dec. = 2.29722 deg) is known to be a lensed galaxy (Jin et al. 2024). Because derivation of its intrinsic physical properties requires much more complicated modeling than is required for the other sources in our sample, for this galaxy we adopted the values of SFR, M_* and A_V deduced by Jin et al. (2024), correcting the derived values by the magnification factor given there.

Fig. 9 shows the distribution of SFR for the 128 sources in our sample, as derived from these different methods. It can be seen that SFR_{FIR} dominates SFR_{UV} by on average a factor ≈ 100 . Quantifying this source-by-source via the ratio $\text{SFR}_{\text{UV}}/\text{SFR}_{\text{raw}}$, we find that the vast majority of the sources in the sample (125/128) are highly obscured with more than 80% of SFR_{raw} composed of SFR_{FIR} .

It can also be seen that the (FIR dominated) total SFR_{raw} for the

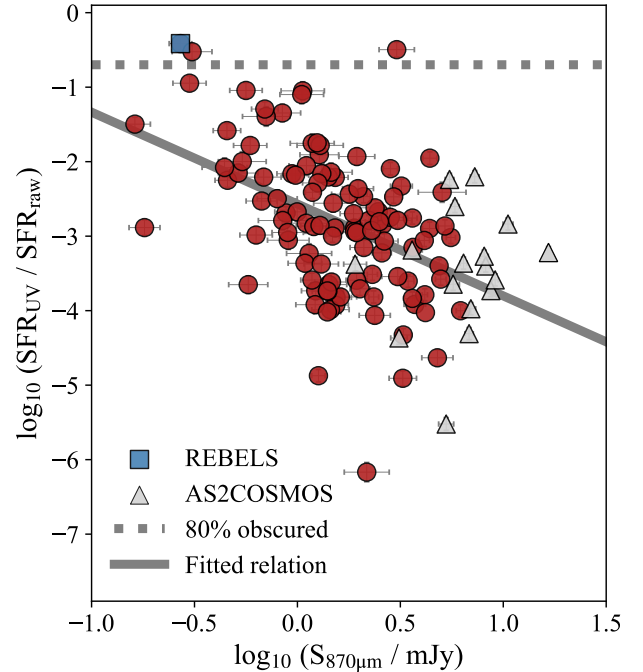


Figure 12. The level of dust attenuation, as quantified by the ratio of UV-visible to total SFR ($\text{SFR}_{\text{UV}}/\text{SFR}_{\text{raw}}$) plotted against the observed sub-mm flux density for each galaxy in our 128-source sample. All but 3 of the galaxies are more than 80% obscured. Moreover, while an anti-correlation is expected (see text), this plot confirms that the brightest (sub)mm sources are typically also the most heavily dust obscured as judged by this SFR ratio. We highlight the brightest and generally most heavily obscured sources in our sample which were also detected by AS2COSMOS (grey triangles, Simpson et al. 2020), as well as the one (relatively faint) (sub)mm source which also features in the REBELS sample (blue rectangle, Smit et al. 2018), and which was in practice first selected at rest-frame UV wavelengths (see text).

sample is generally higher than SFR_{corr} , confirming that, for this class of source, optical-infrared SED fitting runs the risk of underestimating the true SFR when at least some of the SFR in these galaxies is highly obscured. For the sample as a whole the offset between SFR_{raw} and SFR_{corr} is shown and quantified in Fig. 10, which reveals that while the two values are clearly well correlated, there exists an offset of ≈ 0.33 dex.

As a sanity check that our results are reasonable, in Fig. 11 we show that, reassuringly, the fitted value of dust attenuation, A_V , from the BAGPIPES SED fitting correlates well with $\text{SFR}_{\text{UV}}/\text{SFR}_{\text{raw}}$. Moreover, as expected (and discussed by Dunlop et al. 2017) the correlation is tightest for the less obscured galaxies in our sample, where less of the star formation is deeply obscured (and hence the SED fitting is more likely to yield unbiased results).

Finally, for completeness, in Fig. 12 we plot raw obscuration ($\text{SFR}_{\text{UV}}/\text{SFR}_{\text{raw}}$) versus the sub-mm flux density for all of the galaxies in our sample. An anti-correlation is arguably expected here (because SFR_{raw} is dominated by SFR_{FIR} which is proportional to $S_{870\mu\text{m}}$ according to Equation (2)) provided SFR_{UV} is not strongly related (correlated or anti-correlated) to SFR_{FIR} . Indeed, this is what is seen, with the best-fitting relation given by:

$$\log_{10} \frac{\text{SFR}_{\text{UV}}}{\text{SFR}_{\text{raw}}} = (-1.23 \pm 0.04) \times \log_{10} S_{870\mu\text{m}} (\text{mJy}) - (2.57 \pm 0.01) \quad (5)$$

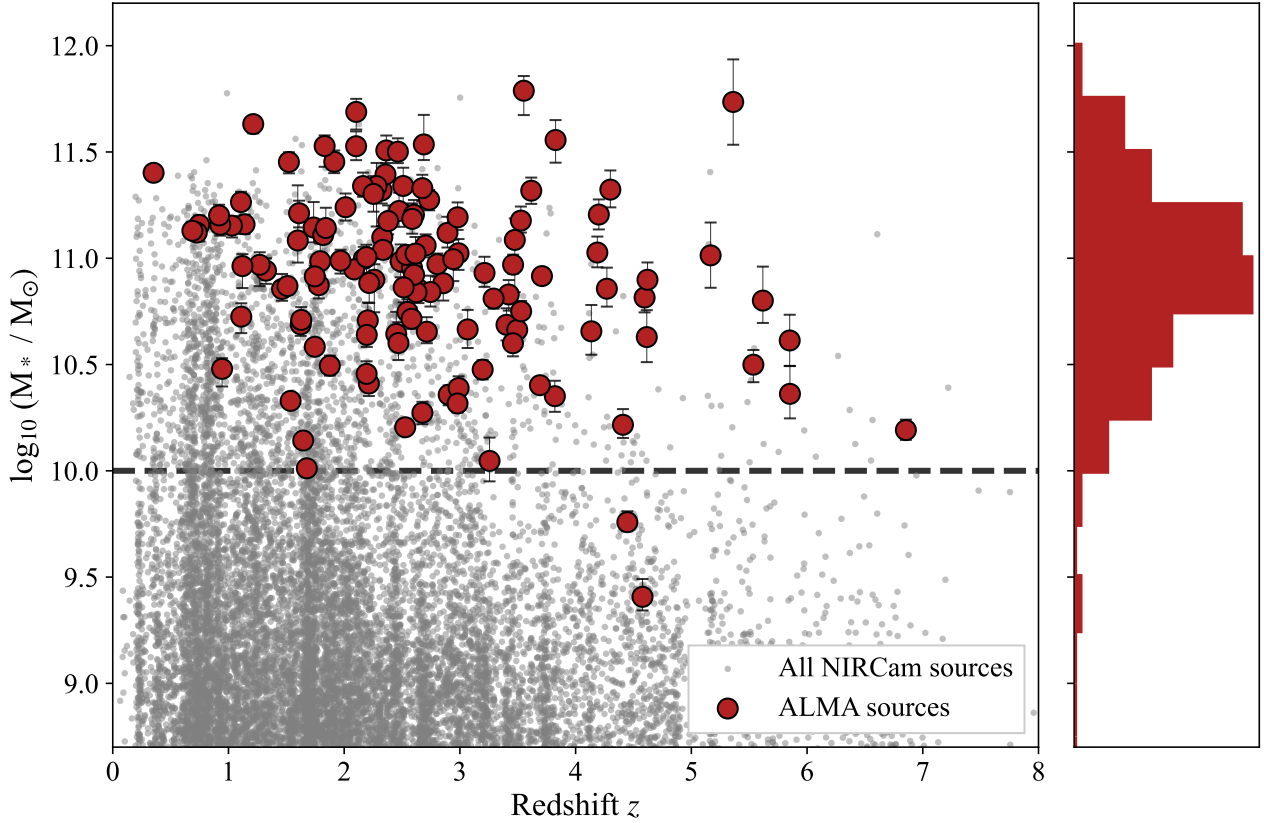


Figure 13. The stellar masses of all sources in the complete NIRCAM PRIMER COSMOS galaxy catalogue, plotted as a function of redshift (small grey dots). The 128 sources in our ALMA-detected sample are highlighted by the red filled circles and can be seen to be confined to the high-mass end of the galaxy mass distribution at all epochs. Specifically, almost all (126/128) having a stellar mass $M_* > 10^{10} M_\odot$ (a threshold indicated by the dashed horizontal line). It can also be seen that the ALMA detected subsample becomes an increasingly dominant subset of the general high-mass galaxy population with increasing redshift (at $z < 1$ the majority of such high-mass galaxies are known to be quiescent). The distribution of M_* for the ALMA-detected galaxies is shown in the right-hand panel. We remind the reader that because complete ALMA coverage of this field has not yet been achieved, several/many of the high-redshift high-mass NIRCAM sources plotted here in grey could yet transpire to be detectable in the (sub)mm given new ALMA observations.

In effect this plot, and the fitted relation, confirm that the galaxies which are brightest in the (sub)mm are indeed the most heavily obscured. We also use Fig. 12 to show how our sample connects the most luminous (and most dust-obscured) (sub)mm galaxies originally detected by SCUBA-2 in the field (i.e., the 17 AS2COSMOS sources) down to the much less luminous (sub)mm sources, which are in turn much less obscured as exemplified by the UV-selected REBELS source (ID 126) (for which SFR_{UV} is comparable to SFR_{FIR}).

4.2 Galaxy stellar masses

The stellar masses of all 128 ALMA-detected galaxies in our sample were determined by SED fitting with BAGPIPES as described in Section 4.1. The resulting values, which assume a Chabrier IMF, are tabulated for all the sources in Table A2 and plotted in Fig. 13. To place these results in context, in Fig. 13 we have also plotted the stellar masses (versus their redshifts) of all the galaxies in the NIRCAM PRIMER COSMOS catalogue (also derived with BAGPIPES) and highlight in red the sources that feature in our ALMA-detected sample (the stellar mass histogram for the ALMA-detected sources is projected into the right-hand panel).

From Fig. 13 it can be seen that virtually all (126/128) of the ALMA-detected galaxies have stellar masses, M_* , greater than the

mass threshold $M_* = 10^{10} M_\odot$, at all redshifts. Moreover, they extend upwards in mass to include the most massive galaxies in the field. This result echoes the results from the early blank-field ALMA surveys, such as those conducted in the Hubble Ultra Deep Field (HUDF; Bouwens et al. 2016; Dunlop et al. 2017), but the HUDF was too small a field to contain galaxies with $M_* > 10^{10} M_\odot$ at $z > 3$. Now, with the larger cosmological volumes sampled here by the PRIMER COSMOS field, it can be seen that this galaxy stellar mass threshold for bright (sub)mm emission applies back towards the epoch of reionisation.

It can also be seen that the ALMA-detected sample becomes an increasingly dominant subset of the general high-mass galaxy population with increasing redshift. Here we remind the reader that the ALMA ‘survey’ of the PRIMER COSMOS field utilised here is highly incomplete (being based simply on ≈ 100 pointings) and so the fraction of high-mass galaxies detected by ALMA (highlighted in red) is undoubtedly a lower limit. It is entirely possible, indeed likely, that many of the other high-mass galaxies in the field indicated by the grey dots in Fig. 13 will also yield (sub)mm detections if observed with ALMA. At the highest masses, $M_* > 10^{11} M_\odot$, the majority of the galaxies in the field at $z > 2$ are ALMA-detected. This reflects the fact that, within the ALMA-detected sample of galaxies under study here, it transpires that (sub)mm flux density, $S_{870\mu\text{m}}$, is

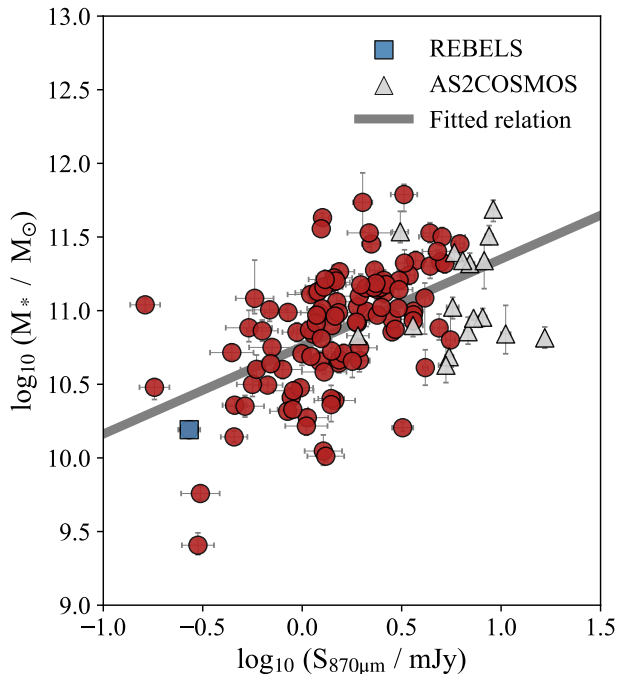


Figure 14. The relation between stellar mass and (sub)mm flux-density displayed by the 128 ALMA-detected galaxies in our sample. Again we highlight the 17 bright sources within our sample which were detected by the AS2COSMOS follow-up of the SCUBA-2 survey (Simpson et al. 2020; Gillman et al. 2024) and the one (UV-selected) REBELS source in our sample.

actually a rather strong function of stellar mass, as shown in Fig. 14. This is perhaps not unexpected, given the well-established strong stellar-mass dependence of dust attenuation in galaxies at $z \approx 2$ (e.g., McLure et al. 2018).

In summary, the clear implication of this still incomplete ALMA ‘survey’ is that virtually all massive galaxies ($M_* > 2 \times 10^{10} M_\odot$) at high redshift are dust-enshrouded star-forming galaxies, with the most massive being detectable in the (sub)mm with bright (but also reasonably complete) surveys as have been conducted with SCUBA-2. At lower redshifts, it can be seen that the ALMA-detected fraction of massive galaxies declines fairly rapidly at $z < 2$, with only a handful remaining at $z < 1$. This is as expected given that an increasing majority of the most massive galaxies at $z < 1.5$ are known to be quiescent, with most star-formation activity in such objects having been quenched by this epoch.

Finally, in Fig. 15, we plot the raw total value of SFR (derived and discussed in Section 4.1) for each galaxy versus its stellar mass. This allows us to explore where the ALMA-detected galaxies in our sample lie relative to the so-called ‘main sequence’ (MS) of star-forming galaxies. There is quite a lot of scatter in this plot, but this is probably realistically due to the fact that SFR_{raw} and M_* have been derived in a completely independent manner (as compared to studies where SFR and M_* are *both* derived from SED fitting). Nonetheless, there is enough dynamic range in our sample for it to be clear that these galaxies, with a few possible exceptions, lie on the MS (Speagle et al. 2014). Moreover, dividing our sample into a low-redshift half and a high-redshift half (around the median redshift, $z_{\text{med}} = 2.52$) there is enough signal to reveal the redshift evolution of the MS, and hence infer the redshift dependence of the typical specific SFR (sSFR) of the ALMA-detected galaxies. This

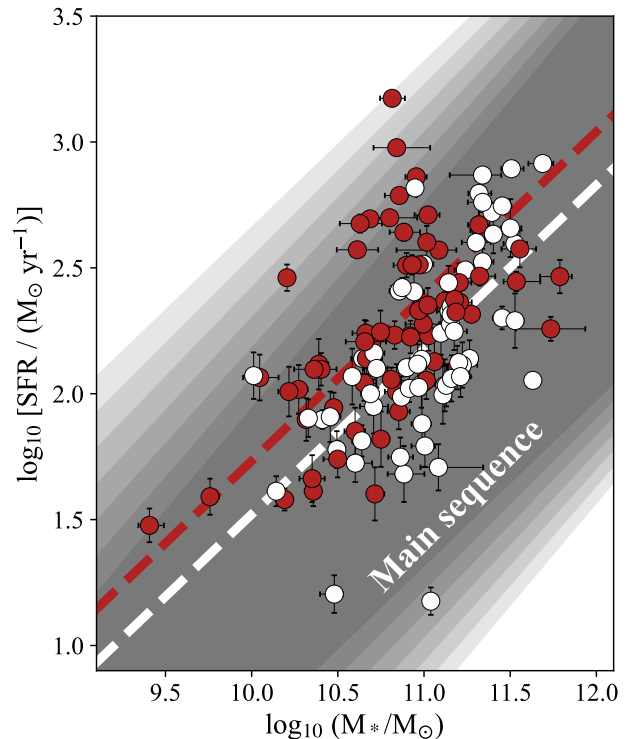


Figure 15. Star-formation rate (SFR_{raw} plotted versus stellar mass (M_*) for the 128 ALMA-detected galaxies. Shown in grey is the region occupied by ‘normal’ star-forming galaxies - the so-called main sequence (MS) over the redshift range $z = 1 - 7$ (Speagle et al. 2014). Despite the (arguably realistic) scatter it is clear that the vast majority of the ALMA-detected galaxies lie on the MS, suggesting that these galaxies are representative of star-forming galaxies over most of cosmic time. As shown here the sample is divided in half into a low-redshift group (white filled circles) and a high-redshift group (red filled circles) around the median redshift of the sample ($z_{\text{med}} = 2.52$). The two groups exhibit a ≈ 0.2 dex difference in normalisation (i.e., sSFR) when fitted with a linear relation with the same slope (fitted from the low-redshift group) under the logarithmic scale, showing that our sample is powerful enough to reveal the redshift evolution of the MS.

information becomes important in the final analysis section below, where we attempt to correct for the incompleteness in our ALMA ‘survey’ in order to properly estimate the redshift evolution of dust-enshrouded star-formation rate density.

4.3 Cosmic star formation history

Finally, we used our results to make a new estimate of the contribution of dust-enshrouded star formation to cosmic star-formation history, reaching back to $z \approx 7$. Here we made two calculations.

4.3.1 Star-formation rate density from the ALMA sources

First, we simply calculated the cosmic history of dust-enshrouded star-formation rate density, $\rho_{\text{SFR IR}}$, on the basis of the 128 ALMA-detected galaxies studied here. Because this ALMA ‘survey’ of the PRIMER COSMOS field simply consists of a series of individual pointings, it is inevitably highly incomplete (except at the very bright end where the AS2COSMOS ALMA sources were originally uncovered by the contiguous SCUBA-2 CLS survey). This means that the result of summing the SFR contributions of the ALMA sources in

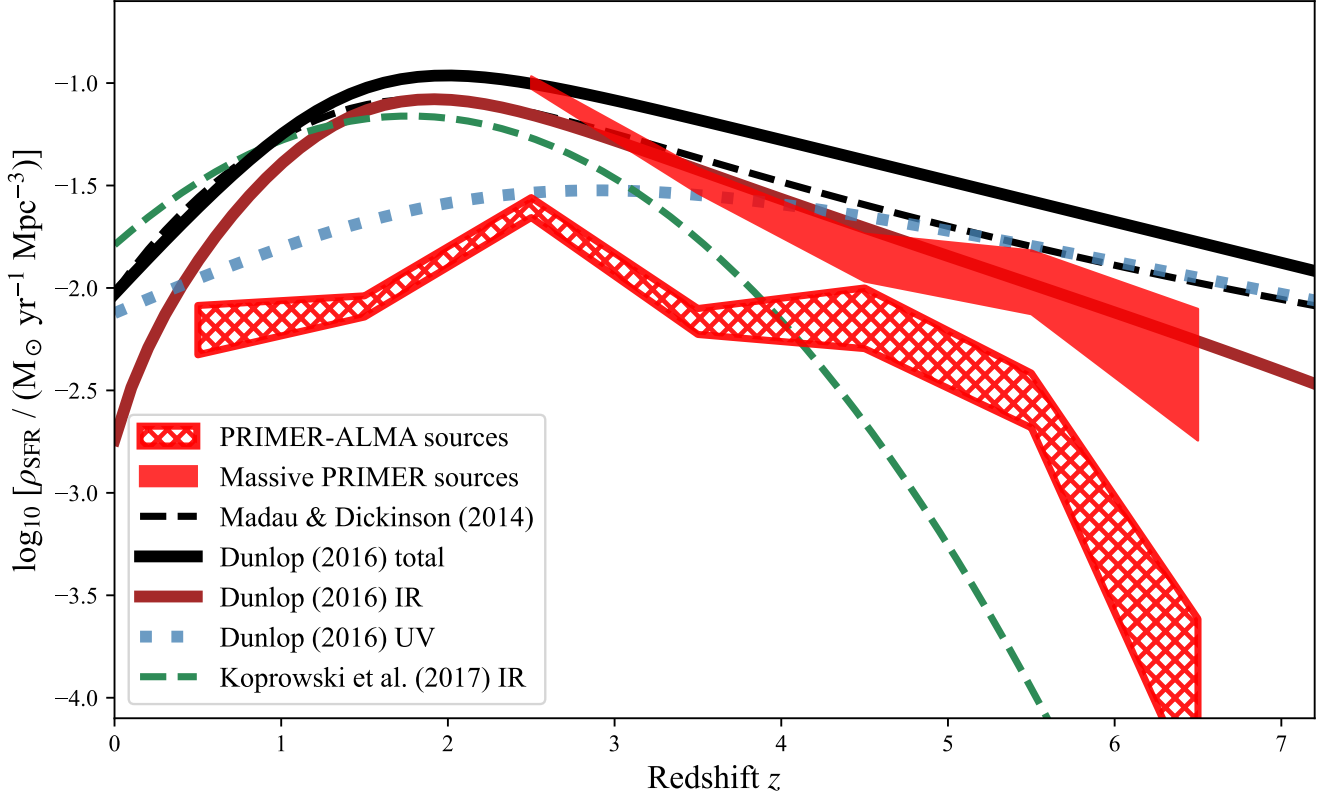


Figure 16. Co-moving cosmic star-formation rate density, ρ_{SFR} . The contribution made by dust-enshrouded star formation ($\rho_{\text{SFR,IR}}$) as calculated directly from the 128 ALMA-detected galaxies in our sample is shown (in integer redshift bins) by the cross-hatched red region. In effect, given the high incompleteness of the ALMA coverage of the COSMOS PRIMER field, this represents a hard lower limit to the true contribution of dust-enshrouded galaxies. Our corrected version of $\rho_{\text{SFR,IR}}$, derived by adding in the anticipated contributions of other massive ($M_* > 10^{10} M_\odot$) galaxies in the field is plotted for comparison: the total ρ_{SFR} from Madau & Dickinson (2014) (corrected to a Chabrier IMF), the total, obscured and UV-visible values of ρ_{SFR} from Dunlop (2016), and the extrapolated contribution of obscured star formation inferred by Koprowski et al. (2017). The very rapid drop in dust-obscured star-formation activity suggested by Koprowski et al. (2017) can be excluded, even by our raw ALMA-only results, while our final incompleteness-corrected results are in excellent agreement with the relation for $\rho_{\text{SFR,IR}}$ given by Dunlop (2016).

our sample can only yield a lower limit to $\rho_{\text{SFR,IR}}$ as a function of redshift/time. However, this lower limit is robust, and significantly higher (and hence more useful) than the results achieved by simply summing the contributions of the very bright A2SCOSMOS sources (of which there are only 17 in our sample).

The results of this calculation, in integer redshift bins ($z = 0 - 1$, $z = 1 - 2$ etc), are tabulated in the second row of Table 3. The error in each redshift bin was estimated by bootstrapping, where we randomly re-sampled the galaxies 10,000 times in each redshift bin and calculated the standard deviation of all 10,000 runs. We also calculated the errors in each bin resulting from the propagation of the individual errors in SFR_{raw} for each galaxy and from the overall sampling uncertainty, but found that these errors were relatively small compared to those calculated from the bootstrap analysis.

These values, and the associated errors are plotted as the *cross-hatched* red band in Fig. 16. The resulting ‘curve’ rises by two orders-of-magnitude from $z \approx 7$ to a peak at cosmic noon ($z \approx 2.5$) before declining by ≈ 0.5 dex by $z \approx 0.5$. Unsurprisingly, given that this curve essentially represents a lower limit on $\rho_{\text{SFR,IR}}$, this curve lies below previous estimates of total ρ_{SFR} (e.g., Madau & Dickinson 2014; Dunlop 2016), but interestingly it already lies above some estimates of the high-redshift evolution of $\rho_{\text{SFR,IR}}$ based on certain functional extrapolations from lower redshift (sub)mm detections (e.g., Koprowski et al. 2017). It is also notable that, at $z \approx 2.5$, this

incomplete determination of $\rho_{\text{SFR,IR}}$ essentially matches the value of $\rho_{\text{SFR,UV}}$ as indicated by the dotted blue curve in Fig. 16, which is given by the equation

$$\rho_{\text{SFR,UV}} = \frac{0.055}{10^{-0.38(z-2.2)} + 10^{0.16(z-2.2)}} \quad (6)$$

as derived by Dunlop (2016). However, this is perhaps not surprising, given that a full calculation of $\rho_{\text{SFR,IR}}$ from complete ALMA surveys such as those conducted in the HUDF, shows that $\rho_{\text{SFR,IR}}$ dominates $\rho_{\text{SFR,UV}}$ at cosmic noon (Dunlop et al. 2017; Bouwens et al. 2020; Zavala et al. 2021).

4.3.2 Final incompleteness-corrected star-formation rate density

Second, armed with the *full* galaxy sample in the PRIMER COSMOS NIRCcam imaging resulting from the deep *JWST+HST* observations (including derived photometric/spectroscopic redshifts and stellar masses), we have attempted to correct for the incompleteness in our ALMA survey. This calculation was primarily motivated by Fig. 13, which confirms that essentially all the ALMA-detected galaxies are massive with $M_* > 10^{10} M_\odot$, but that there remain many comparably massive galaxies in the full PRIMER COSMOS catalogue that have yet to be observed with ALMA. We therefore proceeded to estimate

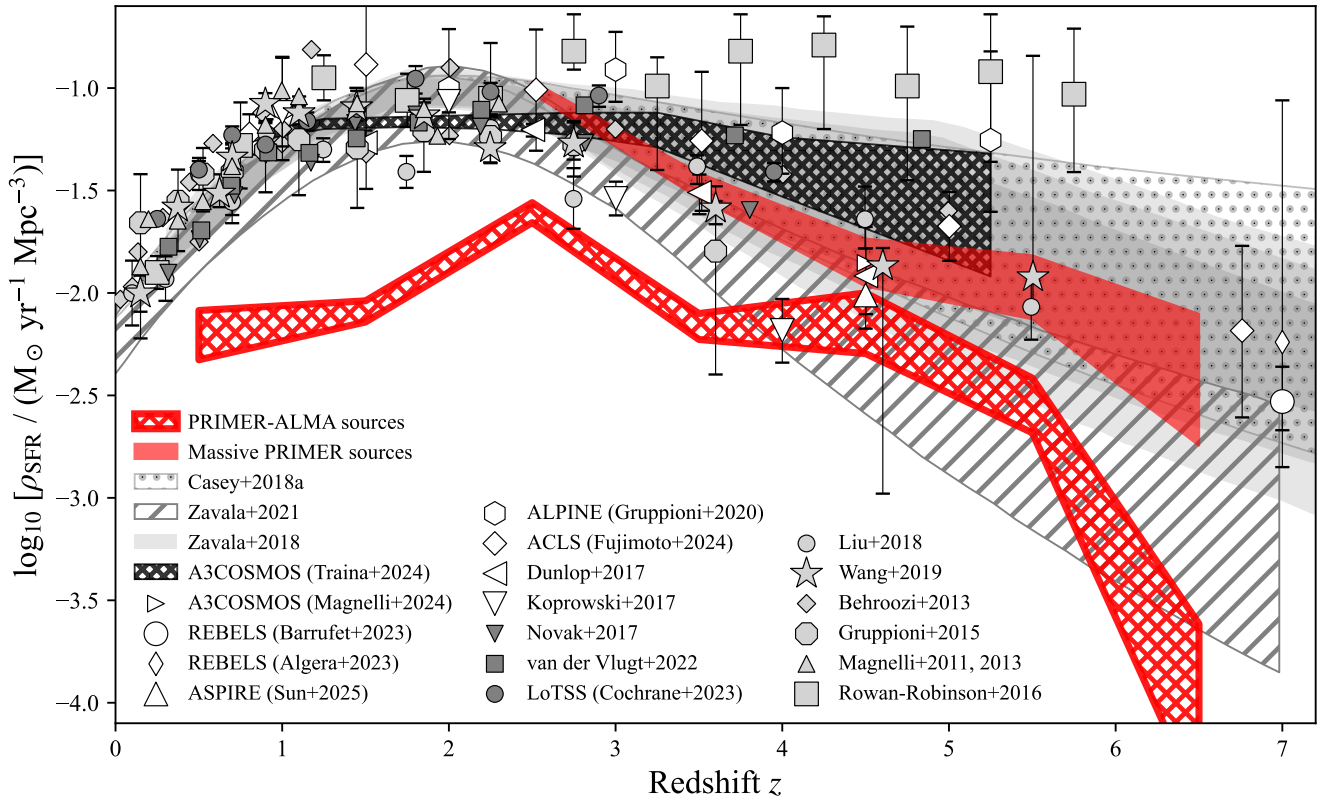


Figure 17. Our raw and incompleteness-corrected results for dust-obscured $\rho_{\text{SFR IR}}$ as shown above in Fig. 16, but this time compared with a compilation of results for obscured star-formation rate density from the literature. White data-points are derived from (sub)mm observations, light-grey points are from mid-to-far-infrared observations, and dark-grey data-points are from data at other wavelengths (e.g., radio observations). Data include Magnelli et al. (2011, 2013), a collection of IR observations in Behroozi et al. (2013), Gruppioni et al. (2015), Rowan-Robinson et al. (2016), Koprowski et al. (2017), Novak et al. (2017), Liu et al. (2018), Zavala et al. (2018) (fitted from models in Casey et al. 2018a,b, colours lightened from 68% to 99.7% confidence interval), Casey et al. (2018a) (dust-rich and dust-poor models as upper and lower borders), Wang et al. (2019), ALPINE (Gruppioni et al. 2020), Zavala et al. (2021), van der Vlugt et al. (2022), REBELS (Algera et al. 2023; Barrufet et al. 2023b), LoTSS (Cochrane et al. 2023), ACLS (Fujimoto et al. 2024), A³COSMOS (Magnelli et al. 2024; Traina et al. 2024), ASPIRE (recalculated from Sun et al. 2025).

Table 3. Calculated estimates of co-moving cosmic star-formation rate density, ρ_{SFR} , as a function of redshift. The first row indicates the redshift bins, with the second row giving the contribution to ρ_{SFR} made by the 128 ALMA-detected galaxies in our sample ($\rho_{\text{SFR mm}}$). The third row shows the result of our efforts to correct for the incompleteness of the ALMA ‘survey’ used here, by assigning dust-obscured SFR estimates to all galaxies in the *JWST* PRIMER COSMOS sample with $M_* > 10^{10} M_\odot$, assuming a sSFR as derived from the ALMA-detected galaxies at comparable redshifts. This latter calculation is confined to $z > 2$ because, at lower redshifts, it is unreasonable to assume that the vast majority of massive galaxies are star-forming. This final row thus gives our best incompleteness-corrected estimate of the evolution of dust-obscured star-formation rate density, $\rho_{\text{SFR IR}}$, from $z \approx 2$ to $z \approx 7$. Errors are calculated from bootstrapping and propagated to the logarithmic scale. The bootstrapping for $\rho_{\text{SFR IR}}$ used a perturbation method to reflect the uncertainty in the measurement of SFR (see Section 4.3).

| Redshift range | $0 < z \leq 1$ | $1 < z \leq 2$ | $2 < z \leq 3$ | $3 < z \leq 4$ | $4 < z \leq 5$ | $5 < z \leq 6$ | $6 < z \leq 7$ |
|---------------------------------|------------------|------------------|------------------|------------------|------------------|------------------|------------------|
| $\log_{10}\rho_{\text{SFR mm}}$ | -2.21 ± 0.12 | -2.09 ± 0.05 | -1.61 ± 0.05 | -2.16 ± 0.06 | -2.15 ± 0.15 | -2.55 ± 0.13 | -4.05 ± 0.43 |
| $\log_{10}\rho_{\text{SFR IR}}$ | - | - | -1.00 ± 0.03 | -1.48 ± 0.06 | -1.85 ± 0.12 | -1.97 ± 0.16 | -2.42 ± 0.32 |

the additional contribution to $\rho_{\text{SFR IR}}$ that would be made by these other massive galaxies in the field, on the assumption that their properties are similar to those of the ALMA-detected objects at comparable redshift and of comparable stellar mass.

In detail, we proceeded as follows. Firstly, we calculated the sSFR of each ALMA source, and fitted the sSFR as a function of redshift for the 128 ALMA sources. This gives:

$$\log_{10}\text{sSFR} (\text{yr}^{-1}) = (0.10 \pm 0.04) \times z - (8.88 \pm 0.14) \quad (7)$$

fitted over the redshift range $0 < z < 7$. We then required the NIRCcam

sources in the PRIMER COSMOS catalogue to have a SED-fitted $M_* > 10^{10} M_\odot$, to also have $\text{S/N} > 10$ in the F356W imaging (already true for almost all high-mass galaxies in the sample), and for the SED fitting to achieve a reduced $\chi^2_\nu < 5$. We also carefully checked the photometric redshift solutions, especially in the highest redshift bins, to exclude any sources with unreliable redshift estimates. The fitted sSFR from the ALMA sample as given by Equation (7) is then applied to the SED-fitted M_* values of all the galaxies in this cleaned high-mass galaxy sample, which contained 2,225 sources in total. The deduced SFR, SFR_{SFR} , has an error propagated from both the uncertainty in the individual values of M_* and the uncertainty in the

fitted z -sSFR relation. We then calculated the contribution to ρ_{SFR} made by this much larger galaxy sample as a function of redshift, calculating the appropriate cosmological volumes corresponding to the 142.2 arcmin² of NIRCcam coverage. During the error derivation, we perturbed the SFR_{sSFR} of each galaxy with its error, and ran bootstrap on the perturbed sample in each redshift bin 10,000 times. This approach effectively includes both the unperturbed bootstrapped error from the original sample and the uncertainty in the measured SFR_{sSFR} of each massive galaxy.

In essence, this calculation corresponds to assuming that the massive galaxies in the field which have not been observed by ALMA have a similar sSFR to the ALMA-detected galaxies at each redshift, and that the resulting inferred SFR for these massive galaxies is overwhelmingly dust enshrouded. The latter assumption is relatively safe, given the properties of the ALMA-detected galaxies studied here, and indeed the properties of all known high-mass star-forming galaxies. The former assumption is likely also reasonable at high-redshift (where quiescent galaxies are extremely rare) but becomes dubious at lower redshift and obviously is completely incorrect by the present day (when the vast majority of massive galaxies are passive). We therefore restricted this calculation to $z > 2$.

These resulting ‘corrected’ values of $\rho_{\text{SFR IR}}$, derived by adding the directly-measured contributions of those massive galaxies detected by ALMA to the estimated additional contributions of the other high-mass galaxies in the field, are tabulated in the third row of Table 3, again in integer redshift bins but this time only for $z > 2$. These values, and the associated errors are plotted as the bright filled red band in Fig. 16. At $z > 3$ this still lies reassuringly below previous estimates of total ρ_{SFR} shown in Fig. 16 as derived by Madau & Dickinson (2014) (converted to a Chabrier IMF; dashed black curve) or Dunlop (2016) (solid black curve) where the latter relation is given by:

$$\rho_{\text{SFR total}} = \frac{0.175}{10^{-0.9(z-1.4)} + 10^{0.2(z-1.4)}} \quad (8)$$

Interestingly, however, our ‘corrected’ evolution of $\rho_{\text{SFR IR}}$ (as indicated by the bright filled red band) in fact follows rather well the evolution of dust-enshrouded SFR density inferred by Dunlop (2016) by simply subtracting Equation (6) from Equation (8), *i.e.*:

$$\rho_{\text{SFR IR}} = \rho_{\text{SFR total}} - \rho_{\text{SFR UV}} \quad (9)$$

which is plotted as the solid brown curve in Fig. 16. This new measurement of $\rho_{\text{SFR IR}}$ at $z > 2$ presented here thus appears to confirm the conclusions of several previous studies that $z \approx 4$ represents the transition redshift between $\rho_{\text{SFR IR}}$ and $\rho_{\text{SFR UV}}$ with UV visible SFR becoming increasingly dominant at all higher redshifts (Dunlop et al. 2017; Magnelli et al. 2024). We note that this high-redshift decline of the relative contribution of dust-enshrouded star formation to $\rho_{\text{SFR total}}$ can be explained simply by the relative rarity of high-mass galaxies ($M_* > 10^{10} M_{\odot}$) at early times, as is evident from Fig. 13.

Whilst massive quiescent galaxies are known to be rare at $z > 2$, an unexpectedly large number of such objects have been found in early JWST data. We therefore perform a check on our assumption that all massive $z > 2$ galaxies in the field have SFRs comparable to our ALMA sample by excluding the robust $z > 2$ quiescent galaxy sample of Stevenson et al. (in prep) from our estimate. This sample was selected via a BAGPIPES fitting approach described in Carnall et al. (2023), which has now been extensively spectroscopically validated (Carnall et al. 2024). This robust quiescent sample has 37 objects in common with our high-mass PRIMER COSMOS galaxy sample

(though none in our ALMA-detected sample), the removal of which reduces our ‘corrected’ measure of $\rho_{\text{SFR IR}}$ by $\approx 9\%$ in our $2 < z \leq 3$ bin and $\approx 4\%$ in our $3 < z \leq 4$ bin. We therefore conclude that the presence of massive quiescent galaxies at $z > 2$ in PRIMER COSMOS does not strongly affect our $\rho_{\text{SFR IR}}$ estimates.

Finally, in Fig. 17 we again show our new raw and corrected estimates of the evolution of dust-enshrouded star-formation rate density, $\rho_{\text{SFR IR}}$, but this time compared against a broad range of recent results from the literature. In general it can be seen that our results now categorically exclude most of the very high values of $\rho_{\text{SFR IR}}$ at $z > 3$ proposed by Rowan-Robinson et al. (2016), Casey et al. (2018a), Gruppioni et al. (2020), and Khusanova et al. (2021) before the advent of JWST. They also exclude almost all of the (highly-uncertain) region suggested by Traina et al. (2024) from their recent analysis of the wider A³COSMOS sample (where the redshift information is in general much poorer than achieved here), and the upper regions of the uncertain high-redshift extrapolation proposed by Zavala et al. (2018). By contrast, our results are consistent with the upper end of the range derived by Zavala et al. (2021), align well with the results of Dunlop et al. (2017) out to $z \approx 4$, and are completely consistent with the result derived at $z \approx 4.5$ by Magnelli et al. (2024) from A3COSMOS. At the highest redshifts, our results are in excellent agreement with the evolution of dust-enshrouded $\rho_{\text{SFR IR}}$ inferred by Wang et al. (2019) and our measurement is consistent with the values derived at $z \approx 7$ from the REBELS survey (Algera et al. 2023; Barrufet et al. 2023b) and from the ACLS (Fujimoto et al. 2024), albeit some of these previous $z \approx 7$ measurements are highly uncertain.

In summary, while a complete ALMA survey of the PRIMER COSMOS field remains a highly desirable (albeit demanding) observational goal, through the analysis of the existing fairly dense ALMA observations of the field, in tandem with the PRIMER COSMOS JWST+HST+VISTA near/mid-infrared imaging, we have been able to derive a new estimate of the high-redshift evolution of dust-enshrouded star-formation rate density which is significantly more complete, robust and well-constrained than previously achieved. Solutions in which dust-enshrouded star-formation rate density ($\rho_{\text{SFR IR}}$) exceeds UV-visible star-formation rate density ($\rho_{\text{SFR UV}}$) at $z > 5$ are now effectively excluded by our analysis, even when we make the assumption that all massive galaxies in the field at $z > 2$ are as highly star-forming as the 128 ALMA-detected sources studied in detail here. That said, dust-enshrouded star formation clearly persists to higher redshifts than inferred from some earlier extrapolations from lower-redshift ALMA studies, but $\rho_{\text{SFR IR}}$ is certainly lower at high redshift than inferred from many earlier investigations, especially those based on (relatively) poor-resolution *Herschel* surveys, which in many cases lacked secure galaxy identifications with robust redshift information.

In this study we have benefited from high-quality, high-resolution ALMA and JWST imaging, along with secure redshift information aided by the pleasing fact that 52% of the ALMA-detected sources in our sample possess secure spectroscopic redshifts. The availability of a high-quality underlying galaxy sample in the same field is also an unusual asset, which has helped us to compensate for the lack of complete ALMA imaging. Our final result for the high-redshift evolution of dust-enshrouded star-formation rate density, $\rho_{\text{SFR IR}}$, transpires to be very well described by the relation given by Dunlop (2016) (and provided explicitly here in Equation (9) from the difference between Equations (8) and (6)), as shown in Fig. 16. Extrapolation of our results (according to this relation) predicts that, by $z \approx 8$, dust-enshrouded star-formation activity is expected to con-

tribute only 20% of the total cosmic star-formation rate density, ρ_{SFR} , with this contribution dropping to $\approx 5\%$ by $z = 10$.

Of course, these are simply extrapolations, and the results presented here do not provide direct constraints beyond $z \approx 7$. Nonetheless, this serves to demonstrate that even given the evidence that UV-visible star formation dominates at $z > 4$, dust may still be present at $z > 10$. This possibility is not yet ruled out by recent reports that galaxies discovered with *JWST* at $z \approx 11$ are largely dust-free (e.g., Cullen et al. 2024, 2025; Ferrara et al. 2025) because the galaxy samples uncovered to date at such early times have yet to reveal galaxies with stellar masses $M_* > 10^{10} M_{\odot}$ (Donnan et al. 2024, 2025), should they exist.

5 SUMMARY & CONCLUSIONS

We have used the wealth of archival ALMA data in the COSMOS field to assemble a robust sample of 128 unique (sub)mm sources that lie within the central $\approx 175 \text{ arcmin}^2$ region covered by the new *JWST* NIRCam and MIRI imaging from the PRIMER survey. This ALMA sample, being assembled from numerous pointed follow-up observations, does not represent a complete (sub)mm survey of the field. However, it spans two orders-of-magnitude in terms of sub-mm flux density, $S_{870 \mu\text{m}}$, enabling us to explore the properties of dust-enshrouded star-forming galaxies from the brightest (sub)mm emitters uncovered by wide-area single-dish surveys (AS2COSMOS detected 17 of the 128 sources in our sample) down to the much fainter (sub)mm emitters recently uncovered by, for example, the REBELS programme.

The depth, red sensitivity, and high angular resolution (and hence high positional accuracy) of the *JWST* observations have enabled us to identify a secure and unique galaxy counterpart for *every one* of the 128 ALMA sources in our sample (aided, of course, by the high positional accuracy provided by ALMA). This unusually high level of 100% identification completeness is accompanied by a pleasingly high level of redshift completeness: an extensive search of the optical-infrared-millimetre spectroscopic literature revealed that 52% of the sources in our sample have secure spectroscopic redshifts. This spectroscopic redshift information (extending to $z \approx 7$), coupled with the extensive multi-frequency photometry provided by *JWST* PRIMER (and, where necessary/helpful, UltraVISTA), has enabled us to produce robust photometric redshifts for the galaxies in the remaining half of the ALMA-detected sample (checked, where possible, by the plausibility of multi-band ALMA photometry). We provide the positions and basic photometric properties of all 128 sources in Appendix A, Table A1, with colour postage-stamp images of all the galaxies presented in Appendix B, Figure B1.

Armed with this unusually complete and robust information, we undertook a detailed exploration of the basic physical properties of the ALMA-detected galaxies. We made 3 different estimates of SFR for each source: (1) the SFR inferred from fitting the optical-infrared SED allowing for dust attenuation (using BAGPIPES), (2) the ‘raw’ UV-visible SFR, calculated from the emission at $\lambda_{\text{rest}} = 1500 \text{ \AA}$, and (3) the ‘raw’ dust-obscured SFR inferred from the (sub)mm photometry. As expected for (sub)mm detected sources, SFR measure (3) (i.e., the SFR inferred from the (sub)mm) was found to be much larger than SFR measure (2), with the raw UV-visible SFR being essentially negligible in comparison for most sources. Nonetheless, for completeness, we added SFR measures (2) and (3) to obtain a best estimate of total ‘raw’ SFR, independent of the SED fitting. As has been shown in previous studies, we found that SFR estimate (1) works well for moderately obscured sources, but falls short of the total raw

(sub)mm+UV SFR for the more highly-obscured objects. Thus, for all subsequent analysis, we adopted the total ‘raw’ SFR (although we provide all SFR measures for all the sources in Appendix A, Table A2). The star-formation rates of the ALMA-detected sources range from $\text{SFR} \approx 500 M_{\odot} \text{ yr}^{-1}$ down to $\text{SFR} \approx 30 M_{\odot} \text{ yr}^{-1}$, reflecting the high dynamic range of our sample.

We used the BAGPIPES SED fitting to determine the stellar masses, M_* of all the ALMA-detected galaxies, as well as the masses of all other galaxies in the field imaged with *JWST*. Consistent with previous studies, we found that virtually all (126/128) of the ALMA-detected galaxies have high stellar masses, $M_* > 10^{10} M_{\odot}$, but we are now able to show that this appears to be *independent of redshift*, at least out to $z \approx 7$ (the effective redshift limit of the present study). Plotting the completely independent measures of ‘raw’ total SFR against M_* we find that, with very few exceptions, the ALMA-detected sources lie on the evolving ‘main sequence’ (MS) of star-forming galaxies, and we are able to use our data to establish the sSFR of the ALMA-detected galaxies as a function of redshift (i.e., the redshift evolution of the MS).

The unusually high quality of our sample (in terms of robust and complete redshift and SFR information) has enabled us to make a robust estimate of the contribution of the ALMA-detected galaxies to cosmic star-formation rate density, ρ_{SFR} . However, this represents only a lower limit (albeit a robust one, which can already exclude some previous estimates), to the true contribution of dust-enshrouded activity to cosmic star-formation rate density. This is because, as mentioned above, despite delivering 128 sources, the ALMA imaging is highly incomplete, with the individual pointings covering $< 20\%$ of the PRIMER COSMOS area. We therefore used our knowledge of all other comparably massive galaxies in the field (yet to be observed with ALMA), to produce a new, completeness-corrected estimate of dust-enshrouded ρ_{SFR} from $z \approx 2$ out to $z \approx 7$.

Our new relatively well-constrained estimate of the high-redshift evolution of dust-enshrouded $\rho_{\text{SFR,IR}}$ is accurate enough to now rule out several previous claims that dust-enshrouded SFR continues unabated beyond cosmic noon. Instead, it confirms the conclusions of several other recent studies that UV-visible star formation dominates ρ_{SFR} beyond $z \approx 4 - 5$, a result that can be explained simply by the inevitable decline in the numbers of massive galaxies at high redshift (rather than requiring a change in the nature of dust). We note that our final our results at $z > 2$ align very well by the parametric fit to the evolution of dust-enshrouded $\rho_{\text{SFR,IR}}$ derived by Dunlop (2016). Further extrapolation of this relation indicates that, while dust-enshrouded star formation inevitably continues to decline with increasing redshift, it could still have made a significant contribution at higher redshifts, amounting to most likely $\approx 20\%$ of total ρ_{SFR} at $z \approx 8$, and potentially still as much as $\approx 5\%$ at $z \approx 10$.

Finally, we note that to improve on this study really requires the provision of deep, complete and contiguous ALMA imaging of the PRIMER COSMOS field, to remove the need for the incompleteness correction to $\rho_{\text{SFR,IR}}$ for high-mass galaxies applied here (which could in fact have led to an over-estimate) and to enable stacking to assess the contribution of galaxies with $M_* < 10^{10} M_{\odot}$ (as previously undertaken in much smaller fields such as the HUDF). That said, the quality of the available *JWST* data means that our current 128-source sample still merits further investigation, and we will present the results of a more detailed analysis of the morphologies and SED properties of the ALMA-detected PRIMER COSMOS galaxies in a subsequent paper.

ACKNOWLEDGEMENTS

JSD, DJM and LB acknowledge the support of the Royal Society through the award of a Royal Society University Research Professorship to JSD. DJM, CD, RJM, and JSD acknowledge the support of the UK Science and Technology Facilities Council (STFC). ACC and SDS acknowledge support from a UKRI Frontier Research Guarantee Grant (PI Carnall; grant reference EP/Y037065/1). RSE acknowledges financial support from the Peter and Patricia Gruber Foundation. FC acknowledges support from a UKRI Frontier Research Guarantee Grant (PI Cullen; grant reference EP/X021025/1). RB acknowledges support from an STFC Ernest Rutherford Fellowship [grant number ST/T003596/1].

This work is based in part on observations made with the NASA/ESA/CSA *James Webb Space Telescope*. The data were obtained from the Mikulski Archive for Space Telescopes at the Space Telescope Science Institute, which is operated by the Association of Universities for Research in Astronomy, Inc., under NASA contract NAS 5-03127 for JWST. This work is based in part on observations obtained with the NASA/ESA Hubble Space Telescope, retrieved from the Mikulski Archive for Space Telescopes at the Space Telescope Science Institute (STScI). STScI is operated by the Association of Universities for Research in Astronomy, Inc. under NASA contract NAS 5-26555. This work is also based in part on observations made with the Spitzer Space Telescope, which is operated by the Jet Propulsion Laboratory, California Institute of Technology under NASA contract 1407. ALMA is a partnership of ESO (representing its member states), NSF (USA), and NINS (Japan), together with NRC (Canada), MOST and ASIAA (Taiwan), and KASI (Republic of Korea), in cooperation with the Republic of Chile. The Joint ALMA Observatory is operated by ESO, AUI/NRAO, and NAOJ. This work is based in part on VISTA observations collected at the European Southern Observatory under ESO programme ID 179.A-2005 and 198.A-2003 and on data products produced by CALET and the Cambridge Astronomy Survey Unit on behalf of the UltraVISTA consortium. This work is based in part on observations obtained with MegaPrime/MegaCam, a joint project of CFHT and CEA/IRFU, at the Canada–France–Hawaii Telescope (CFHT) which is operated by the National Research Council (NRC) of Canada, the Institut National des Science de l’Univers of the Centre National de la Recherche Scientifique (CNRS) of France, and the University of Hawaii. This work is based in part on data products produced at Terapix available at the Canadian Astronomy Data Centre as part of the Canada–France–Hawaii Telescope Legacy Survey, a collaborative project of NRC and CNRS. Some of the NIRSpec data products utilised here to provide spectroscopic redshifts were retrieved from the Dawn JWST Archive (DJA). DJA is an initiative of the Cosmic Dawn Center (DAWN), which is funded by the Danish National Research Foundation under grant DNRF140. This research used the facilities of the Canadian Astronomy Data Centre operated by the National Research Council of Canada with the support of the Canadian Space Agency. This research has made use of NASA’s Astrophysics Data System Bibliographic Services.

For the purpose of open access, the author has applied a Creative Commons Attribution (CC BY) licence to any Author Accepted Manuscript version arising from this submission.

DATA AVAILABILITY

All *JWST* and *HST* data products are available via the Mikulski Archive for Space Telescopes (<https://mast.stsci.edu>). Additional

data products are available from the authors upon reasonable request.

REFERENCES

Adscheid S., et al., 2024, *A&A*, 685, A1
 Algera H. S. B., et al., 2023, *MNRAS*, 518, 6142
 Arnouts S., Ilbert O., 2011, LePHARE: Photometric Analysis for Redshift Estimate, Astrophysics Source Code Library, record ascl:1108.009
 Bagley M. B., et al., 2023, *ApJ*, 946, L12
 Barrufet L., et al., 2023a, *MNRAS*, 522, 449
 Barrufet L., et al., 2023b, *MNRAS*, 522, 3926
 Begley R., et al., 2024, *arXiv e-prints*, p. arXiv:2410.10988
 Behroozi P. S., Wechsler R. H., Conroy C., 2013, *ApJ*, 770, 57
 Belli S., et al., 2021, The Stellar and Gas Content of Galaxies at Cosmic Noon, JWST Proposal. Cycle 1, ID. #1810
 Bourne N., Dunlop J. S., Simpson J. M., Rowlands K. E., Geach J. E., McLeod D. J., 2019, *MNRAS*, 482, 3135
 Bouwens R. J., et al., 2016, *ApJ*, 833, 72
 Bouwens R., et al., 2020, *ApJ*, 902, 112
 Bouwens R. J., et al., 2022, *ApJ*, 931, 160
 Bowler R. A. A., et al., 2014, *MNRAS*, 440, 2810
 Bowler R. A. A., et al., 2024, *MNRAS*, 527, 5808
 Brammer G., 2023, msaexp: NIRSpec analysis tools, doi:10.5281/zenodo.7299500
 Brammer G. B., van Dokkum P. G., Coppi P., 2008, *ApJ*, 686, 1503
 Brammer G. B., et al., 2012, *ApJS*, 200, 13
 Bruzual G., Charlot S., 2003, *MNRAS*, 344, 1000
 Carnall A. C., McLure R. J., Dunlop J. S., Davé R., 2018, *MNRAS*, 480, 4379
 Carnall A. C., et al., 2023, *MNRAS*, 520, 3974
 Carnall A. C., et al., 2024, *MNRAS*, 534, 325
 Casey C. M., et al., 2018a, *ApJ*, 862, 77
 Casey C. M., Hodge J., Zavala J. A., Spilker J., da Cunha E., Staguhn J., Finkelstein S. L., Drew P., 2018b, *ApJ*, 862, 78
 Casey C. M., et al., 2019, *ApJ*, 887, 55
 Casey C. M., et al., 2021, *ApJ*, 923, 215
 Casey C. M., et al., 2023, *ApJ*, 954, 31
 Cataldi G., et al., 2023, *ApJ*, 951, 111
 Chabrier G., 2003, *PASP*, 115, 763
 Champagne J. B., et al., 2021, *ApJ*, 913, 110
 Chen C.-C., et al., 2022, *ApJ*, 929, 159
 Circosta C., et al., 2021, *A&A*, 646, A96
 Cochrane R. K., et al., 2023, *MNRAS*, 523, 6082
 Coulter D., et al., 2024, The High-z Menagerie: A Rare Chance to Study the Early and Exotic Transient Universe, JWST Proposal. Cycle 2, ID. #6585
 Cullen F., et al., 2024, *MNRAS*, 531, 997
 Cullen F., et al., 2025, *arXiv e-prints*, p. arXiv:2501.11099
 Donnan C. T., et al., 2024, *MNRAS*, 533, 3222
 Donnan C. T., Dunlop J. S., McLure R. J., McLeod D. J., Cullen F., 2025, *arXiv e-prints*, p. arXiv:2501.03217
 Dudzevičiūtė U., et al., 2020, *MNRAS*, 494, 3828
 Dunlop J. S., 2016, *The Messenger*, 166, 48
 Dunlop J. S., et al., 2017, *MNRAS*, 466, 861
 Dunlop J. S., et al., 2021, PRIMER: Public Release IMaging for Extragalactic Research, JWST Proposal. Cycle 1, ID. #1837
 Ferrara A., Carniani S., di Mascia F., Bouwens R. J., Oesch P., Schouws S., 2025, *A&A*, 694, A215
 Fioc M., Rocca-Volmerange B., 1997, *A&A*, 326, 950
 Fioc M., Rocca-Volmerange B., 1999, *arXiv e-prints*, pp astro-ph/9912179
 Fioc M., Rocca-Volmerange B., 2019, *A&A*, 623, A143
 Fujimoto S., et al., 2020, *ApJ*, 900, 1
 Fujimoto S., et al., 2024, *ApJS*, 275, 36
 Furusawa H., et al., 2016, *ApJ*, 822, 46
 Gaia Collaboration et al., 2023, *A&A*, 674, A1
 Geach J. E., et al., 2017, *MNRAS*, 465, 1789
 Gillman S., et al., 2024, *A&A*, 691, A299

- Glazebrook K., et al., 2021, How Many Quiescent Galaxies are There at 3, JWST Proposal. Cycle 1, ID. #2565
- Grogin N. A., et al., 2011, *ApJS*, 197, 35
- Gruppioni C., et al., 2015, *MNRAS*, 451, 3419
- Gruppioni C., et al., 2020, *A&A*, 643, A8
- Hainline K. N., et al., 2024, *ApJ*, 964, 71
- Hasinger G., et al., 2018, *ApJ*, 858, 77
- Heintz K. E., et al., 2024, *Science*, 384, 890
- Hudelot P., et al., 2012, VizieR Online Data Catalog: The CFHTLS Survey (T0007 release) (Hudelot+ 2012), VizieR On-line Data Catalog: II/317. Originally published in: SPIE Conf. 2012
- Inami H., et al., 2022, *MNRAS*, 515, 3126
- Iverson R. J., et al., 2007, *MNRAS*, 380, 199
- Jin S., et al., 2024, *A&A*, 690, L16
- Kaasinen M., et al., 2019, *ApJ*, 880, 15
- Kennicutt Jr. R. C., 1998, *ARA&A*, 36, 189
- Khostovan A. A., et al., 2025, COSMOS Spectroscopic Redshift Compilation (First Data Release): 165k Redshifts Encompassing Two Decades of Spectroscopy (arXiv:2503.00120), <https://arxiv.org/abs/2503.00120>
- Khusanova Y., et al., 2021, *A&A*, 649, A152
- Koekemoer A. M., et al., 2011, *ApJS*, 197, 36
- Koprowski M. P., Dunlop J. S., Michałowski M. J., Coppin K. E. K., Geach J. E., McLure R. J., Scott D., van der Werf P. P., 2017, *MNRAS*, 471, 4155
- Kriek M., et al., 2015, *ApJS*, 218, 15
- Kron R. G., 1980, *ApJS*, 43, 305
- Larson R. L., et al., 2023, *ApJ*, 958, 141
- Lawrence A., et al., 2007, *MNRAS*, 379, 1599
- Le Fèvre O., et al., 2015, *A&A*, 576, A79
- Le Fèvre O., et al., 2020, *A&A*, 643, A1
- Liao C.-L., et al., 2024, *ApJ*, 961, 226
- Lilly S. J., et al., 2007, *ApJS*, 172, 70
- Lilly S. J., et al., 2009, *ApJS*, 184, 218
- Liu D., et al., 2018, *ApJ*, 853, 172
- Liu D., et al., 2019, *ApJS*, 244, 40
- Loiacono F., et al., 2021, *A&A*, 646, A76
- Long A. S., et al., 2024, arXiv e-prints, p. arXiv:2408.14546
- Madau P., Dickinson M., 2014, *ARA&A*, 52, 415
- Magnelli B., Elbaz D., Chary R. R., Dickinson M., Le Borgne D., Frayer D. T., Willmer C. N. A., 2011, *A&A*, 528, A35
- Magnelli B., et al., 2013, *A&A*, 553, A132
- Magnelli B., et al., 2024, *A&A*, 688, A55
- Masters D. C., Stern D. K., Cohen J. G., Capak P. L., Rhodes J. D., Castander F. J., Paltani S., 2017, *ApJ*, 841, 111
- Masters D. C., et al., 2019, *ApJ*, 877, 81
- McCracken H. J., et al., 2012, *A&A*, 544, A156
- McLeod D. J., McLure R. J., Dunlop J. S., Cullen F., Carnall A. C., Duncan K., 2021, *MNRAS*, 503, 4413
- McLeod D. J., et al., 2024, *MNRAS*, 527, 5004
- McLure R. J., et al., 2018, *MNRAS*, 476, 3991
- Merlin E., et al., 2015, *A&A*, 582, A15
- Michałowski M. J., et al., 2017, *MNRAS*, 469, 492
- Mitsuhashi I., et al., 2021, *ApJ*, 907, 122
- Momcheva I. G., Williams K. A., Cool R. J., Keeton C. R., Zabludoff A. I., 2015, *ApJS*, 219, 29
- Nanayakkara T., et al., 2016, *ApJ*, 828, 21
- Novak M., et al., 2017, *A&A*, 602, A5
- Oke J. B., 1974, *ApJS*, 27, 21
- Oke J. B., Gunn J. E., 1983, *ApJ*, 266, 713
- Östlin G., et al., 2024, arXiv e-prints, p. arXiv:2411.19686
- Pérez-González P. G., et al., 2023, *ApJ*, 946, L16
- Pérez-González P. G., et al., 2024, *ApJ*, 968, 4
- Planck Collaboration et al., 2020, *A&A*, 641, A6
- Rizzo F., et al., 2023, *A&A*, 679, A129
- Rowan-Robinson M., et al., 2016, *MNRAS*, 461, 1100
- Sanders R. L., et al., 2023, *ApJ*, 942, 24
- Schreiber C., et al., 2018a, *A&A*, 611, A22
- Schreiber C., et al., 2018b, *A&A*, 618, A85
- Scoville N., et al., 2007, *ApJS*, 172, 1
- Silverman J. D., et al., 2015, *ApJS*, 220, 12
- Simpson J. M., et al., 2019, *ApJ*, 880, 43
- Simpson J. M., et al., 2020, *MNRAS*, 495, 3409
- Smit R., et al., 2018, *Nature*, 553, 178
- Speagle J. S., Steinhardt C. L., Capak P. L., Silverman J. D., 2014, *ApJS*, 214, 15
- Sun F., et al., 2025, *ApJ*, 980, 12
- Tasca L. A. M., et al., 2017, *A&A*, 600, A110
- Traina A., et al., 2024, *A&A*, 690, A84
- Valentino F., et al., 2018, *ApJ*, 869, 27
- Valentino F., et al., 2020, *ApJ*, 890, 24
- Wang L., Pearson W. J., Cowley W., Trayford J. W., Béthermin M., Gruppioni C., Hurley P., Michałowski M. J., 2019, *A&A*, 624, A98
- Williams C. C., et al., 2019, *ApJ*, 884, 154
- Xiao M. Y., et al., 2023, *A&A*, 672, A18
- Zavala J. A., Casey C. M., da Cunha E., Spilker J., Staguhn J., Hodge J., Drew P. M., 2018, *ApJ*, 869, 71
- Zavala J. A., et al., 2019, *ApJ*, 887, 183
- Zavala J. A., et al., 2021, *ApJ*, 909, 165
- de Graaff A., et al., 2024, arXiv e-prints, p. arXiv:2409.05948
- van der Vlugt D., Hodge J. A., Algera H. S. B., Smail I., Leslie S. K., Radcliffe J. F., Riechers D. A., Röttgering H., 2022, *ApJ*, 941, 10
- van der Wel A., et al., 2021, *ApJS*, 256, 44

APPENDIX A: SOURCE CATALOGUES

Here we present the final sample of 128 *JWST*-detected ALMA sources in the PRIMER COSMOS footprint. Basic observational properties such as positions and flux densities are tabulated in Table A1, while the redshifts (spectroscopic and photometric) and derived physical properties of the galaxies are given in Table A2.

Table A1. The complete catalogue of ALMA sources within the PRIMER COSMOS footprint. Only the highest-S/N ALMA detection for each source is listed here. For the JWST PRIMER detections, we list two representative fluxes from NIRCam (F444W) and MIRI (F770W), respectively, while the coordinates are based on F356W imaging. The f_{F770W} has a typical uncertainty of 10%. The flag indicates if the source is also detected by AS2COSMOS ('S', Simpson et al. 2020) or Ex-MORA ('E', Long et al. 2024) or both. † ALMA properties of ID 024 are taken from Ex-MORA (Long et al. 2024).

| ID | ALMA | | | | JWST NIRCam & MIRI | | | | UltraVISTA | | | Flag |
|------|---------------|---------------|------------------|-------------------------|--------------------|---------------|----------------------------|----------------------------|---------------|---------------|-------------------------|------|
| | R.A. (deg) | Dec. (deg) | S_ν (mJy) | λ (μ m) | R.A. (deg) | Dec. (deg) | S_{F444W} (μ Jy) | S_{F770W} (μ Jy) | R.A. (deg) | Dec. (deg) | S_{Ks} (μ Jy) | |
| 001 | 150.06505 | 2.26361 | 5.13 (0.10) | 1287 | 150.06509 | 2.26363 | 0.55 (0.03) | 2.94 | 150.06519 | 2.26365 | 0.55 (0.07) | E, S |
| 002 | 150.09991 | 2.29722 | 10.45 (0.60) | 873 | 150.10004 | 2.29739 | 1.67 (0.08) | 4.46 | 150.10011 | 2.29714 | 66.65 (3.33) | S |
| 003 | 150.13264 | 2.21187 | 2.82 (0.10) | 1287 | 150.13265 | 2.21184 | 12.15 (0.61) | 18.80 | 150.13266 | 2.21193 | 5.84 (0.29) | S |
| 004 | 150.09856 | 2.36537 | 8.63 (0.39) | 873 | 150.09855 | 2.36537 | 7.22 (0.36) | - | 150.09857 | 2.36536 | 2.46 (0.12) | S |
| 005 | 150.10541 | 2.31282 | 8.15 (0.37) | 873 | 150.10539 | 2.31283 | 6.35 (0.32) | 10.92 | 150.10543 | 2.31284 | 2.66 (0.13) | E, S |
| 006 | 150.20803 | 2.38314 | 8.01 (0.37) | 873 | - | - | - | 8.66 | 150.20803 | 2.38310 | 1.09 (0.05) | S |
| 007 | 150.16352 | 2.37252 | 7.20 (0.36) | 873 | 150.16352 | 2.37248 | 6.93 (0.35) | 15.02 | 150.16357 | 2.37246 | 5.95 (0.30) | S |
| 008 | 150.04823 | 2.25145 | 6.90 (0.38) | 873 | - | - | - | 11.08 | 150.04826 | 2.25148 | 1.99 (0.10) | E, S |
| 009 | 150.10063 | 2.33483 | 6.76 (0.32) | 873 | 150.10063 | 2.33483 | 0.31 (0.02) | 1.46 | - | - | - | E, S |
| 010 | 150.13894 | 2.43376 | 2.17 (0.09) | 1249 | 150.13896 | 2.43377 | 7.40 (0.37) | 13.37 | 150.13900 | 2.43376 | 2.22 (0.11) | E, S |
| 011 | 150.10394 | 2.18642 | 6.15 (0.31) | 873 | 150.10393 | 2.18642 | 15.13 (0.76) | 15.54 | 150.10396 | 2.18642 | 5.13 (0.26) | S |
| 012 | 150.05243 | 2.24559 | 5.77 (0.28) | 873 | - | - | - | 15.88 | 150.05247 | 2.24554 | 9.72 (0.49) | S |
| 013 | 150.14320 | 2.35603 | 5.72 (0.41) | 870 | 150.14323 | 2.35602 | 2.06 (0.10) | 5.01 | 150.14313 | 2.35591 | 1.22 (0.07) | S |
| 014 | 150.14728 | 2.47409 | 3.31 (0.17) | 1035 | 150.14725 | 2.47407 | 0.81 (0.04) | 2.87 | - | - | - | S |
| 015 | 150.03142 | 2.19637 | 1.85 (0.09) | 1249 | - | - | - | 6.27 | 150.03147 | 2.19644 | 1.69 (0.08) | S |
| 016 | 150.10445 | 2.43537 | 5.23 (0.46) | 873 | 150.10445 | 2.43540 | 0.12 (0.01) | 0.86 | - | - | - | S |
| 017 | 150.12926 | 2.46431 | 5.16 (0.41) | 873 | 150.12928 | 2.46431 | 3.22 (0.16) | - | 150.12931 | 2.46431 | 0.76 (0.06) | S |
| 018 | 150.15026 | 2.36414 | 0.12 (0.04) | 3010 | 150.15024 | 2.36413 | 7.16 (0.36) | 11.77 | 150.15023 | 2.36412 | 3.87 (0.19) | S |
| 019 | 150.15373 | 2.32798 | 1.90 (0.12) | 1200 | 150.15374 | 2.32798 | 4.67 (0.23) | 2.33 | 150.15377 | 2.32797 | 1.00 (0.05) | S |
| 020 | 150.09852 | 2.32085 | 4.83 (0.39) | 873 | 150.09853 | 2.32087 | 2.67 (0.13) | 6.53 | 150.09863 | 2.32082 | 1.12 (0.06) | S |
| 021 | 150.08063 | 2.39027 | 0.11 (0.02) | 3088 | 150.08061 | 2.39027 | 66.30 (3.31) | - | 150.08065 | 2.39026 | 222.43 (9.12) | S |
| 022 | 150.17326 | 2.46435 | 4.36 (0.35) | 873 | 150.17324 | 2.46432 | 12.71 (0.64) | 16.77 | 150.17327 | 2.46431 | 7.91 (0.40) | S |
| 023 | 150.07593 | 2.21182 | 1.36 (0.11) | 1287 | 150.07594 | 2.21180 | 10.99 (0.55) | 11.42 | 150.07598 | 2.21176 | 8.88 (0.44) | S |
| 024† | 150.04096 | 2.28048 | 0.33 (0.06) | 2040 | - | - | - | 6.27 | 150.04104 | 2.28044 | 0.52 (0.05) | E |
| 025 | 150.10981 | 2.25775 | 3.90 (0.12) | 889 | 150.10982 | 2.25776 | 0.09 (0.01) | 0.41 | - | - | - | E |
| 026 | 150.10588 | 2.42880 | 4.09 (0.25) | 873 | 150.10587 | 2.42881 | 2.49 (0.12) | 6.12 | - | - | - | S |
| 027 | 150.10631 | 2.25158 | 3.68 (0.47) | 873 | 150.10631 | 2.25157 | 11.36 (0.57) | 10.59 | 150.10642 | 2.25159 | 3.88 (0.19) | S |
| 028 | 150.03650 | 2.19838 | 1.23 (0.08) | 1249 | - | - | - | 8.75 | 150.03657 | 2.19837 | 1.89 (0.09) | S |
| 029 | 150.03738 | 2.34073 | 2.32 (0.12) | 1009 | - | - | - | 4.63 | 150.03729 | 2.34060 | 1.79 (0.09) | E |
| 030 | 150.17488 | 2.35278 | 3.62 (0.34) | 870 | 150.17487 | 2.35274 | 1.54 (0.08) | 4.07 | 150.17490 | 2.35269 | 0.52 (0.04) | S |
| 031 | 150.10572 | 2.43481 | 3.57 (0.43) | 873 | 150.10574 | 2.43483 | 0.38 (0.02) | 1.32 | - | - | - | S |
| 032 | 150.17184 | 2.24070 | 1.07 (0.07) | 1287 | 150.17185 | 2.24071 | 11.14 (0.56) | - | 150.17186 | 2.24067 | 3.54 (0.18) | S |
| 033 | 150.17425 | 2.42973 | 3.26 (0.29) | 870 | 150.17428 | 2.42973 | 0.67 (0.03) | 2.78 | 150.17432 | 2.42975 | 0.17 (0.04) | S |
| 034 | 150.07192 | 2.19020 | 3.22 (0.53) | 873 | 150.07194 | 2.19017 | 4.40 (0.22) | 8.84 | 150.07198 | 2.19017 | 1.66 (0.08) | S |
| 035 | 150.13655 | 2.23243 | 0.99 (0.13) | 1287 | 150.13653 | 2.23242 | 3.59 (0.18) | 8.23 | - | - | - | S |
| 036 | 150.13914 | 2.43197 | 1.05 (0.10) | 1249 | 150.13916 | 2.43198 | 4.43 (0.22) | 8.13 | 150.13922 | 2.43198 | 1.42 (0.07) | S |
| 037 | 150.03954 | 2.37208 | 3.04 (0.52) | 873 | - | - | - | 11.72 | 150.03960 | 2.37205 | 6.27 (0.31) | S |
| 038 | 150.11126 | 2.40319 | 3.04 (0.59) | 873 | 150.11129 | 2.40318 | 5.65 (0.28) | - | 150.11132 | 2.40320 | 1.50 (0.08) | S |
| 039 | 150.03719 | 2.24460 | 0.94 (0.20) | 1287 | - | - | - | 54.91 | 150.03722 | 2.24463 | 73.06 (3.65) | S |
| 040 | 150.13639 | 2.22533 | 0.91 (0.09) | 1287 | 150.13638 | 2.22531 | 8.41 (0.42) | 11.80 | 150.13641 | 2.22530 | 4.91 (0.25) | S |
| 041 | 150.03641 | 2.31719 | 0.79 (0.06) | 1333 | - | - | - | 10.04 | 150.03651 | 2.31718 | 20.84 (1.04) | S |
| 042 | 150.14415 | 2.37632 | 2.36 (0.43) | 873 | 150.14417 | 2.37632 | 2.18 (0.11) | 4.39 | 150.14421 | 2.37633 | 0.60 (0.05) | S |
| 043 | 150.05312 | 2.19807 | 2.80 (0.58) | 873 | - | - | - | 15.38 | 150.05322 | 2.19809 | 22.36 (1.12) | S |
| 044 | 150.14283 | 2.41751 | 2.62 (0.44) | 873 | 150.14285 | 2.41747 | 1.91 (0.10) | 4.10 | 150.14289 | 2.41745 | 0.79 (0.05) | S |
| 045 | 150.03652 | 2.32122 | 0.72 (0.06) | 1333 | - | - | - | 27.45 | 150.03654 | 2.32125 | 1.01 (0.05) | S |
| 046 | 150.12059 | 2.41810 | 2.55 (0.28) | 873 | 150.12058 | 2.41809 | 1.47 (0.07) | 4.13 | 150.12063 | 2.41811 | 0.33 (0.04) | S |
| 047 | 150.09940 | 2.40492 | 0.77 (0.13) | 1287 | 150.0994 | 2.40492 | 3.58 (0.18) | - | 150.09945 | 2.40490 | 1.31 (0.07) | S |
| 048 | 150.21011 | 2.31165 | 1.44 (0.08) | 1042 | - | - | - | 37.58 | 150.21019 | 2.31167 | 52.54 (2.63) | S |
| 049 | 150.11211 | 2.31401 | 1.08 (0.21) | 1131 | 150.11213 | 2.31400 | 4.81 (0.24) | - | 150.11219 | 2.31399 | 2.70 (0.14) | S |
| 050 | 150.14174 | 2.42569 | 0.91 (0.05) | 1195 | 150.14176 | 2.42568 | 3.90 (0.20) | 7.78 | 150.14181 | 2.42574 | 1.01 (0.05) | S |
| 051 | 150.07469 | 2.21648 | 0.71 (0.04) | 1287 | 150.07469 | 2.21648 | 5.28 (0.26) | 6.01 | 150.07473 | 2.21650 | 2.00 (0.10) | S |
| 052 | 150.09458 | 2.33633 | 0.84 (0.08) | 1215 | 150.09459 | 2.33635 | 17.28 (0.86) | 11.73 | 150.09463 | 2.33635 | 29.09 (1.45) | S |
| 053 | 150.18759 | 2.32248 | 2.21 (0.25) | 873 | 150.18759 | 2.32249 | 22.64 (1.13) | 17.19 | 150.18764 | 2.32249 | 16.51 (0.83) | S |
| 054 | 150.16768 | 2.29873 | 0.81 (0.23) | 1209 | 150.16767 | 2.29875 | 10.21 (0.51) | - | 150.16771 | 2.29875 | 3.81 (0.19) | S |
| 055 | 150.10355 | 2.34608 | 0.66 (0.05) | 1279 | 150.10351 | 2.34608 | 9.98 (0.50) | 10.40 | 150.10353 | 2.34611 | 23.27 (1.16) | S |
| 056 | 150.15365 | 2.24773 | 0.71 (0.12) | 1249 | 150.15365 | 2.24777 | 1.84 (0.09) | - | 150.15366 | 2.24773 | 0.55 (0.05) | S |
| 057 | 150.09824 | 2.16625 | 0.62 (0.07) | 1287 | - | - | - | 7.01 | 150.09826 | 2.16623 | 0.58 (0.05) | S |
| 058 | 150.18712 | 2.38012 | 0.13 (0.02) | 2160 | 150.18715 | 2.38014 | 9.73 (0.49) | 13.29 | 150.18720 | 2.38014 | 4.65 (0.23) | S |
| 059 | 150.09251 | 2.39816 | 0.60 (0.08) | 1287 | 150.09251 | 2.39816 | 0.69 (0.03) | - | - | - | - | S |
| 060 | 150.22026 | 2.31933 | 0.04 (0.01) | 3187 | - | - | - | 4.62 | 150.22035 | 2.31925 | 2.70 (0.13) | S |

Table A1 – *continued*

| ID | ALMA | | | | JWST NIRCam & MIRI | | | | UltraVISTA | | | Flag |
|-----|---------------|---------------|------------------|--------------------------------|--------------------|---------------|-----------------------------------|-----------------------------------|---------------|---------------|--------------------------------|------|
| | R.A. (deg) | Dec. (deg) | f_ν (mJy) | λ (μm) | R.A. (deg) | Dec. (deg) | f_{F444W} (μJy) | f_{F770W} (μJy) | R.A. (deg) | Dec. (deg) | f_{Ks} (μJy) | |
| 061 | 150.12996 | 2.25271 | 1.92 (0.43) | 873 | 150.12997 | 2.25268 | 5.84 (0.29) | - | 150.13001 | 2.25268 | 1.59 (0.08) | S |
| 062 | 150.09596 | 2.36527 | 1.90 (0.26) | 870 | 150.09596 | 2.36526 | 1.39 (0.07) | - | 150.09599 | 2.36525 | 0.25 (0.05) | |
| 063 | 150.12913 | 2.28456 | 1.14 (0.17) | 1031 | 150.12914 | 2.28456 | 0.71 (0.04) | 2.04 | 150.12918 | 2.28458 | 0.32 (0.06) | |
| 064 | 150.06143 | 2.3788 | 1.29 (0.03) | 989 | 150.06145 | 2.37871 | 5.05 (0.25) | - | 150.06149 | 2.37872 | 2.63 (0.13) | |
| 065 | 150.10520 | 2.32581 | 0.69 (0.11) | 1213 | 150.10520 | 2.32582 | 3.46 (0.17) | 5.32 | 150.10528 | 2.32589 | 1.46 (0.07) | |
| 066 | 150.18425 | 2.25212 | 0.55 (0.12) | 1287 | 150.18423 | 2.25210 | 0.51 (0.03) | - | - | - | - | |
| 067 | 150.10520 | 2.15661 | 0.55 (0.11) | 1249 | - | - | - | 5.91 | 150.10522 | 2.15664 | 2.24 (0.11) | |
| 068 | 150.09808 | 2.16577 | 0.48 (0.09) | 1287 | - | - | - | 24.92 | 150.09813 | 2.16581 | 20.62 (1.03) | |
| 069 | 150.11574 | 2.43112 | 1.52 (0.23) | 873 | 150.11575 | 2.43112 | 0.52 (0.03) | 1.58 | 150.11570 | 2.43110 | 0.12 (0.06) | |
| 070 | 150.06451 | 2.32914 | 1.51 (0.23) | 873 | 150.06446 | 2.32916 | 6.17 (0.31) | 8.84 | 150.06456 | 2.32904 | 14.11 (0.71) | |
| 071 | 150.12287 | 2.36095 | 1.51 (0.28) | 873 | 150.12289 | 2.36096 | 4.90 (0.25) | 6.98 | 150.12294 | 2.36097 | 2.72 (0.14) | |
| 072 | 150.07740 | 2.18536 | 1.48 (0.36) | 873 | 150.07740 | 2.18536 | 4.30 (0.22) | 4.88 | 150.07745 | 2.18537 | 1.47 (0.07) | |
| 073 | 150.04297 | 2.34090 | 0.57 (0.05) | 1193 | - | - | - | 12.18 | 150.04304 | 2.34091 | 21.46 (1.07) | |
| 074 | 150.09885 | 2.16626 | 0.45 (0.09) | 1287 | - | - | - | 20.42 | 150.09887 | 2.16623 | 14.09 (0.70) | |
| 075 | 150.14299 | 2.35590 | 1.44 (0.38) | 873 | 150.14300 | 2.35589 | 2.39 (0.12) | 5.87 | 150.14313 | 2.35591 | 1.22 (0.07) | |
| 076 | 150.11256 | 2.37658 | 1.45 (0.34) | 870 | 150.11252 | 2.37654 | 3.15 (0.16) | - | 150.11256 | 2.37653 | 0.84 (0.05) | |
| 077 | 150.13085 | 2.20895 | 0.48 (0.11) | 1249 | 150.13087 | 2.20894 | 3.29 (0.16) | 5.51 | 150.13088 | 2.20903 | 1.31 (0.07) | |
| 078 | 150.07716 | 2.38036 | 0.44 (0.03) | 1287 | 150.07716 | 2.38037 | 3.87 (0.19) | - | 150.07717 | 2.38040 | 2.12 (0.11) | |
| 079 | 150.03003 | 2.31411 | 0.40 (0.08) | 1326 | - | - | - | 10.15 | 150.03003 | 2.31415 | 3.75 (0.19) | |
| 080 | 150.10981 | 2.25740 | 1.31 (0.09) | 889 | 150.10979 | 2.25739 | 0.10 (0.01) | 0.24 | - | - | - | |
| 081 | 150.15865 | 2.46835 | 1.38 (0.22) | 873 | 150.15858 | 2.46835 | 0.82 (0.04) | 0.06 | 150.15862 | 2.46833 | 0.40 (0.05) | |
| 082 | 150.16687 | 2.23582 | 0.40 (0.09) | 1287 | 150.16687 | 2.23582 | 12.98 (0.65) | - | 150.16691 | 2.23580 | 5.36 (0.27) | |
| 083 | 150.10698 | 2.42895 | 1.30 (0.31) | 873 | 150.10697 | 2.42894 | 2.07 (0.10) | 3.63 | 150.10701 | 2.42912 | 10.31 (0.52) | |
| 084 | 150.05911 | 2.21987 | 0.35 (0.08) | 1344 | 150.05922 | 2.21979 | 17.05 (0.85) | 14.30 | 150.05915 | 2.21994 | 27.93 (1.40) | |
| 085 | 150.09400 | 2.24583 | 0.40 (0.12) | 1287 | 150.09401 | 2.24585 | 6.93 (0.35) | 6.45 | 150.09406 | 2.24588 | 3.46 (0.17) | |
| 086 | 150.07066 | 2.30517 | 0.43 (0.10) | 1249 | 150.07066 | 2.30512 | 1.70 (0.09) | 3.84 | 150.07065 | 2.30518 | 1.58 (0.08) | |
| 087 | 150.15175 | 2.33459 | 0.37 (0.03) | 1310 | 150.15178 | 2.33459 | 22.33 (1.12) | 15.11 | 150.15184 | 2.33459 | 16.05 (0.80) | |
| 088 | 150.11262 | 2.40668 | 1.25 (0.23) | 873 | 150.11260 | 2.40668 | 1.03 (0.05) | - | - | - | - | |
| 089 | 150.08802 | 2.39511 | 1.24 (0.15) | 873 | 150.08801 | 2.39510 | 2.49 (0.12) | - | 150.08804 | 2.39509 | 1.28 (0.08) | |
| 090 | 150.13653 | 2.26058 | 1.33 (0.23) | 847 | 150.13650 | 2.26058 | 2.36 (0.12) | 2.94 | 150.13653 | 2.26055 | 0.28 (0.04) | |
| 091 | 150.10283 | 2.38454 | 1.22 (0.29) | 870 | 150.10283 | 2.38451 | 3.39 (0.17) | - | 150.10287 | 2.38452 | 0.64 (0.05) | |
| 092 | 150.15025 | 2.47514 | 1.19 (0.26) | 873 | 150.15022 | 2.47515 | - | 368.11 | 150.15027 | 2.47515 | 87.40 (4.37) | |
| 093 | 150.12637 | 2.43288 | 1.24 (0.10) | 857 | 150.12635 | 2.43287 | 15.48 (0.77) | 12.64 | 150.12639 | 2.43287 | 13.08 (0.65) | |
| 094 | 150.07725 | 2.21141 | 0.46 (0.06) | 1187 | 150.07724 | 2.21141 | 5.18 (0.26) | 5.23 | 150.07725 | 2.21141 | 1.85 (0.09) | |
| 095 | 150.14722 | 2.33718 | 1.12 (0.31) | 885 | 150.14718 | 2.33718 | 25.94 (1.30) | 20.27 | 150.14722 | 2.33717 | 60.72 (3.04) | |
| 096 | 150.17078 | 2.36860 | 1.14 (0.33) | 870 | 150.17079 | 2.36862 | 1.85 (0.09) | 3.41 | 150.17079 | 2.36857 | 0.55 (0.04) | |
| 097 | 150.03737 | 2.27182 | 1.10 (0.24) | 873 | - | - | - | 9.05 | 150.03745 | 2.27185 | 6.47 (0.32) | |
| 098 | 150.14479 | 2.21969 | 1.09 (0.33) | 873 | 150.14481 | 2.21971 | 7.25 (0.36) | 5.47 | 150.14476 | 2.21972 | 3.74 (0.19) | |
| 099 | 150.19617 | 2.48181 | 0.38 (0.08) | 1241 | - | - | - | 9.56 | 150.19624 | 2.48179 | 4.93 (0.25) | |
| 100 | 150.07933 | 2.34058 | 1.05 (0.29) | 873 | 150.07932 | 2.34056 | 6.60 (0.33) | 7.35 | 150.07938 | 2.34057 | 3.84 (0.19) | |
| 101 | 150.11431 | 2.36983 | 0.32 (0.09) | 1287 | 150.11431 | 2.36985 | 1.31 (0.07) | - | 150.11439 | 2.36989 | 0.82 (0.05) | |
| 102 | 150.09545 | 2.24667 | 0.99 (0.28) | 873 | 150.09546 | 2.24667 | 6.05 (0.30) | 8.08 | 150.09551 | 2.24668 | 1.52 (0.08) | |
| 103 | 150.15710 | 2.33230 | 0.37 (0.06) | 1200 | 150.15711 | 2.33231 | 0.84 (0.04) | 1.51 | - | - | - | |
| 104 | 150.11237 | 2.37526 | 0.29 (0.05) | 1287 | 150.11235 | 2.37524 | 2.51 (0.13) | - | 150.11240 | 2.37522 | 2.14 (0.11) | |
| 105 | 150.11510 | 2.32127 | 0.28 (0.05) | 1287 | 150.11510 | 2.32127 | 4.51 (0.23) | 3.05 | 150.11514 | 2.32128 | 1.37 (0.07) | |
| 106 | 150.10750 | 2.34435 | 0.28 (0.07) | 1279 | 150.10753 | 2.34433 | 2.20 (0.11) | - | 150.10758 | 2.34430 | 0.89 (0.06) | |
| 107 | 150.03846 | 2.33944 | 0.56 (0.06) | 1009 | - | - | - | 3.41 | 150.03848 | 2.33947 | 0.64 (0.05) | |
| 108 | 150.06669 | 2.25772 | 0.26 (0.08) | 1287 | 150.06669 | 2.25772 | 3.07 (0.15) | 4.12 | 150.06674 | 2.25772 | 1.70 (0.08) | |
| 109 | 150.09532 | 2.33895 | 0.31 (0.07) | 1215 | 150.09532 | 2.33897 | 2.14 (0.11) | 3.66 | 150.09537 | 2.33898 | 1.36 (0.07) | |
| 110 | 150.10875 | 2.20871 | 0.79 (0.20) | 873 | 150.10874 | 2.20870 | 0.93 (0.05) | 2.25 | 150.10875 | 2.20873 | 0.21 (0.05) | |
| 111 | 150.08425 | 2.21847 | 0.26 (0.08) | 1213 | 150.08432 | 2.21848 | 1.19 (0.06) | 2.25 | 150.08433 | 2.21854 | 1.64 (0.08) | |
| 112 | 150.07528 | 2.37943 | 0.21 (0.03) | 1287 | 150.07524 | 2.37941 | 5.61 (0.28) | - | 150.07527 | 2.37941 | 4.91 (0.25) | |
| 113 | 150.14127 | 2.27816 | 0.21 (0.05) | 1287 | 150.14127 | 2.27819 | 6.22 (0.31) | 10.74 | 150.14130 | 2.27818 | 2.04 (0.10) | |
| 114 | 150.04203 | 2.33898 | 0.26 (0.05) | 1193 | - | - | - | 2.91 | 150.04209 | 2.33900 | 1.40 (0.07) | |
| 115 | 150.10282 | 2.37940 | 0.19 (0.04) | 1287 | 150.10284 | 2.37940 | 4.24 (0.21) | - | 150.10289 | 2.37942 | 1.03 (0.05) | |
| 116 | 150.07574 | 2.38072 | 0.18 (0.04) | 1287 | 150.07584 | 2.38073 | 3.08 (0.15) | - | 150.07585 | 2.38067 | 3.56 (0.18) | |
| 117 | 150.14728 | 2.28236 | 0.18 (0.04) | 1287 | 150.14727 | 2.28232 | 7.41 (0.37) | 7.30 | 150.14732 | 2.28229 | 3.03 (0.15) | |
| 118 | 150.03921 | 2.33710 | 0.36 (0.07) | 1014 | - | - | - | 0.70 | 150.03932 | 2.33720 | 0.42 (0.04) | |
| 119 | 150.19437 | 2.27329 | 0.17 (0.05) | 1287 | 150.19435 | 2.27331 | 5.06 (0.25) | 6.26 | 150.19438 | 2.27334 | 3.36 (0.17) | |
| 120 | 150.19728 | 2.48045 | 0.18 (0.04) | 1241 | - | - | - | 0.41 | 150.19735 | 2.48043 | 0.18 (0.04) | |
| 121 | 150.12358 | 2.22071 | 0.17 (0.03) | 1203 | 150.12357 | 2.22070 | 0.95 (0.05) | 1.70 | 150.12362 | 2.22072 | 0.26 (0.04) | |
| 122 | 150.18430 | 2.26436 | 0.45 (0.07) | 873 | 150.18428 | 2.26437 | 3.27 (0.16) | 3.08 | 150.18431 | 2.26436 | 1.90 (0.09) | |
| 123 | 150.06978 | 2.38156 | 0.20 (0.06) | 1131 | 150.06982 | 2.38151 | 1.62 (0.08) | - | 150.06985 | 2.38155 | 1.01 (0.06) | |

Table A1 – *continued*

| ID | ALMA | | | | JWST NIRCam & MIRI | | | | UltraVISTA | | | Flag |
|-----|---------------|---------------|--------------------|--------------------------------|--------------------|---------------|-----------------------------------|-----------------------------------|---------------|---------------|--------------------------------|------|
| | R.A. (deg) | Dec. (deg) | f_{ν} (mJy) | λ (μm) | R.A. (deg) | Dec. (deg) | f_{F444W} (μJy) | f_{F770W} (μJy) | R.A. (deg) | Dec. (deg) | f_{Ks} (μJy) | |
| 124 | 150.13584 | 2.25791 | 0.33 (0.08) | 847 | 150.13582 | 2.25789 | 0.53 (0.03) | 0.66 | 150.13587 | 2.25789 | 0.50 (0.04) | |
| 125 | 150.17157 | 2.28730 | 0.30 (0.06) | 866 | 150.17157 | 2.28729 | 0.24 (0.01) | 0.27 | 150.17149 | 2.28731 | 0.49 (0.05) | |
| 126 | 150.12578 | 2.26662 | 0.08 (0.01) | 1284 | 150.12574 | 2.26660 | 0.41 (0.02) | - | 150.12577 | 2.26656 | 0.27 (0.04) | |
| 127 | 150.12487 | 2.26946 | 0.06 (0.01) | 1284 | 150.12487 | 2.26947 | 5.59 (0.28) | - | 150.12492 | 2.26947 | 5.41 (0.27) | |
| 128 | 150.03687 | 2.25772 | 0.16 (0.03) | 873 | - | - | - | 10.42 | 150.03690 | 2.25781 | 2.53 (0.13) | |

Table A2. The derived physical properties of the 128 sources in our sample. References for the best quality redshifts ('Ref.') are provided for the spectroscopic redshifts, which are rounded to three decimal places. For those from DJA, we refer to the observation programmes. The photometric redshifts are rounded to two decimal places, and flagged as 'J' or 'U' depending on whether they are derived from the *JWST* PRIMER or UltraVISTA data respectively. In the final column ('Flag'), we also use the 'J' and 'U' flags to indicate the origin of the photometry used to derive the physical properties of each galaxy. †The M_* and A_V of the lensed galaxy ID 002 are taken from [Jin et al. \(2024\)](#). All its properties are corrected for lensing with the magnification factor provided there.

| ID | z | Ref. | $f_{870\mu\text{m}}$ (mJy) | SFR_{FIR} ($M_{\odot}\text{yr}^{-1}$) | SFR_{UV} ($M_{\odot}\text{yr}^{-1}$) | SFR_{raw} ($M_{\odot}\text{yr}^{-1}$) | SFR_{corr} ($M_{\odot}\text{yr}^{-1}$) | M_* ($\log M_{\odot}$) | A_V | Flag |
|------|-------|---|-------------------------------|--|---|--|---|-------------------------------|------------------------|------|
| 001 | 4.596 | Chen et al. (2022) | 16.58 ± 0.32 | 1490 ± 28 | 0.90 | 1491 ± 28 | 1762^{+1557}_{-694} | $10.82^{+0.07}_{-0.07}$ | $2.88^{+0.29}_{-0.26}$ | J |
| 002† | 2.625 | Jin et al. (2024) | 10.54 ± 0.61 | 263^{+147}_{-68} | 0.38 | 264^{+147}_{-68} | 9^{+4}_{-5} | $10.84^{+0.19}_{-0.14}$ | 1.95 ± 0.01 | J |
| 003 | 2.104 | Kaasinen et al. (2019) | 9.13 ± 0.32 | 821 ± 29 | 0.21 | 821 ± 29 | 271^{+51}_{-51} | $11.69^{+0.06}_{-0.08}$ | $3.42^{+0.23}_{-0.43}$ | J |
| 004 | 2.364 | Brammer et al. (2012); Momcheva et al. (2015) | 8.71 ± 0.40 | 783 ± 35 | 0.15 | 783 ± 35 | 176^{+38}_{-28} | $11.51^{+0.07}_{-0.06}$ | $3.03^{+0.31}_{-0.19}$ | J |
| 005 | 2.283 | Khostovan et al. (2025) | 8.22 ± 0.38 | 739 ± 33 | 0.29 | 739 ± 33 | 324^{+244}_{-152} | $11.34^{+0.11}_{-0.19}$ | $2.71^{+0.26}_{-0.36}$ | J |
| 006 | 2.59 | U | 8.08 ± 0.37 | 726 ± 33 | 0.39 | 727 ± 33 | 55^{+12}_{-12} | $10.95^{+0.06}_{-0.06}$ | $1.88^{+0.16}_{-0.24}$ | U |
| 007 | 2.086 | Brammer et al. (2012); Momcheva et al. (2015) | 7.27 ± 0.36 | 653 ± 32 | 4.12 | 657 ± 32 | 417^{+28}_{-29} | $10.95^{+0.02}_{-0.01}$ | $2.06^{+0.04}_{-0.03}$ | J |
| 008 | 2.32 | U | 6.96 ± 0.39 | 625 ± 34 | 0.07 | 625 ± 34 | 107^{+25}_{-26} | $11.32^{+0.07}_{-0.06}$ | $2.68^{+0.30}_{-0.31}$ | U |
| 009 | 4.27 | J | 6.82 ± 0.32 | 613 ± 29 | 0.03 | 613 ± 29 | 73^{+20}_{-18} | $10.86^{+0.10}_{-0.08}$ | $3.25^{+0.28}_{-0.29}$ | J |
| 010 | 2.510 | Zavala et al. (2019) | 6.41 ± 0.25 | 576 ± 22 | 0.25 | 576 ± 22 | 145^{+52}_{-28} | $11.34^{+0.09}_{-0.09}$ | $3.22^{+0.31}_{-0.23}$ | J |
| 011 | 1.914 | Brammer et al. (2012); Momcheva et al. (2015) | 6.20 ± 0.31 | 557 ± 28 | 0.06 | 557 ± 28 | 118^{+21}_{-30} | $11.45^{+0.05}_{-0.05}$ | $3.03^{+0.19}_{-0.28}$ | J |
| 012 | 2.438 | Khostovan et al. (2025) | 5.82 ± 0.28 | 523 ± 25 | 1.31 | 525 ± 25 | 513^{+219}_{-167} | $11.39^{+0.08}_{-0.08}$ | $1.55^{+0.22}_{-0.26}$ | U |
| 013 | 2.988 | Zavala et al. (2019) | 5.71 ± 0.41 | 513 ± 36 | 0.12 | 513 ± 36 | 80^{+22}_{-14} | $11.02^{+0.07}_{-0.08}$ | $2.79^{+0.21}_{-0.21}$ | J |
| 014 | 5.62 | J | 5.57 ± 0.29 | 500 ± 26 | 0.48 | 500 ± 26 | 967^{+258}_{-230} | $10.80^{+0.16}_{-0.11}$ | $2.60^{+0.19}_{-0.17}$ | J |
| 015 | 3.40 | U | 5.48 ± 0.28 | 492 ± 24 | 2.86 | 495 ± 24 | 216^{+56}_{-57} | $10.69^{+0.08}_{-0.07}$ | $1.08^{+0.14}_{-0.19}$ | U |
| 016 | 4.615 | Mitsubishi et al. (2021) | 5.28 ± 0.46 | 474 ± 41 | 0.00 | 474 ± 41 | 35^{+20}_{-35} | $10.63^{+0.13}_{-0.12}$ | $4.13^{+0.49}_{-0.41}$ | J |
| 017 | 3.62 | J | 5.21 ± 0.42 | 468 ± 37 | 0.64 | 469 ± 37 | 170^{+35}_{-37} | $11.32^{+0.06}_{-0.06}$ | $2.14^{+0.22}_{-0.17}$ | J |
| 018 | 2.464 | Kriek et al. (2015) | 5.05 ± 1.54 | 453 ± 138 | 1.77 | 455 ± 138 | 192^{+42}_{-30} | $11.50^{+0.06}_{-0.05}$ | $2.51^{+0.24}_{-0.16}$ | J |
| 019 | 2.68 | J | 4.97 ± 0.30 | 446 ± 27 | 0.12 | 446 ± 27 | 140^{+32}_{-21} | $11.33^{+0.06}_{-0.06}$ | $3.18^{+0.22}_{-0.15}$ | J |
| 020 | 2.86 | J | 4.88 ± 0.39 | 438 ± 35 | 0.17 | 438 ± 35 | 380^{+61}_{-63} | $10.88^{+0.09}_{-0.08}$ | $3.79^{+0.09}_{-0.10}$ | J |
| 021 | 0.353 | Khostovan et al. (2025) | 4.79 ± 0.91 | 430 ± 82 | 0.01 | 430 ± 82 | 0^{+0}_{-0} | $11.40^{+0.01}_{-0.01}$ | $0.79^{+0.09}_{-0.10}$ | J |
| 022 | 2.25 | J | 4.40 ± 0.36 | 395 ± 32 | 4.45 | 399 ± 32 | 183^{+97}_{-53} | $11.30^{+0.08}_{-0.08}$ | $1.47^{+0.25}_{-0.19}$ | J |
| 023 | 2.103 | Rizzo et al. (2023) | 4.39 ± 0.37 | 394 ± 33 | 0.50 | 394 ± 33 | 184^{+40}_{-31} | $11.53^{+0.07}_{-0.07}$ | $2.20^{+0.27}_{-0.23}$ | J |
| 024 | 3.83 | U | 4.19 ± 0.77 | 376 ± 69 | 0.04 | 376 ± 69 | 272^{+116}_{-105} | $11.56^{+0.09}_{-0.11}$ | $3.24^{+0.29}_{-0.39}$ | U |
| 025 | 5.85 | Casey et al. (2019) | 4.16 ± 0.12 | 373 ± 11 | 0.06 | 373 ± 11 | 68^{+32}_{-20} | $10.61^{+0.12}_{-0.12}$ | $2.94^{+0.33}_{-0.31}$ | J |
| 026 | 3.47 | J | 4.13 ± 0.25 | 371 ± 22 | 0.33 | 372 ± 22 | 157^{+218}_{-46} | $11.09^{+0.10}_{-0.25}$ | $2.51^{+0.27}_{-0.27}$ | J |
| 027 | 2.163 | Brammer et al. (2012); Momcheva et al. (2015) | 3.72 ± 0.48 | 334 ± 42 | 0.04 | 334 ± 42 | 90^{+18}_{-26} | $11.34^{+0.06}_{-0.05}$ | $2.64^{+0.20}_{-0.19}$ | J |
| 028 | 2.17 | U | 3.64 ± 0.23 | 327 ± 20 | 0.23 | 327 ± 20 | 52^{+11}_{-8} | $11.00^{+0.06}_{-0.07}$ | $1.95^{+0.20}_{-0.18}$ | U |
| 029 | 2.81 | U | 3.62 ± 0.19 | 325 ± 17 | 0.57 | 325 ± 17 | 66^{+19}_{-12} | $10.97^{+0.05}_{-0.06}$ | $1.21^{+0.19}_{-0.14}$ | U |
| 030 | 3.21 | J | 3.62 ± 0.34 | 325 ± 30 | 0.05 | 325 ± 30 | 59^{+15}_{-14} | $10.93^{+0.08}_{-0.07}$ | $2.77^{+0.33}_{-0.23}$ | J |
| 031 | 4.621 | Mitsubishi et al. (2021) | 3.61 ± 0.43 | 324 ± 38 | 0.21 | 324 ± 38 | 91^{+26}_{-23} | $10.90^{+0.08}_{-0.08}$ | $2.20^{+0.26}_{-0.25}$ | J |
| 032 | 2.012 | Brammer et al. (2012); Momcheva et al. (2015) | 3.45 ± 0.23 | 310 ± 20 | 0.08 | 310 ± 20 | 81^{+16}_{-15} | $11.24^{+0.06}_{-0.06}$ | $2.67^{+0.34}_{-0.29}$ | J |
| 033 | 4.30 | J | 3.27 ± 0.29 | 293 ± 26 | 0.01 | 293 ± 26 | 220^{+71}_{-52} | $11.32^{+0.09}_{-0.08}$ | $3.96^{+0.31}_{-0.30}$ | J |
| 034 | 3.55 | J | 3.25 ± 0.54 | 292 ± 48 | 0.00 | 292 ± 48 | 0^{+339}_{-0} | $11.79^{+0.07}_{-0.11}$ | $2.10^{+0.59}_{-0.37}$ | J |
| 035 | 2.53 | J | 3.20 ± 0.41 | 287 ± 37 | 1.36 | 289 ± 37 | 48^{+3}_{-5} | $10.20^{+0.04}_{-0.02}$ | $0.27^{+0.02}_{-0.04}$ | J |
| 036 | 2.69 | J | 3.11 ± 0.30 | 279 ± 26 | 0.01 | 279 ± 26 | 147^{+59}_{-147} | $11.54^{+0.14}_{-0.07}$ | $3.42^{+0.24}_{-0.64}$ | J |
| 037 | 1.84 | U | 3.07 ± 0.52 | 275 ± 46 | 0.45 | 276 ± 46 | 152^{+62}_{-52} | $11.14^{+0.10}_{-0.05}$ | $1.58^{+0.22}_{-0.26}$ | U |
| 038 | 2.60 | J | 3.07 ± 0.60 | 276 ± 53 | 0.08 | 276 ± 53 | 97^{+25}_{-17} | $11.20^{+0.07}_{-0.05}$ | $2.64^{+0.34}_{-0.20}$ | J |
| 039 | 2.536 | Khostovan et al. (2025) | 3.04 ± 0.66 | 273 ± 59 | 127.55 | 400 ± 64 | 8386^{+304}_{-337} | $11.02^{+0.03}_{-0.02}$ | $0.61^{+0.02}_{-0.01}$ | U |
| 040 | 1.780 | Brammer et al. (2012); Momcheva et al. (2015) | 2.94 ± 0.28 | 263 ± 24 | 0.89 | 264 ± 24 | 490^{+43}_{-71} | $10.87^{+0.05}_{-0.06}$ | $3.12^{+0.07}_{-0.08}$ | J |
| 041 | 1.463 | Silverman et al. (2015) | 2.83 ± 0.23 | 254 ± 20 | 2.06 | 256 ± 20 | 637^{+92}_{-92} | $10.86^{+0.07}_{-0.06}$ | $1.24^{+0.06}_{-0.07}$ | U |
| 042 | 3.46 | J | 2.38 ± 0.43 | 214 ± 38 | 0.51 | 214 ± 38 | 73^{+15}_{-14} | $10.97^{+0.05}_{-0.04}$ | $1.89^{+0.18}_{-0.17}$ | J |

Table A2 – continued

| ID | z | Ref. | $f_{870\mu\text{m}}$ (mJy) | SFR _{FIR} ($M_{\odot}\text{yr}^{-1}$) | SFR _{UV} ($M_{\odot}\text{yr}^{-1}$) | SFR _{raw} ($M_{\odot}\text{yr}^{-1}$) | SFR _{corr} ($M_{\odot}\text{yr}^{-1}$) | M_{*} ($\log M_{\odot}$) | A_V | Flag |
|-----|-------|---|-------------------------------|---|--|---|--|---------------------------------|------------------------|------|
| 043 | 1.324 | Kriek et al. (2015) | 2.83 ± 0.58 | 254 ± 52 | 0.46 | 254 ± 52 | 244^{+78}_{-57} | $10.94^{+0.06}_{-0.06}$ | $1.57^{+0.18}_{-0.18}$ | U |
| 044 | 3.53 | J | 2.64 ± 0.44 | 237 ± 39 | 0.20 | 237 ± 39 | 115^{+27}_{-29} | $11.18^{+0.07}_{-0.06}$ | $2.34^{+0.29}_{-0.22}$ | J |
| 045 | 2.89 | U | 2.60 ± 0.22 | 233 ± 20 | 0.33 | 233 ± 20 | 93^{+22}_{-20} | $11.12^{+0.08}_{-0.07}$ | $1.79^{+0.22}_{-0.21}$ | U |
| 046 | 4.200 | J | 2.57 ± 0.29 | 231 ± 25 | 0.14 | 231 ± 25 | 159^{+39}_{-38} | $11.21^{+0.07}_{-0.07}$ | $2.85^{+0.30}_{-0.25}$ | J |
| 047 | 2.62 | J | 2.50 ± 0.43 | 225 ± 38 | 0.35 | 225 ± 38 | 101^{+58}_{-27} | $11.02^{+0.08}_{-0.09}$ | $2.47^{+0.23}_{-0.23}$ | J |
| 048 | 0.748 | van der Wel et al. (2021) | 2.47 ± 0.14 | 222 ± 12 | 0.47 | 222 ± 12 | 38^{+8}_{-5} | $11.16^{+0.04}_{-0.08}$ | $1.37^{+0.13}_{-0.14}$ | U |
| 049 | 1.736 | Brammer et al. (2012); Momcheva et al. (2015) | 2.37 ± 0.45 | 213 ± 40 | 0.02 | 213 ± 40 | 43^{+14}_{-25} | $11.14^{+0.12}_{-0.07}$ | $3.47^{+0.20}_{-0.32}$ | J |
| 050 | 2.59 | J | 2.35 ± 0.13 | 211 ± 11 | 0.03 | 211 ± 11 | 89^{+24}_{-16} | $11.19^{+0.07}_{-0.07}$ | $3.41^{+0.36}_{-0.24}$ | J |
| 051 | 2.73 | J | 2.31 ± 0.13 | 207 ± 12 | 0.06 | 207 ± 12 | 101^{+22}_{-31} | $11.28^{+0.05}_{-0.05}$ | $2.58^{+0.25}_{-0.36}$ | J |
| 052 | 0.929 | Bourne et al. (2019) | 2.29 ± 0.22 | 206 ± 19 | 0.25 | 206 ± 19 | 37^{+5}_{-5} | $11.16^{+0.05}_{-0.05}$ | $1.75^{+0.26}_{-0.18}$ | J |
| 053 | 1.522 | Brammer et al. (2012); Momcheva et al. (2015) | 2.23 ± 0.26 | 200 ± 22 | 0.33 | 200 ± 22 | 107^{+16}_{-14} | $11.45^{+0.05}_{-0.05}$ | $1.72^{+0.21}_{-0.16}$ | J |
| 054 | 1.831 | Brammer et al. (2012); Momcheva et al. (2015) | 2.17 ± 0.62 | 195 ± 55 | 0.00 | 195 ± 55 | 0^{+3}_{-0} | $11.53^{+0.05}_{-0.10}$ | $3.20^{+0.20}_{-0.34}$ | J |
| 055 | 1.030 | Bourne et al. (2019) | 2.10 ± 0.17 | 188 ± 14 | 0.64 | 189 ± 14 | 42^{+7}_{-5} | $11.15^{+0.04}_{-0.06}$ | $1.65^{+0.25}_{-0.19}$ | J |
| 056 | 2.94 | J | 2.10 ± 0.35 | 189 ± 31 | 0.13 | 189 ± 31 | 91^{+67}_{-19} | $11.00^{+0.09}_{-0.10}$ | $2.92^{+0.25}_{-0.22}$ | J |
| 057 | 5.36 | U | 2.01 ± 0.24 | 181 ± 21 | 0.04 | 181 ± 21 | 0^{+327}_{-0} | $11.74^{+0.20}_{-0.20}$ | $1.30^{+0.69}_{-0.65}$ | U |
| 058 | 2.380 | Brammer et al. (2012); Momcheva et al. (2015) | 1.97 ± 0.37 | 177 ± 33 | 0.77 | 177 ± 33 | 104^{+41}_{-37} | $11.17^{+0.07}_{-0.06}$ | $1.56^{+0.20}_{-0.21}$ | J |
| 059 | 3.50 | J | 1.94 ± 0.24 | 174 ± 21 | 0.04 | 174 ± 21 | 33^{+11}_{-18} | $10.66^{+0.08}_{-0.08}$ | $2.33^{+0.32}_{-0.32}$ | J |
| 060 | 2.55 | U | 1.94 ± 0.43 | 174 ± 38 | 2.06 | 176 ± 38 | 260^{+59}_{-58} | $10.75^{+0.06}_{-0.05}$ | $1.30^{+0.14}_{-0.16}$ | U |
| 061 | 2.33 | J | 1.94 ± 0.43 | 174 ± 38 | 0.19 | 174 ± 38 | 68^{+11}_{-10} | $11.10^{+0.05}_{-0.05}$ | $2.69^{+0.19}_{-0.16}$ | J |
| 062 | 3.422 | Coulter et al. (2024) | 1.91 ± 0.26 | 171 ± 23 | 0.07 | 171 ± 23 | 52^{+15}_{-11} | $10.83^{+0.07}_{-0.08}$ | $2.40^{+0.21}_{-0.20}$ | J |
| 063 | 4.19 | J | 1.90 ± 0.28 | 170 ± 25 | 0.20 | 170 ± 25 | 110^{+24}_{-25} | $11.03^{+0.08}_{-0.07}$ | $2.70^{+0.26}_{-0.21}$ | J |
| 064 | 3.709 | Schreiber et al. (2018b) | 1.89 ± 0.04 | 170 ± 3 | 0.22 | 170 ± 3 | 0^{+0}_{-0} | $10.92^{+0.03}_{-0.03}$ | $0.60^{+0.10}_{-0.11}$ | J |
| 065 | 2.60 | J | 1.87 ± 0.30 | 168 ± 27 | 0.34 | 168 ± 27 | 60^{+33}_{-9} | $10.92^{+0.05}_{-0.11}$ | $2.25^{+0.22}_{-0.15}$ | J |
| 066 | 4.14 | J | 1.79 ± 0.39 | 160 ± 35 | 0.59 | 161 ± 35 | 173^{+109}_{-107} | $10.66^{+0.12}_{-0.11}$ | $2.70^{+0.22}_{-0.39}$ | J |
| 067 | 1.63 | U | 1.62 ± 0.32 | 145 ± 29 | 0.02 | 145 ± 29 | 21^{+5}_{-3} | $10.71^{+0.06}_{-0.05}$ | $1.94^{+0.27}_{-0.21}$ | U |
| 068 | 1.11 | U | 1.54 ± 0.29 | 138 ± 25 | 0.02 | 138 ± 25 | 61^{+13}_{-8} | $11.26^{+0.05}_{-0.08}$ | $2.48^{+0.16}_{-0.17}$ | U |
| 069 | 3.07 | J | 1.53 ± 0.23 | 137 ± 21 | 0.02 | 138 ± 21 | 30^{+9}_{-11} | $10.67^{+0.09}_{-0.09}$ | $3.28^{+0.29}_{-0.34}$ | J |
| 070 | 2.450 | Circosta et al. (2021) | 1.53 ± 0.24 | 137 ± 21 | 0.85 | 138 ± 21 | 202^{+23}_{-34} | $10.64^{+0.10}_{-0.05}$ | $1.80^{+0.09}_{-0.09}$ | J |
| 071 | 1.793 | Champagne et al. (2021) | 1.52 ± 0.28 | 136 ± 25 | 0.18 | 137 ± 25 | 96^{+35}_{-32} | $10.99^{+0.08}_{-0.07}$ | $3.17^{+0.25}_{-0.25}$ | J |
| 072 | 2.70 | J | 1.49 ± 0.36 | 134 ± 32 | 0.37 | 134 ± 32 | 61^{+13}_{-19} | $11.06^{+0.05}_{-0.06}$ | $1.78^{+0.26}_{-0.21}$ | J |
| 073 | 0.919 | Hasinger et al. (2018) | 1.48 ± 0.12 | 133 ± 10 | 0.13 | 133 ± 10 | 43^{+7}_{-6} | $11.20^{+0.05}_{-0.04}$ | $1.80^{+0.24}_{-0.18}$ | U |
| 074 | 1.12 | U | 1.46 ± 0.30 | 131 ± 26 | 0.03 | 131 ± 26 | 39^{+18}_{-8} | $10.96^{+0.06}_{-0.10}$ | $1.96^{+0.25}_{-0.19}$ | U |
| 075 | 2.989 | Coulter et al. (2024) | 1.46 ± 0.39 | 131 ± 34 | 0.94 | 131 ± 34 | 190^{+17}_{-20} | $10.39^{+0.06}_{-0.05}$ | $1.73^{+0.08}_{-0.07}$ | J |
| 076 | 2.474 | Schreiber et al. (2018b) | 1.45 ± 0.34 | 130 ± 30 | 0.01 | 130 ± 30 | 88^{+23}_{-25} | $11.22^{+0.09}_{-0.07}$ | $3.51^{+0.33}_{-0.31}$ | J |
| 077 | 2.98 | J | 1.42 ± 0.32 | 127 ± 28 | 0.03 | 127 ± 28 | 99^{+23}_{-28} | $11.19^{+0.07}_{-0.06}$ | $2.96^{+0.32}_{-0.31}$ | J |
| 078 | 2.467 | Khostovan et al. (2025) | 1.41 ± 0.11 | 126 ± 9 | 0.79 | 127 ± 9 | 65^{+57}_{-17} | $10.90^{+0.07}_{-0.15}$ | $1.86^{+0.28}_{-0.22}$ | J |
| 079 | 1.11 | U | 1.41 ± 0.27 | 126 ± 24 | 0.02 | 126 ± 24 | 20^{+7}_{-3} | $10.73^{+0.06}_{-0.08}$ | $2.11^{+0.28}_{-0.21}$ | U |
| 080 | 5.852 | Casey et al. (2019) | 1.40 ± 0.09 | 125 ± 8 | 0.02 | 125 ± 8 | 27^{+12}_{-27} | $10.36^{+0.13}_{-0.12}$ | $2.41^{+0.30}_{-0.32}$ | J |
| 081 | 3.69 | J | 1.40 ± 0.23 | 125 ± 20 | 0.01 | 125 ± 20 | 0^{+0}_{-0} | $10.40^{+0.02}_{-0.02}$ | $0.50^{+0.05}_{-0.05}$ | J |
| 082 | 1.610 | Brammer et al. (2012); Momcheva et al. (2015) | 1.31 ± 0.28 | 117 ± 24 | 0.05 | 117 ± 24 | 60^{+11}_{-13} | $11.21^{+0.06}_{-0.07}$ | $2.81^{+0.31}_{-0.27}$ | J |
| 083 | 1.68 | J | 1.31 ± 0.31 | 118 ± 28 | 0.82 | 118 ± 28 | 43^{+5}_{-4} | $10.01^{+0.03}_{-0.04}$ | $1.65^{+0.04}_{-0.05}$ | J |
| 084 | 1.139 | Valentino et al. (2018) | 1.29 ± 0.31 | 115 ± 27 | 0.16 | 115 ± 27 | 42^{+5}_{-6} | $11.16^{+0.05}_{-0.05}$ | $2.30^{+0.15}_{-0.17}$ | J |
| 085 | 1.746 | Brammer et al. (2012); Momcheva et al. (2015) | 1.29 ± 0.38 | 115 ± 34 | 1.94 | 117 ± 34 | 57^{+4}_{-3} | $10.58^{+0.01}_{-0.02}$ | $1.45^{+0.05}_{-0.04}$ | J |
| 086 | 3.256 | Kriek et al. (2015) | 1.28 ± 0.31 | 114 ± 27 | 1.44 | 116 ± 27 | 183^{+34}_{-37} | $10.05^{+0.11}_{-0.10}$ | $1.15^{+0.06}_{-0.05}$ | J |

Table A2 – continued

| ID | z | Ref. | $f_{870\mu\text{m}}$ (mJy) | SFR _{FIR} ($M_{\odot}\text{yr}^{-1}$) | SFR _{UV} ($M_{\odot}\text{yr}^{-1}$) | SFR _{raw} ($M_{\odot}\text{yr}^{-1}$) | SFR _{corr} ($M_{\odot}\text{yr}^{-1}$) | M_{*} ($\log M_{\odot}$) | A_V | Flag |
|-----|-------|---|-------------------------------|---|--|---|--|---------------------------------|------------------------|------|
| 087 | 1.214 | Bourne et al. (2019) | 1.27 ± 0.10 | 113 ± 8 | 0.00 | 113 ± 8 | 0^{+0}_{-0} | $11.63^{+0.03}_{-0.04}$ | $2.16^{+0.23}_{-0.29}$ | J |
| 088 | 5.17 | J | 1.26 ± 0.24 | 113 ± 21 | 0.59 | 113 ± 21 | 793^{+461}_{-321} | $11.01^{+0.15}_{-0.15}$ | $2.61^{+0.38}_{-0.31}$ | J |
| 089 | 3.291 | Belli et al. (2021) | 1.25 ± 0.15 | 112 ± 13 | 2.04 | 114 ± 13 | 55^{+16}_{-7} | $10.81^{+0.04}_{-0.05}$ | $0.94^{+0.15}_{-0.10}$ | J |
| 090 | 2.71 | J | 1.23 ± 0.21 | 110 ± 19 | 0.02 | 110 ± 19 | 27^{+6}_{-6} | $10.65^{+0.07}_{-0.05}$ | $2.41^{+0.42}_{-0.19}$ | J |
| 091 | 2.488 | Coulter et al. (2024) | 1.22 ± 0.29 | 109 ± 26 | 0.01 | 109 ± 26 | 52^{+13}_{-14} | $10.98^{+0.08}_{-0.07}$ | $3.23^{+0.31}_{-0.37}$ | J |
| 092 | 0.688 | van der Wel et al. (2021) | 1.20 ± 0.26 | 107 ± 23 | 0.15 | 108 ± 23 | 283^{+32}_{-27} | $11.13^{+0.04}_{-0.03}$ | $3.96^{+0.06}_{-0.06}$ | J |
| 093 | 1.27 | Valentino et al. (2018, 2020) | 1.18 ± 0.10 | 106 ± 8 | 0.41 | 106 ± 8 | 40^{+11}_{-6} | $10.97^{+0.06}_{-0.10}$ | $1.50^{+0.15}_{-0.14}$ | J |
| 094 | 1.746 | Brammer et al. (2012); Momcheva et al. (2015) | 1.18 ± 0.16 | 105 ± 14 | 0.03 | 105 ± 14 | 33^{+5}_{-5} | $10.91^{+0.05}_{-0.07}$ | $3.25^{+0.24}_{-0.25}$ | J |
| 095 | 0.726 | van der Wel et al. (2021) | 1.18 ± 0.33 | 106 ± 29 | 1.90 | 108 ± 29 | 29^{+3}_{-4} | $11.12^{+0.04}_{-0.03}$ | $0.85^{+0.13}_{-0.11}$ | J |
| 096 | 2.75 | J | 1.14 ± 0.33 | 102 ± 29 | 0.06 | 102 ± 29 | 49^{+15}_{-9} | $10.84^{+0.08}_{-0.07}$ | $2.84^{+0.27}_{-0.19}$ | J |
| 097 | 1.62 | U | 1.11 ± 0.24 | 99 ± 21 | 0.88 | 100 ± 21 | 116^{+29}_{-27} | $10.69^{+0.05}_{-0.05}$ | $1.28^{+0.14}_{-0.17}$ | U |
| 098 | 1.82 | J | 1.10 ± 0.34 | 99 ± 30 | 0.15 | 99 ± 30 | 55^{+8}_{-8} | $11.11^{+0.05}_{-0.04}$ | $2.03^{+0.22}_{-0.15}$ | J |
| 099 | 1.51 | U | 1.09 ± 0.23 | 97 ± 20 | 0.04 | 97 ± 20 | 27^{+3}_{-4} | $10.87^{+0.03}_{-0.04}$ | $1.68^{+0.14}_{-0.14}$ | U |
| 100 | 2.676 | Khostovan et al. (2025) | 1.06 ± 0.29 | 95 ± 26 | 9.29 | 104 ± 26 | 209^{+22}_{-23} | $10.27^{+0.05}_{-0.05}$ | $0.60^{+0.02}_{-0.02}$ | J |
| 101 | 4.41 | J | 1.05 ± 0.29 | 94 ± 26 | 8.12 | 102 ± 26 | 158^{+34}_{-31} | $10.22^{+0.07}_{-0.06}$ | $0.64^{+0.07}_{-0.06}$ | J |
| 102 | 2.204 | Brammer et al. (2012); Momcheva et al. (2015) | 1.00 ± 0.28 | 89 ± 25 | 0.19 | 89 ± 25 | 90^{+27}_{-23} | $10.71^{+0.08}_{-0.08}$ | $2.53^{+0.12}_{-0.16}$ | J |
| 103 | 3.20 | J | 0.98 ± 0.16 | 88 ± 13 | 0.58 | 88 ± 13 | 22^{+4}_{-3} | $10.48^{+0.04}_{-0.05}$ | $1.16^{+0.15}_{-0.12}$ | J |
| 104 | 2.642 | Brammer et al. (2012); Momcheva et al. (2015) | 0.94 ± 0.17 | 84 ± 15 | 0.59 | 85 ± 15 | 51^{+20}_{-9} | $10.85^{+0.06}_{-0.06}$ | $1.40^{+0.26}_{-0.22}$ | J |
| 105 | 1.54 | J | 0.90 ± 0.17 | 80 ± 15 | 0.09 | 80 ± 15 | 8^{+1}_{-1} | $10.33^{+0.03}_{-0.03}$ | $1.58^{+0.09}_{-0.09}$ | J |
| 106 | 2.19 | J | 0.90 ± 0.24 | 81 ± 21 | 0.07 | 81 ± 21 | 16^{+5}_{-3} | $10.46^{+0.06}_{-0.06}$ | $1.91^{+0.20}_{-0.17}$ | J |
| 107 | 2.21 | U | 0.88 ± 0.09 | 79 ± 7 | 0.16 | 79 ± 7 | 13^{+3}_{-3} | $10.41^{+0.06}_{-0.06}$ | $1.44^{+0.22}_{-0.20}$ | U |
| 108 | 1.968 | Brammer et al. (2012); Momcheva et al. (2015) | 0.85 ± 0.27 | 76 ± 23 | 0.12 | 76 ± 23 | 47^{+8}_{-7} | $10.99^{+0.05}_{-0.06}$ | $2.91^{+0.26}_{-0.25}$ | J |
| 109 | 2.98 | J | 0.84 ± 0.19 | 75 ± 17 | 3.56 | 79 ± 17 | 136^{+16}_{-26} | $10.32^{+0.08}_{-0.04}$ | $1.10^{+0.05}_{-0.07}$ | J |
| 110 | 3.46 | J | 0.80 ± 0.20 | 71 ± 17 | 0.23 | 71 ± 17 | 36^{+13}_{-6} | $10.60^{+0.06}_{-0.06}$ | $1.98^{+0.21}_{-0.18}$ | J |
| 111 | 3.529 | Kriek et al. (2015) | 0.70 ± 0.21 | 63 ± 19 | 2.67 | 66 ± 19 | 59^{+21}_{-10} | $10.75^{+0.05}_{-0.07}$ | $0.86^{+0.15}_{-0.11}$ | J |
| 112 | 2.195 | Brammer et al. (2012); Momcheva et al. (2015) | 0.69 ± 0.11 | 62 ± 10 | 3.31 | 65 ± 10 | 120^{+23}_{-28} | $10.64^{+0.07}_{-0.06}$ | $0.99^{+0.08}_{-0.13}$ | J |
| 113 | 2.193 | Brammer et al. (2012); Momcheva et al. (2015) | 0.69 ± 0.15 | 61 ± 13 | 0.38 | 62 ± 13 | 85^{+40}_{-24} | $11.01^{+0.06}_{-0.08}$ | $2.56^{+0.17}_{-0.23}$ | J |
| 114 | 1.88 | U | 0.67 ± 0.13 | 60 ± 11 | 0.18 | 60 ± 11 | 15^{+2}_{-2} | $10.49^{+0.05}_{-0.05}$ | $1.38^{+0.17}_{-0.14}$ | U |
| 115 | 2.514 | Glazebrook et al. (2021) | 0.63 ± 0.13 | 56 ± 11 | 0.06 | 56 ± 11 | 45^{+15}_{-9} | $10.86^{+0.07}_{-0.07}$ | $2.17^{+0.34}_{-0.26}$ | J |
| 116 | 2.469 | Sanders et al. (2023) | 0.59 ± 0.12 | 53 ± 10 | 0.87 | 53 ± 10 | 136^{+25}_{-44} | $10.60^{+0.10}_{-0.08}$ | $1.81^{+0.08}_{-0.17}$ | J |
| 117 | 1.599 | Brammer et al. (2012); Momcheva et al. (2015) | 0.58 ± 0.14 | 51 ± 12 | 0.01 | 51 ± 12 | 27^{+11}_{-27} | $11.08^{+0.26}_{-0.10}$ | $3.19^{+0.16}_{-0.21}$ | J |
| 118 | 5.536 | Fujimoto et al. (2020) | 0.56 ± 0.11 | 50 ± 10 | 4.97 | 55 ± 10 | 46^{+12}_{-9} | $10.50^{+0.07}_{-0.08}$ | $0.29^{+0.11}_{-0.09}$ | U |
| 119 | 2.216 | Brammer et al. (2012); Momcheva et al. (2015) | 0.54 ± 0.17 | 48 ± 14 | 0.48 | 48 ± 14 | 91^{+36}_{-32} | $10.88^{+0.12}_{-0.09}$ | $1.82^{+0.23}_{-0.22}$ | J |
| 120 | 3.82 | U | 0.52 ± 0.13 | 46 ± 11 | 0.32 | 46 ± 11 | 20^{+6}_{-5} | $10.35^{+0.07}_{-0.07}$ | $1.05^{+0.22}_{-0.20}$ | U |
| 121 | 2.90 | J | 0.46 ± 0.07 | 41 ± 6 | 0.23 | 41 ± 6 | 17^{+4}_{-3} | $10.36^{+0.04}_{-0.05}$ | $1.66^{+0.18}_{-0.14}$ | J |
| 122 | 1.646 | Brammer et al. (2012); Momcheva et al. (2015) | 0.45 ± 0.08 | 40 ± 6 | 1.07 | 41 ± 6 | 27^{+4}_{-4} | $10.14^{+0.04}_{-0.04}$ | $1.28^{+0.08}_{-0.10}$ | J |
| 123 | 2.58 | J | 0.44 ± 0.13 | 39 ± 11 | 0.33 | 40 ± 11 | 33^{+7}_{-5} | $10.72^{+0.05}_{-0.05}$ | $1.64^{+0.21}_{-0.16}$ | J |
| 124 | 4.447 | Le Fèvre et al. (2020) | 0.31 ± 0.08 | 27 ± 6 | 11.67 | 39 ± 7 | 29^{+4}_{-3} | $9.76^{+0.05}_{-0.04}$ | $0.19^{+0.04}_{-0.03}$ | J |
| 125 | 4.578 | Fujimoto et al. (2020) | 0.30 ± 0.06 | 26 ± 5 | 3.39 | 30 ± 5 | 13^{+3}_{-2} | $9.41^{+0.08}_{-0.06}$ | $0.34^{+0.06}_{-0.06}$ | J |
| 126 | 6.854 | Smit et al. (2018) | 0.27 ± 0.04 | 24 ± 3 | 14.61 | 38 ± 4 | 28^{+4}_{-4} | $10.19^{+0.05}_{-0.05}$ | $0.16^{+0.05}_{-0.05}$ | J |
| 127 | 0.945 | Brammer et al. (2012); Momcheva et al. (2015) | 0.18 ± 0.03 | 16 ± 3 | 0.02 | 16 ± 3 | 9^{+1}_{-2} | $10.48^{+0.05}_{-0.08}$ | $2.67^{+0.15}_{-0.43}$ | J |
| 128 | 2.33 | U | 0.16 ± 0.03 | 14 ± 2 | 0.48 | 15 ± 2 | 18^{+13}_{-7} | $11.04^{+0.04}_{-0.04}$ | $1.02^{+0.30}_{-0.29}$ | U |

APPENDIX B: COLOUR (RGB) POSTAGE-STAMP IMAGES OF THE NEAR-MID INFRARED ALMA-DETECTED GALAXIES

In this Appendix we provide three-colour (RGB) postage-stamp images of all the near-mid infrared galaxy counterparts of the 128 ALMA sources in our final PRIMER COSMOS sample. Where NIRC*am* imaging was available these were created using the F444W (red), F277W (green) and F115W (blue) images, after convolving the imaging in the latter two filters to the same resolution as the F444W imaging. Where NIRC*am* imaging was not available (i.e., in the regions with only *JWST* MIRI coverage) we used the MIRI 18 μm (red) and 7.7 μm (yellow) imaging to produce the pseudo-colour images (albeit these inevitably have poorer resolution than the NIRC*am* examples).

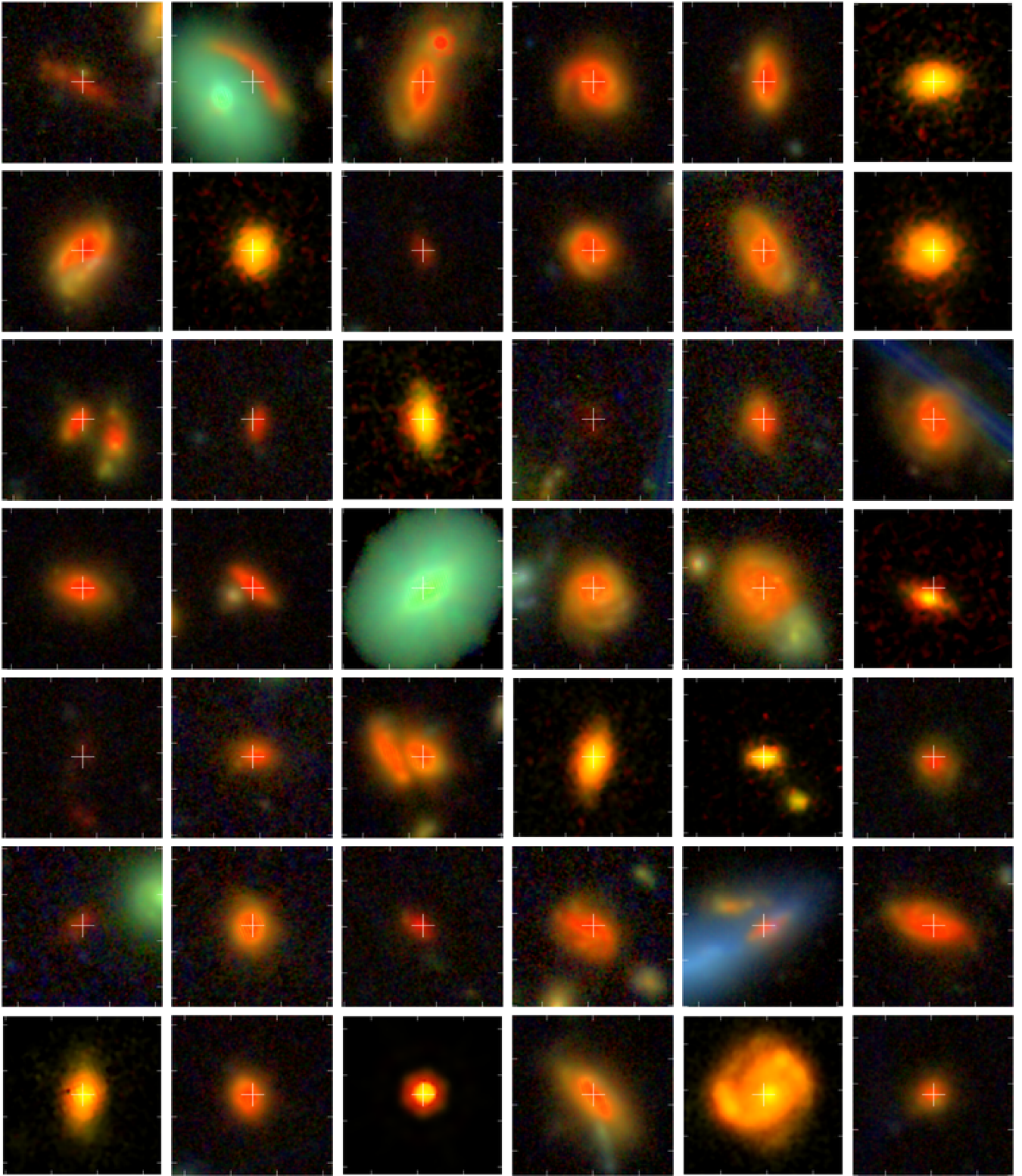


Figure B1. RGB postage-stamp images of the near-mid infrared galaxy counterparts of all 128 ALMA sources in our final PRIMER COSMOS sample. For sources covered by NIRCcam, the images are produced using F444W (red), F277W (green), and F115W (blue) after convolving the shorter wavelength images to the same resolution as the F444W imaging. Where NIRCcam imaging was not available (i.e., in the regions with only *JWST* MIRI coverage) we used the MIRI 18 μm (red) and 7.7 μm (yellow) imaging to produce the pseudo-colour images (albeit these inevitably have poorer resolution than the NIRCcam examples). The ALMA coordinates from the highest-S/N detection (see Table A1) are marked as white crosses. The size of each image is $3.5'' \times 3.5''$, with an axis tick every arcsec.

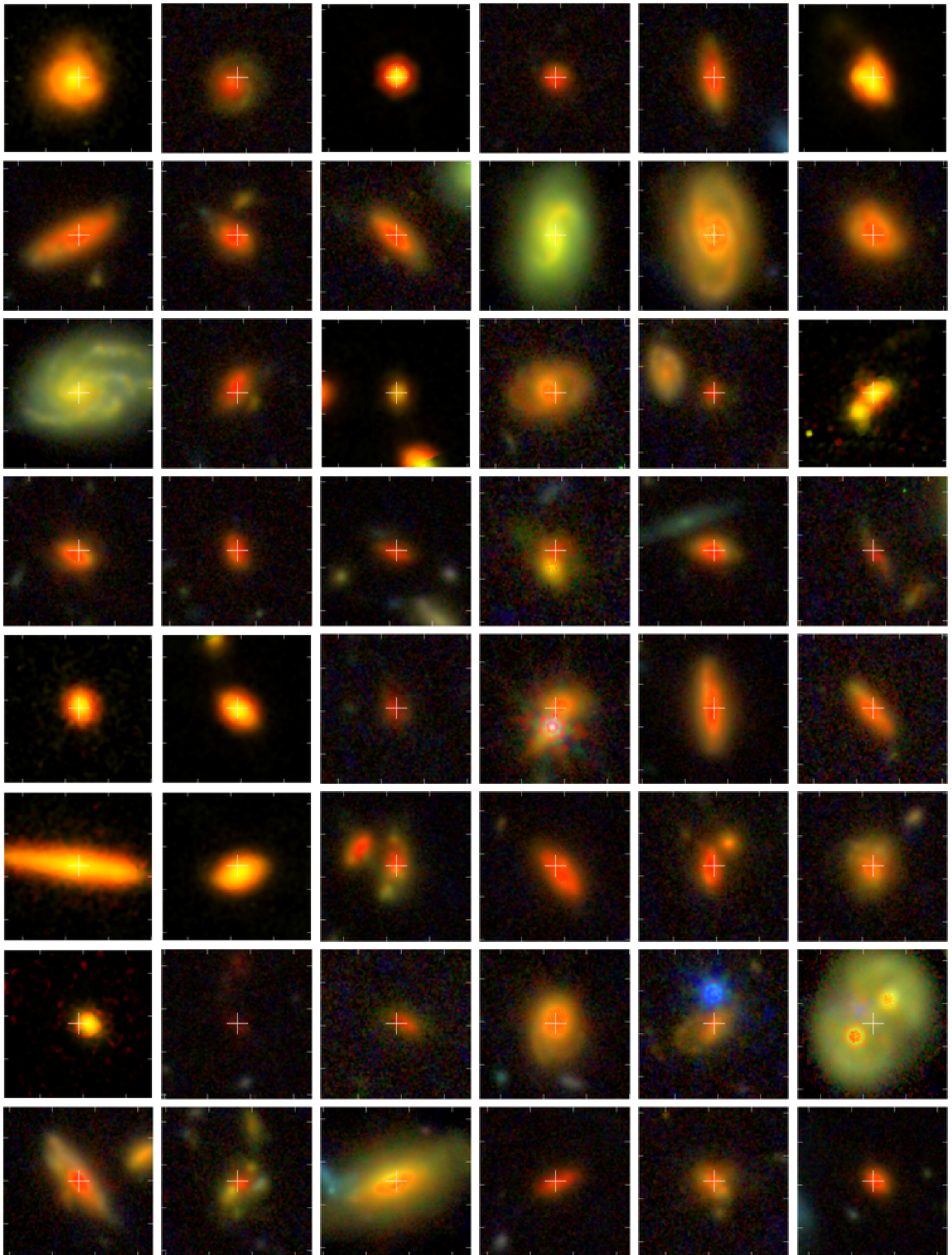


Figure B1 – *continued*

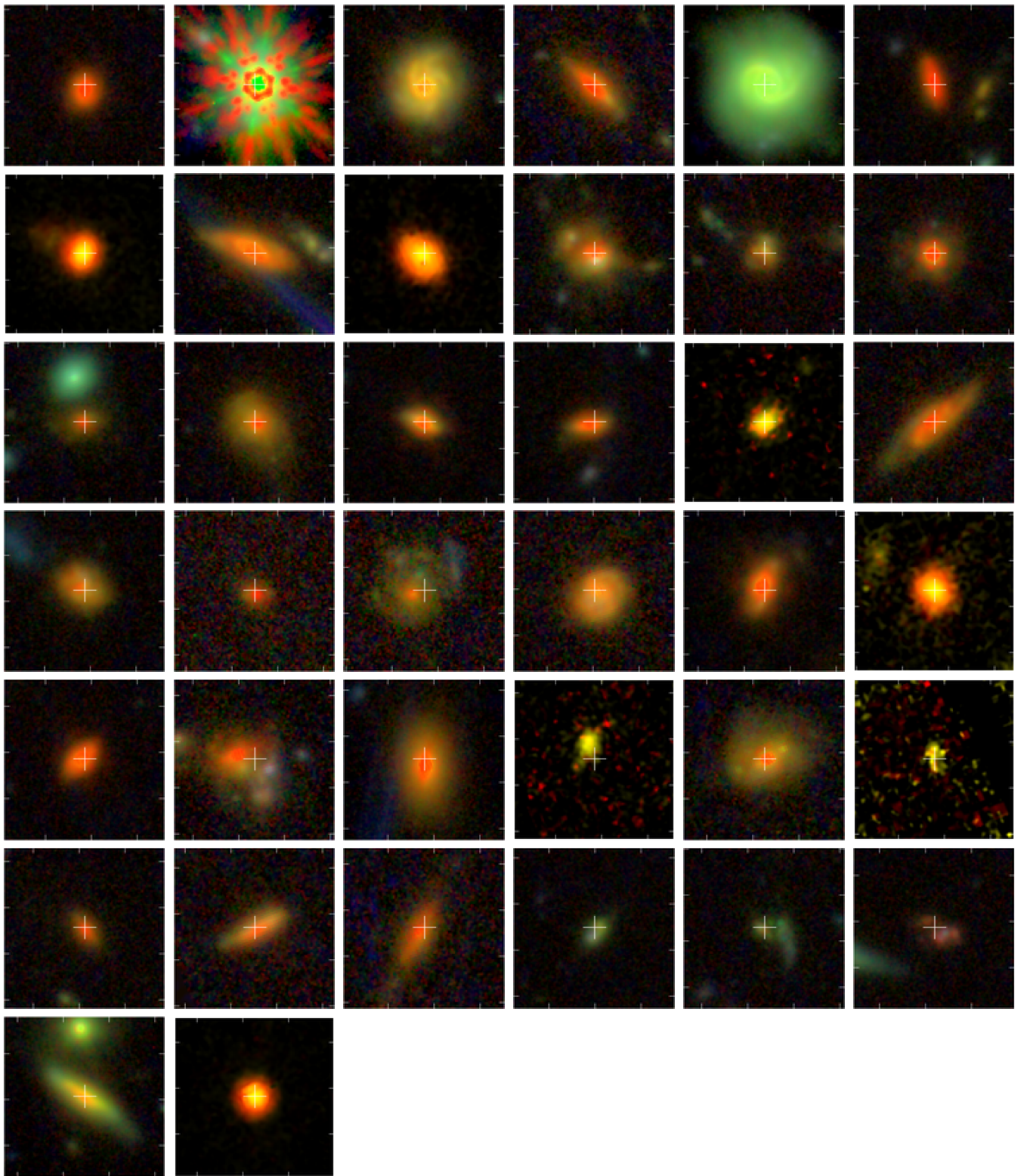


Figure B1 – *continued*

This paper has been typeset from a $\text{\TeX}/\text{\LaTeX}$ file prepared by the author.